Photoacoustic effect and sonoluminescence generated by laser initiated exothermic chemical reactions

by

Han Jung Park

M.Sc., Physical chemistry, Seoul National University, 2005

B. S., Chemistry, Korea University, 2003

Thesis

Submitted in partial fulfillment of the requirements for

the degree of Doctor of Philosophy

in the Department of Chemistry at Brown University

May 2011

This dissertation by Han Jung Park is accepted in its present form

by the Department of Chemistry as satisfying the dissertation requirement

for the degree of Doctor of Philosophy

Date…… ……..

Gerald J. Diebold, Director

Recommended to the Graduate Council

Date…… ……..

Jimmie D. Doll, Reader

Date…… ……..

Christoph Rose-Petruck, Reader

Approved by the Graduate Council

Date…… ……..

Peter M. Weber

Dean of Graduate School and Research

Vita

Han Jung Park was born in Seoul, South Korea on April 24th, 1977. He completed his secondary education from Kyunggi High School in Seoul, South Korea in February of 1996. He then attended Korea University in Seoul. He served the mandatory military service at Seoul Air Base from 1998 to 2001. He obtained a Bachelor of Science degree in Chemistry in February of 2003. He later attended Seoul National University in March of 2003. He received a Master of Science degree in Physical Chemistry in February of 2005. In September of 2006, he began his graduate studies in the Department of Chemistry at Brown University. He carried out his doctoral research under the supervision of Professor Gerald J. Diebold.

Abstract of "photoacoustic effect and sonoluminescence generated by laser initiated exothermic chemical reactions", by Han Jung Park, Ph. D., Brown University, May 2011.

This thesis describes an experimental investigation of the photoacoustic effect generated by laser initiated exothermic chemical reactions. Experiments were carried out to determine the influence of the addition of H_2O_2 on the production of the photoacoustic effect in colloidal suspensions of C nanoparticles in H_2O. A Q-switched Nd:YAG laser fundamental at 1064 or its frequency doubled output at 532 nm was used to irradiate the suspensions. A polyvinylidene film transducer was placed in contact with the cuvette at perpendicular incidence to the direction of propagation of the laser beam to record the acoustic wave. The inclusion of H_2O_2 in an aqueous C suspension changes the normally endothermic reaction of C with H_2O into the highly exothermic reaction of C with H_2O_2 leading to both an enhanced photoacoustic effect and an increase in light emission from the suspension.

Aside from the photoacoutic effect, chemical generation of a sonoluminescing bubble is discussed. The aim of this research is to investigate the possibility of depositing chemical energy into a sonoluminescing bubble, in particular, to determine the influence of the addition of H_2O_2 on the production of the sonoluminescent light in colloidal suspensions of C nanoparticles in H_2O. To generate sonoluminescence, the 1064 nm output of a Q-switched Nd:YAG laser was focused with a lens into a reaction chamber. Light scattering was used to monitor the oscillations in the diameter of the bubble by directing a He-Ne laser beam into the reaction chamber at the point where the Nd:YAG laser beam was focused. Adding hydrogen peroxide to colloidal carbon suspensions increased both the

time of the sonoluminescent flash following the laser pulse and the intensity of sonoluminescence, indicating that large, highly energetic gas bubbles were produced.

In the last chapter, the application of intense ultrasound to a liquid-gas interface is discussed. The composition of the vapor and aerosol above an ultrasonic fountain is determined as a function of irradiation time and compared with the results of sparging for five different solutions. The experiments show that ultrasonic distillation produces separations that are somewhat less complete than what is obtained using sparging.

Acknowledgements

I would especially like to express my appreciation to my graduate adviser, Professor Gerald J. Diebold, for giving me the chance to work in his group and supporting me in every aspect of my research.

During the course of my graduate education, I have benefited from numerous discussions with a number of professors in the Department of Chemistry. I would especially like to thank Professor Christoph Rose-Petruck, Jimmie M. Doll and James Baird for all their suggestions.

I am also indebted to Ken Talbot for his assistance in the construction of the experimental equipment and Alfred Tente for his help with the electronic equipment.

I am thankful to the people who have made working in the laboratory a more enjoyable experience. They include Dr. Cliff Frez, Dr. Cuong Nguyen, Hye Yun Jung, Binbin Wu, and Ziyao Tang. In particular, I would like to express my appreciation to Dr. Jinkee Lee for proof reading this thesis.

Most of all, I wish to thank my parents for their support and love.

This thesis was typeset using *Microsoft Word* 2010

Publications

- **Han Jung Park** and Gerald J. Diebold "Generation of ultrasonic vibration potential through rapid fluid deceleration," Manuscript in preparation
- **Han Jung Park** and Gerald J. Diebold "Generation of sonoluminescence by laser-induced exothermic chemical reaction," Manuscript in preparation
- **Han Jung Park**, Binbin Wu, and Gerald J. Diebold "Effects of exothermic chemical reaction on photoacoustic effect from particulate matter," *J. Chem. Phys*., **2011**, 134, 124513
- Hye Yun Jung, **Han Jung Park**, Joseph M. Calo, and Gerald J. Diebold "Comparison of ultrasonic distillation to sparging of liquid mixtures," *Anal. Chem*., **2010**, 82 (24), 10090--10094

Presentations

- (**Invited**) The 161st Meeting of the Acoustical Society of America, Seattle, WA, May 23-27, **2011**, (lecture session - 1pPA, General Topics in Nonlinear Acoustics), "Enhancement of the photoacoustic effect and sonoluminescence in carbon suspensions through exothermic chemical reaction"
- Spring 2011 Joint Meeting of the New England Sections of the American Physical Society and the American Association of Physics Teachers, University of Massachusetts Lowell, April 8-9, **2011**, C1.08, "Comparison of ultrasonic distillation to sparging of liquid mixtures"
- Joint Fall Meeting of the New England Sections of the American Physical Society and the American Association of Physics Teachers, Brown University, October 29-30, **2010**, B1.00003, "Photoacoustic effect and sonoluminescence generated by laser initiated exothermic chemical reactions in carbon suspensions"
- 240th ACS National Meeting, Boston, MA, August 22-26, **2010**, PHYS-444, "Photoacoustic effect and sonoluminescence generated by laser initiated exothermic chemical reactions in carbon suspensions"
- 48th Course First Mediterranean International Workshop on Photoacoustic & Photothermal Phenomena, Italy, July **2010**, "Photoacoustic effect in phononic structures, and chemically reacting systems" (with Prof. Diebold)
- 236th ACS National Meeting, Philadelphia, PA, August 17-21, **2008**, PHYS-462, "Sonoluminescence initiated by laser irradiation of carbon suspensions: Effects of external pressure on sonoluminescent intensity"

Contents

List of Tables

List of Figures

Chapter 1 Photoacoustics

1. 1 Historical Overview

Photoacoustics (PA) is the generation of acoustic waves by modulated optical radiation. Alexander Graham Bell (1) accidently found the photoacoustic effect in solids in 1880 (2). Subsequently, Bell and his associate Summer Tainter found the effect in liquids and gases. The radiation sources were the sun and a Hg arc. The human ear was used as the signal detector. The established gas kinetic theory explained the photoacoustic generation in gases (3) (4). The explanation of photoacoustic generation from liquids and solids was predicted by Mercadier (1881) (5) and Preece (1881) (6), who claimed that the source of photoacoustic came from periodic heat flow. Photoacoustic studies were thereafter suspended since the scientific community believed that photoacoustics had no great scientific or practical value, as well, there were no detectors to detect and quantify the photoacoustic signal.

Figure 1: Spectrophone, as proposed by A. G. Bell in 1881 from ref. **(2)**.

In 1938, however, photoacoustic studies were reborn by the advent of the microphone (7), but the studies were limited only to gas mixtures. The sensitivity was limited by that of the microphone and the background absorption of the incident radiation by the photoacoustic cell windows and walls. In 1971, a renewed interest in photoacoustics appeared with the advent of lasers which could provide intense coherent radiation. Renewed interest in the photoacoustic effect began with the work of Kruezer (8), who reported that ultra-trace components of gases could be detected by laser-induced photoacoustic generation.

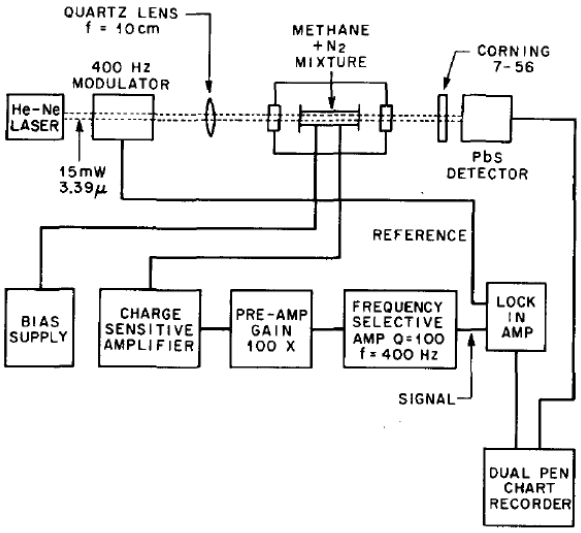

Figure 2: Kruezer's experimental arrangement used to measure the sensitivity for detecting methane mixed with nitrogen from ref. **(8)**.

In 1973, laser-induced photoacoustic studies on solids and liquids reappeared when A. Rosencwaig (9) used a variation of the gas analysis method to study optical absorption at solids surfaces. Subsequently, much experimental and theoretical work has been reported in the literature to demonstrate photoacoustic spectroscopic applications as well as many other photoacoustic applications in various fields of physics, chemistry, biology, engineering, and medicine.

1. 2 Application of Photoacoustics

Photoacoustic Spectroscopy

Photoacoustic spectroscopy records the heat release via pressure changes, following the conversion of absorbed energy into heat. (10) (11) Photoacoustic spectroscopy records information about optical absorption without the effects of scattering. Because photoacoustic spectroscopy does not measure transmitted light intensities, sample opacity and scattering difficulties do not limit this analytical method. Rosencwaig records photoacoustic spectra of blood samples, powder samples, spots on a TLC plate, and leaves from a plant. (10) (12) Gathering spectra of these samples by traditional spectroscopic methods would be highly difficult due to errors from scattering.

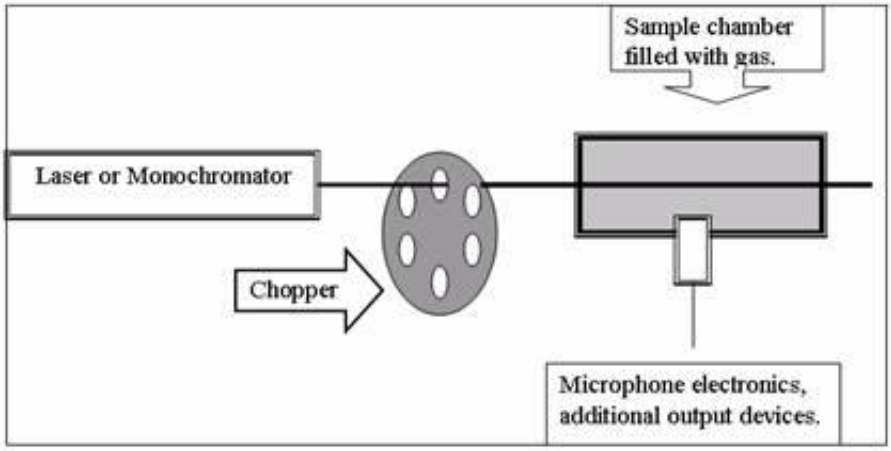

Figure 3: General experimental setup for performing photoacoustic spectroscopy on a gas from ref. **(13)**.

Imaging

Photoacoustic imaging, as a hybrid biomedical imaging modality, is developed based on the photoacoustic effect. It is an analytical method that makes use of amplitude-modulated radiation as a means of probing the absorptive properties of a scanned region. (14) (15) Contrast with this technique relies on physical variations of the irradiated region (such as cracks, defects, or chemical erosion) that have associated variations in their absorption coefficients. (10) These physical variations result in the launching of characteristically different photoacoustic waves. (14) (15) (16) (17) (18) The attraction of this technique in clinical applications is due to its contrast for blood, and that it does not require ionizing radiation.

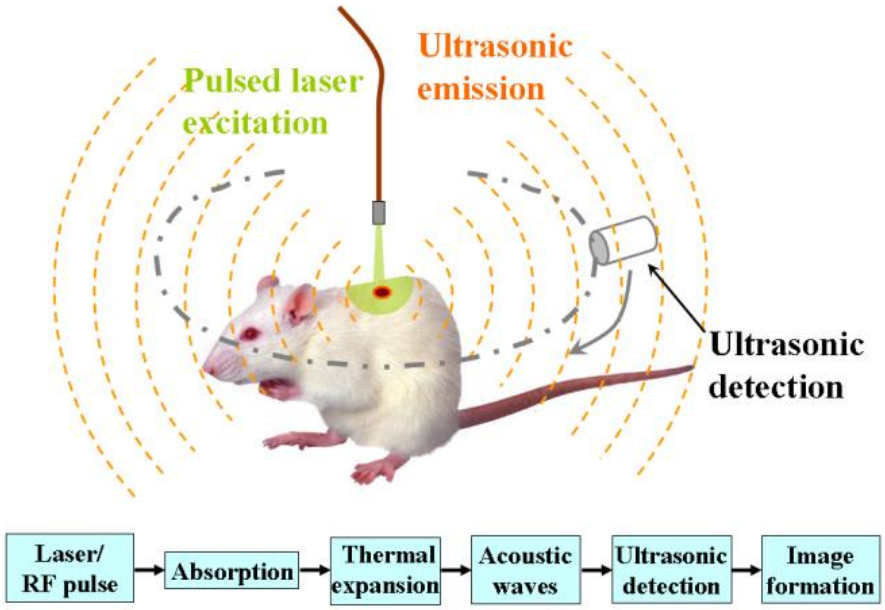

Figure 4: Schematic illustration of photoacoustic imaging.

Chemical Dynamics

Photoacoustics measures heat release following absorption of radiation. If a photochemical reaction generates heat, photoacoustics can be used to obtain kinetic information by means of a refractive index or pressure change. (19) (20) (21) (22) Diebold and coworkers, using the analytical method of photoacoustics, detected and monitored the kinetics of chain reactions. (19) (20)

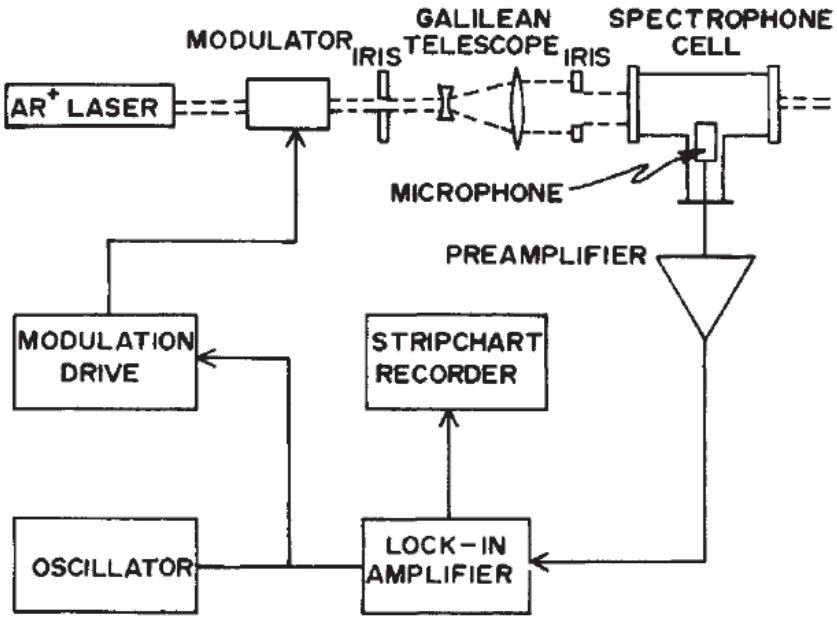

Figure 5: Schematic diagram of the experimental apparatus used to record chemical amplification of optoacoustic signal from ref. **(21)**.

Physical Property Determination

Photoacoustics can be used to determine different thermophysical and acoustic properties of a system, such as density, sound velocity, thermal diffusivity, and viscosity. (16) (17) (18) (23) Diebold and coworkers showed that fluid layers with a specified dimensionless ratio of the product of density and sound velocity of two dissimilar fluids can give unique pressure wave forms dependent on the spatial distribution of absorbed energy. (16) (17) (18) (23) Using a transient grating apparatus and a linear theory of photoacoustics, Diebold and coworkers showed thermal diffusivity, viscosity, and sound speed can be determined by fitting the acoustic and thermal modes of the grating to an analytical equation. (22) (24) (25) (26) (27) (28)

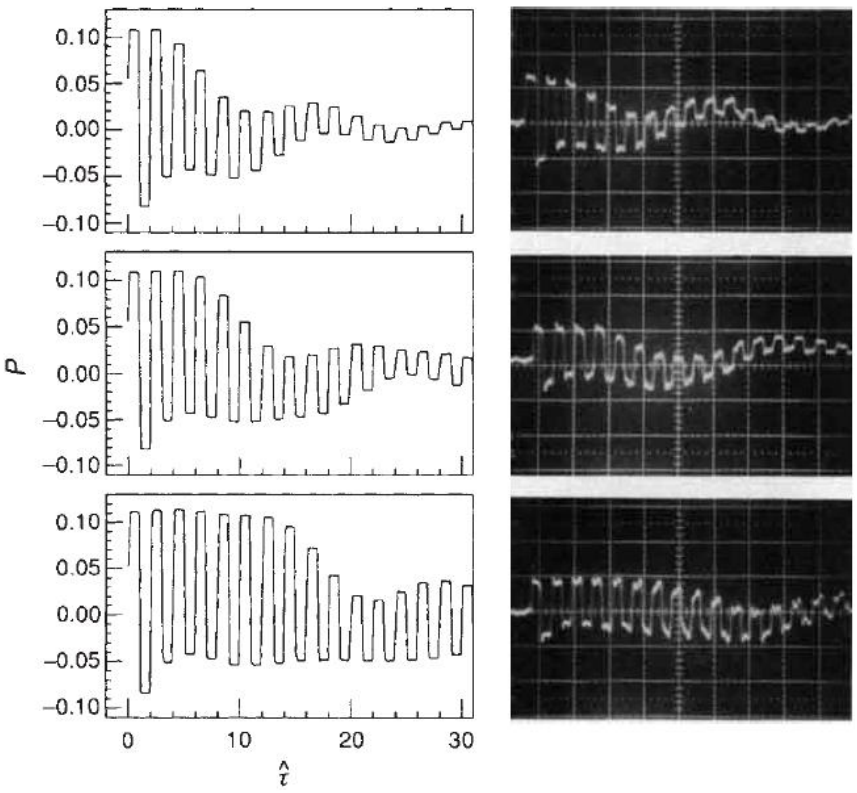

Figure 6: Generation of ultrasonic waves form a layered photoacoustic source from ref. **(23)**.

1. 3 Mechanism of Photoacoustics

Photoacoustic Generation

The generation of acoustic waves follows from the mechanical motion of a volume that results in force acting against its surroundings. The force typically results in a mechanical wave that propagates longitudinally, or parallel to the direction of wave motion. (10) (29) (30) (31) A traveling pressure wave possesses both compressions and rarefactions. (1) (3) (10) (29) (32) (33) In the case of photoacoustics, the generation of sound is initiated by the absorption of modulated light by a volume where the mechanical wave that arises is the response of an irradiated body to minimize the localized stress. Depending on the modulation frequency of the radiation source, the photoaoustic wave can be infrasonic (<1 Hz), audible (16 Hz to 16 kHz), or ultrasonic (>16 kHz). (10) The most common mechanisms by which optical energy are converted into sound are: thermoelastic expansion, volume expansion by a change in phase or by chemical reactions, dielectric breakdown, and electrostriction. (10)

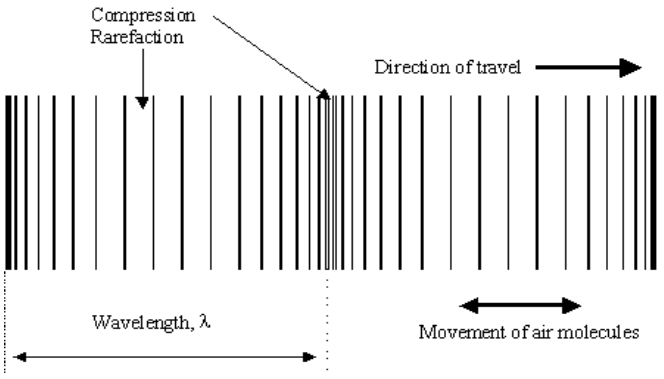

Figure 7: Longitudinal wave.

The general theory of elasticity describes the deformation of a body due to an applied stress (force/unit area) resulting in a strain or unit deformation (a unitless fractional

change in length). (34) (35) Generally, the relationship between stress and strain is linear with the modulus of elasticity used as the proportionality constant. The deformation of an elastic body due to external or internal heat generation, or thermal stress, is called thermoelastic expansion, which is dependent on both its specific heat capacity and temperature distribution. The phenomenon of thermoelasticity encompasses the theories of heat conduction, thermal strains and stresses, and classical elasticity. A more specific form of thermoelastic expansion that indicates the utilization of optical radiation as a source is photothermoelastic expansion.

The other mechanisms of sound generation are volume expansion by either chemical reaction or a change of density arising from a phase change. An example of the latter is the conversion of liquid water to vapor, as it takes place in the fluid surrounding laser irradiated particles. (36) (37) Chemical reactions can give rise to volume expansions as a result of the production of gaseous products from condensed matter, as reported by Diebold, whereby audible sound is heard from laser irradiation of carbon suspensions. (38) (39) (40) In general, a volume expansion of a body results in a mechanical motion that generates sound.

Dielectric breakdown can result from highly intense radiation that converts matter into ionized gas, known as plasma, the fourth state of matter. The most common natural occurrence of dielectric breakdown is manifested in a bolt of lightning. The photoacoustic phenomenon that follows is a clap of thunder. In this case, sound is generated along the length of the lightning channel as the atmosphere is heated by the dielectric breakdown that is caused by electric discharge. (10) (33) (41)

Electrostriction is the deformation of a volume due to an applied electric or electromagnetic field. The applied field deforms the volume over which it is applied, causing molecules to move into or out of the field.

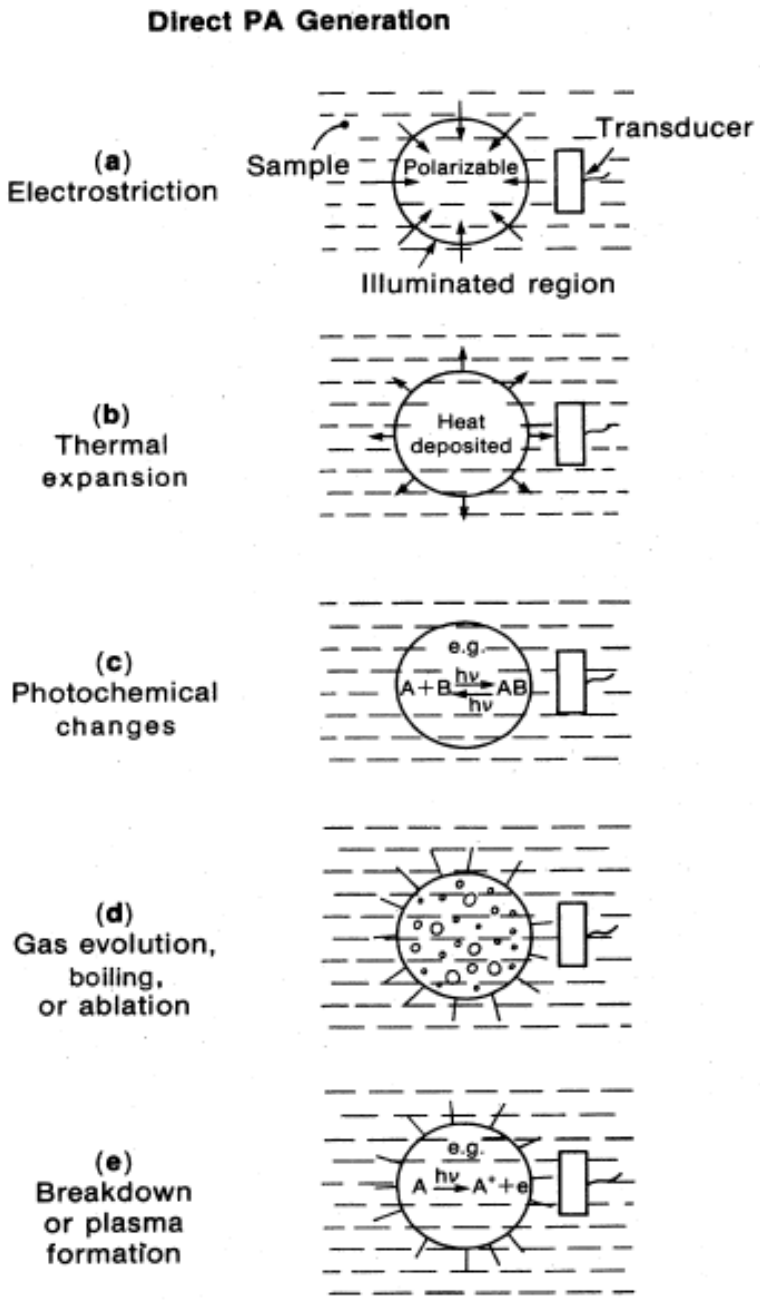

Figure 8: Some common photoacoustic generation mechanism, listed in typical order of efficiency, with the greatest generation efficiency given by method (e) from ref. **(42)**.

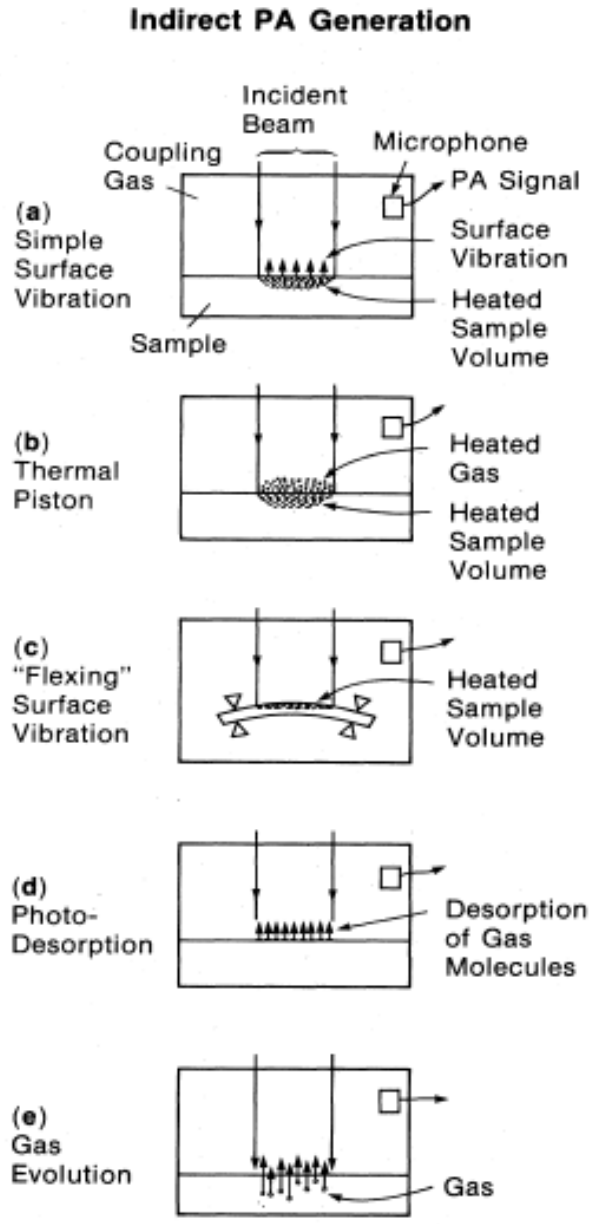

Figure 9: Various possible causes of indirect photoacoustic generation from ref. **(42)**.

Photoacoustic generation can be classified according to excitation modes: there is a continuous-wave (cw) modulation mode, whereby the excitation beam is modulated to have a nearly 50% duty cycle, and a pulsed mode, whereby the excitation beam is of very low duty cycle but high peak power. In the cw case, the signal is typically analyzed in the frequency domain; amplitude and the phase of one or several Fourier components are measured and narrow-band filters can be used to suppress noise. In the pulsed technique, however, the signal is acquired and analyzed in the time domain, making simple gating techniques for noise suppression possible. The features of the two photoacoustic techniques are indicated in Figure 10. The pulse mode will be discussed in the analysis of the experiment of Chapter 3.

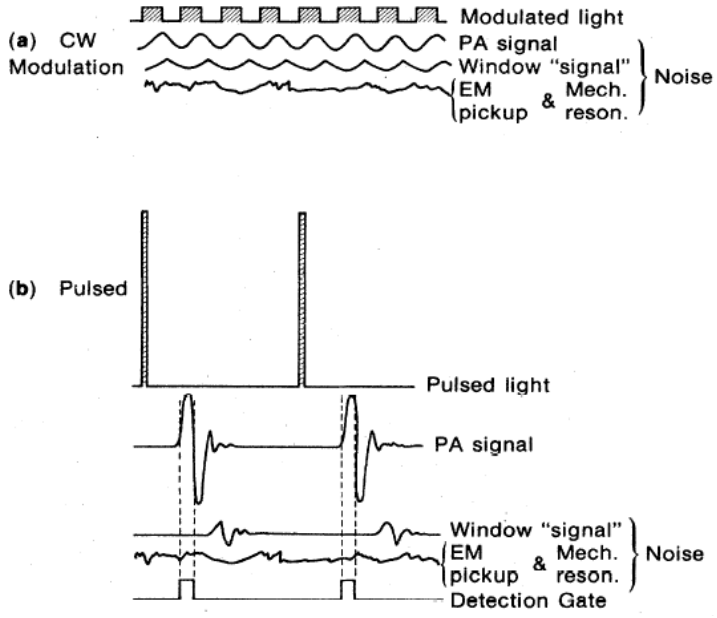

Figure 10: Schematic comparison of the cw modulated photoacoustic detection method (a) and the pulsed photoacoustic detection method (b) from ref. **(42)**.

(a) (b)

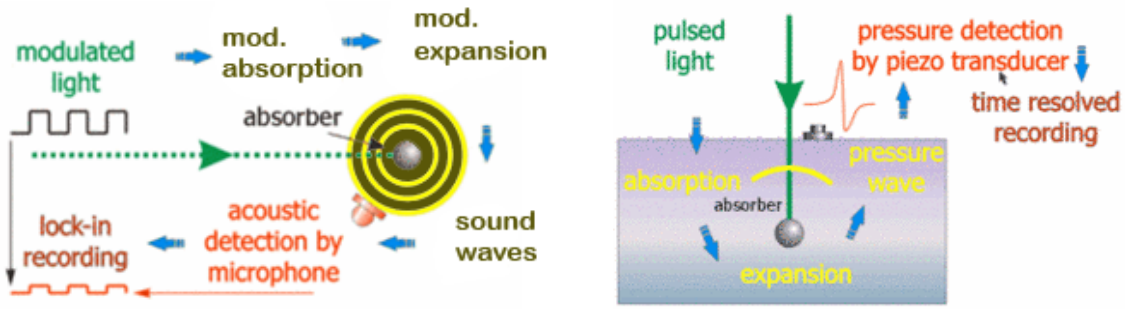

Figure 11: Principle of photoacoustic methods with (a) modulated light and (b) pulsed light source from ref. **(43)**.

Table 1: Comparison of cw Modulated and Pulsed Photoacoustic Techniques.

	cw modulated	Pulsed
Modulated intensity	High duty cycle, Low peak power	Low duty cycle, High peak power
Acoustic detection	Low frequency transducer and lock-in detector usually used	High frequency transducer and boxcar or transient recorder usually used
PA generation efficiency	Low	High
Thermal diffusion effects	May be important	Usually negligible
Acoustic boundary conditions	Important	Unimportant
Unmodulated background heating	Usually substantial	Usually small

Photoacoustic Cell

The photoacoustic cell is a container for the sample and for the microphone or transducer, such that the incident excitation beam is absorbed by the sample to produce an acoustic signal. The design of the photoacoustic cell is a critical element in achieving a good signal to noise ratio; it is vital to attain as close to perfect acoustic isolation from the outside world as possible. Photoacoustic cells may be classified into two general kinds: cells designed for gas samples, and those designed for condensed matter samples. The former generally utilize a microphone to sense the gas pressure fluctuations produced by the optical absorption; some examples are shown in Figure 12.

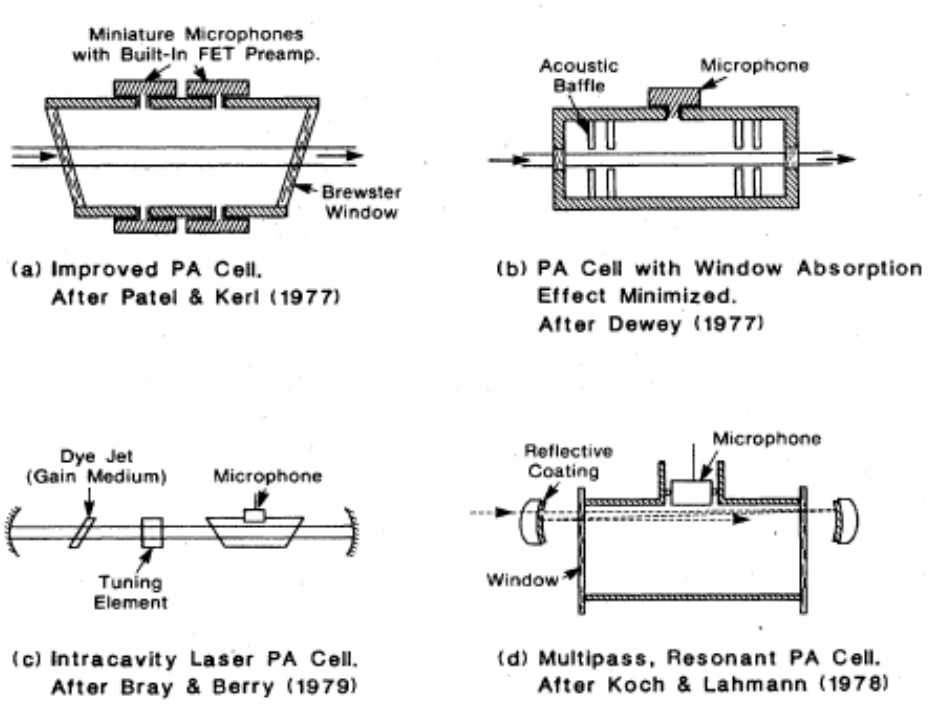

Figure 12: Examples of various photoacoustic cells for high-sensitivity detection in gases samples from ref. **(42)**.

In the second type of cells, for condensed matter, both microphones and piezoelectric transducers are used for detection. The microphonic detection schemes shown in Figure 13 (a) and (b) are based on the detection of the indirect photoacoustic signal due to thermal coupling from the sample into the gas, while the piezoelectric detection schemes illustrated in Figure 13 (c) and (d) are based on direct photoacoustic detection, usually providing a higher detection sensitivity. Figure 14 shows the various photoacoustic cells in Diebold's lab. Figure 14 (c) is based on Figure 13 (c) for the research of photoacoustic effect found in Chapter 3.

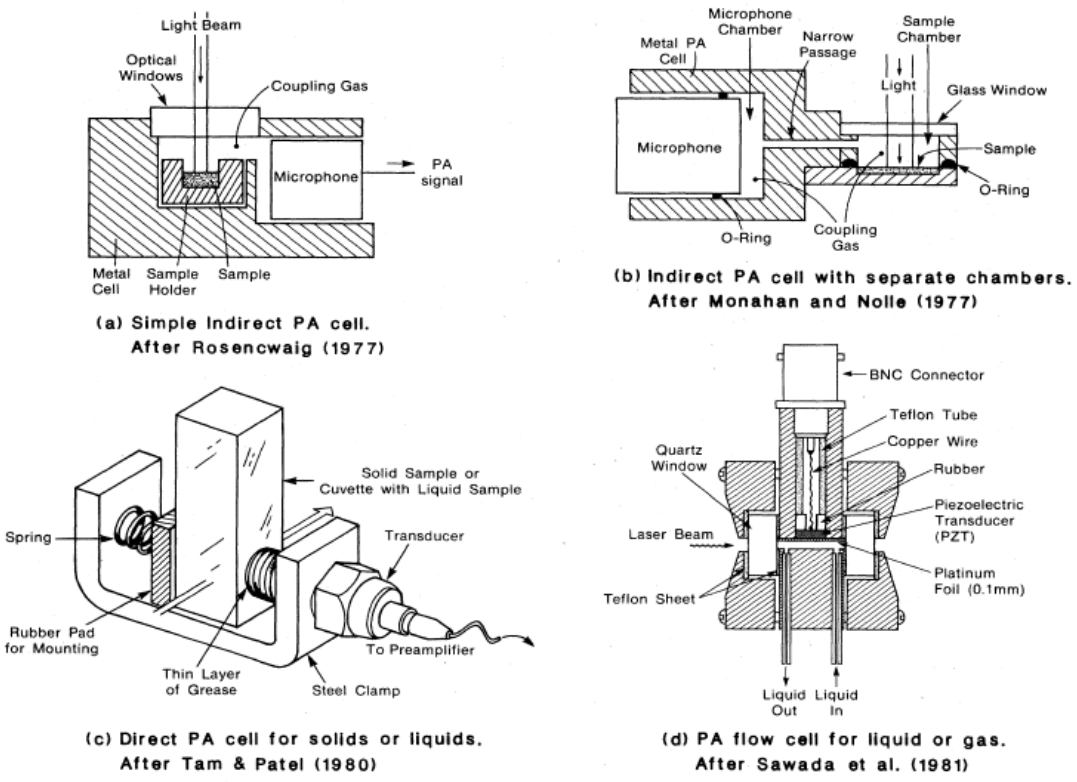

Figure 13: Example of various photoacoustic cells for condensed matter samples from ref. **(42)**.

(a) (b)

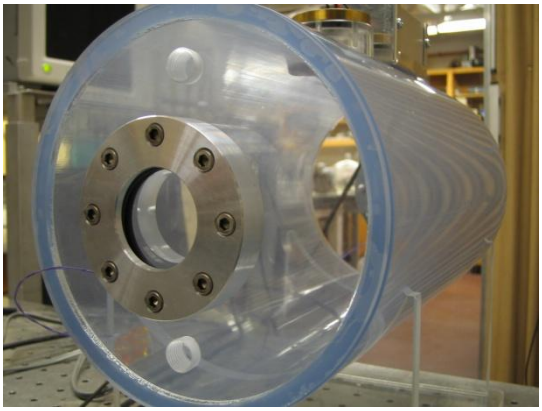

(c) (d)

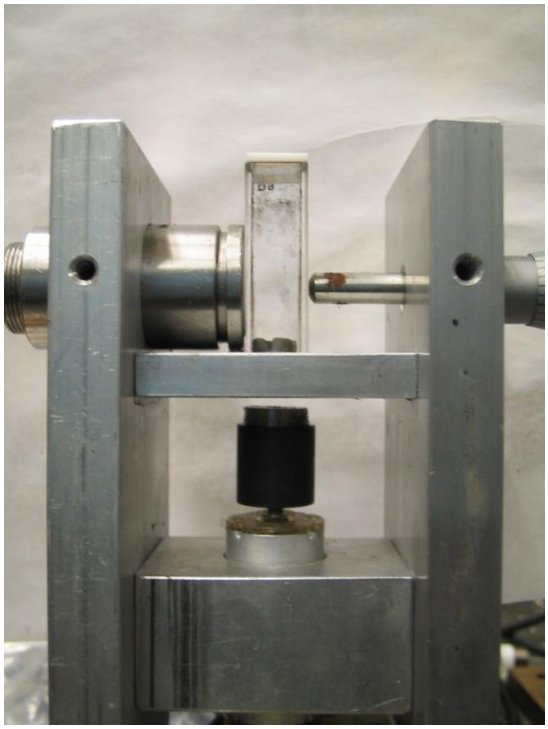

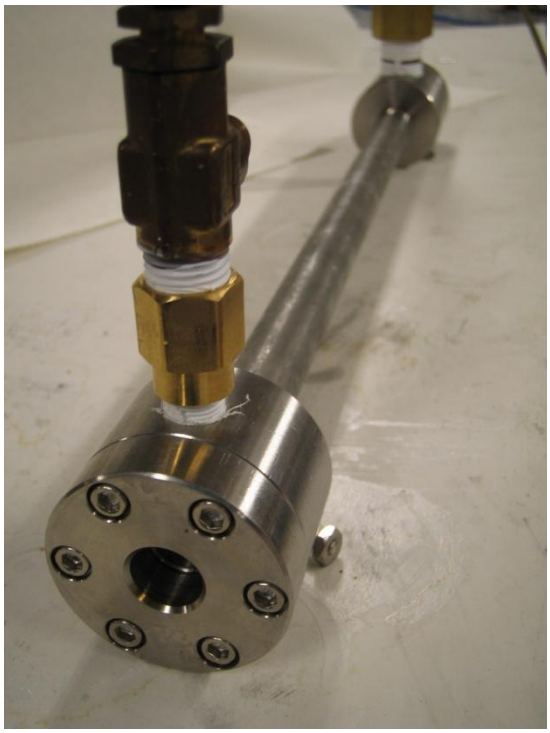

Figure 14: Various photoacoustic cells in Diebold's lab.

Generalized Photoacoustic Technique

The photoacoustic effect relies on the use of a modulated light beam as an excitation source for acoustic waves. To generalize, the excitation may be caused by any form of energy, such as radio waves or particle beams. The use of such other modulated excitation sources for acoustic generation is called the generalized photoacoustic technique, as summarized in Figure 15.

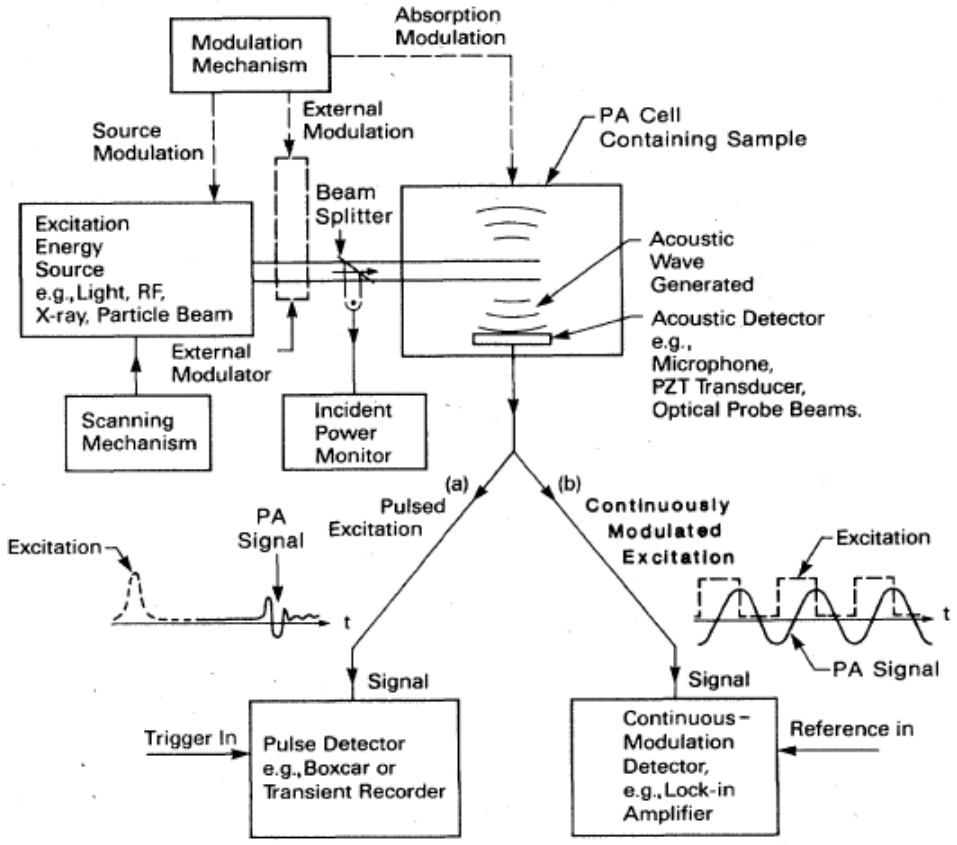

Figure 15: Schematic of the generalized photoacoustic generation and detection technique from ref. **(42)**.

Chapter 2 Sonoluminescence

2. 1 Historical Overview

Multi-Bubble Sonoluminescence

The term “Sonoluminescence” (SL) refers to the emission of bursts of light from imploding bubbles in a liquid when excited by sound. The effect was first discovered by H. Frenzel and H. Schultes in 1934. (44) They put an ultrasound transducer in a tank of photographic developer fluid in the hope of speeding up the development process because chemists of their time learned that a strong sound field could catalyze reactions that take place in an aqueous solution. Instead, they found tiny dots on the films after developing, and realized that the bubbles in the fluid were emitting photons when the ultrasound was turned on. Because of the complex environment, the strong sound field created a large number of short-lived bubbles that grew, collapsed and gave off light in an unpredictable and unsynchronized manner. This effect is called Multi-Bubble Sonoluminescence (MBSL). It is difficult to analyze the multi-bubble sonoluminescence and account for the lighting mechanism since it is impossible to track and study a single bubble from its creation to its collapse.

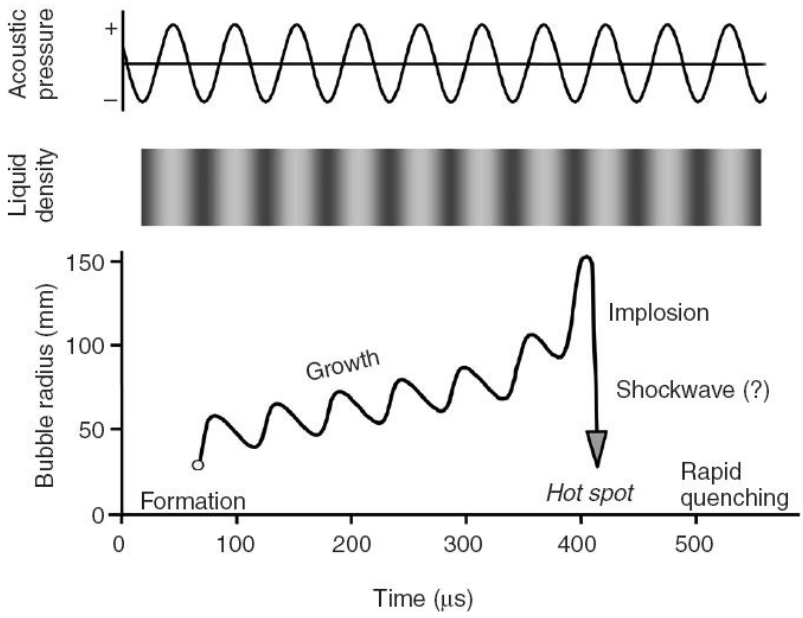

Figure 16: Transient acoustic cavitation: the origin of sonochemistry and sonoluminescence from ref. **(45)**.

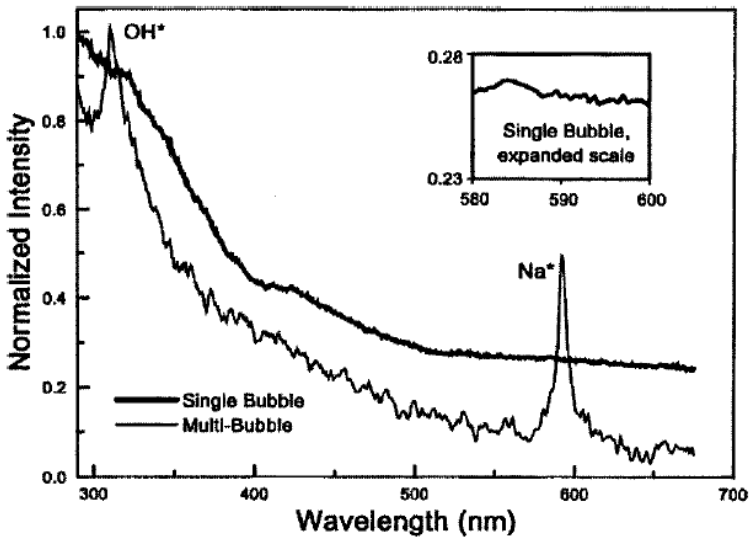

Figure 17: MBSL(thin line) and SBSL (thick line) spectra in a 0.1 M sodium chloride solution. Each spectrum was normalized to its hightes intensity. Note the prominence (MBSL) and absence (SBSL, see the inset for an enlargement) of the sodium line near 589 nm from ref. **(46)**.

Single-Bubble Sonoluminescence

In 1989, F. Gaitan and L. Crum showed that they could trap a single, light-emitting bubble in water that was partially degassed. (47) (48) This is the so called Single-Bubble Sonoluminescence (SBSL). In single-bubble sonoluminescence, a single bubble was trapped at a pressure antinode of an acoustic standing wave, undergoing strongly nonlinear oscillations and emitting a pulse of light during every acoustic cycle. In comparison with the bubbles in multi-bubble sonoluminescence, a single-bubble sonoluminescence bubble is quite stable and oscillates in a continuously repeating, predictable fashion for billions of acoustic cycles, thus allowing a more systematic study of the phenomenon. Hereafter all sonoluminescence in this thesis refers to single-bubble sonoluminescence.

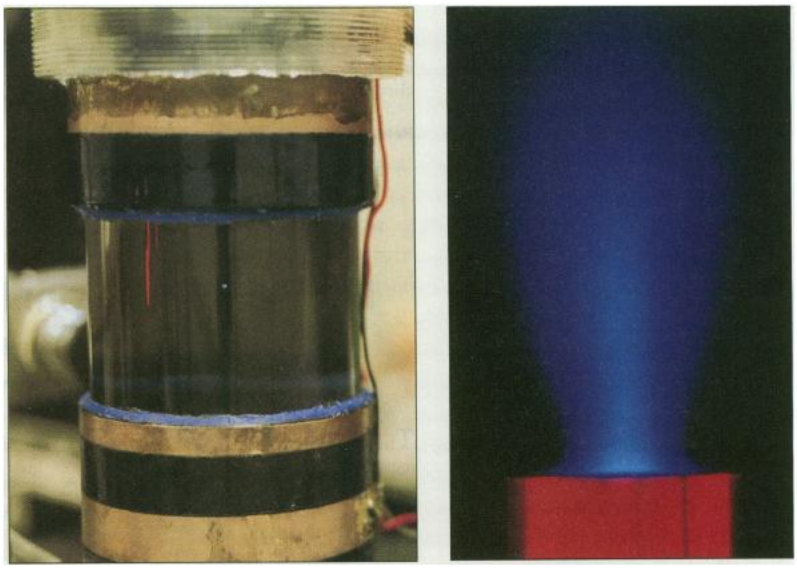

Figure 18: Bright bubbles. An acoustic standing wave levitates a small gas bubble near the center of a glass cell (left) and drives that bubble to radial excursions of sufficient amplitude to generate sonoluminescence on each acoustic cycle. Note the bright spot at the center of the cell, which can easily be seen without darkening the room; no chemical enhancement is required. In an example of multi-bubble sonoluminescence (right), the intense sound field near the tip of an acoustic source produces many transient cavitation bubbles that grow and collapse with such violence that they heat their respective interiors to incandescence from ref. **(48)**.

Most single-bubble sonoluminescence is achieved by acoustically exciting the fundamental mode of the acoustic resonator. The frequency of single-bubble sonoluminescence is that of the sinusoidal driving sound, typically 20 – 40 kHz, while the frequency of multi-bubble sonoluminescence is typically in the megahertz region.

Figure 19 shows the extraordinary range of length and time scales characterizing sonoluminescence. Trace "b" is the sound field near the center of a flask containing partially degassed water, driven (sinusoidally) at its acoustic resonance (which is about 26 kHz in this case). The acoustic radiation pressure of the sound field traps a gas bubble at the pressure antinodes in the center of the flask, where it pulsates in response to the pressure swings of the drive. These pulsations are displayed in trace "a", which shows the amount of light scattered out of a probe laser beam trained on the bubble. The general rule is; the larger the negative signal, the larger the bubble radius. The expansion of the bubble from its ambient radius (- 4.5 μm) occurs on hydrodynamic time scales during the rarefaction half-cycle of the pressure swing. It brings the bubble to its maximum radius of about 45 μm. The ensuing collapse accelerates the bubble wall to supersonic velocities and compresses the bubble's interior. The high stresses and high-energy densities inside the bubble generated by this collapse result in the emission of a flash of light (in trace "c"). The high pressures built up inside the bubble during the collapse launch an outgoing acoustic pulse, which is the spike riding the sound field in trace "b".

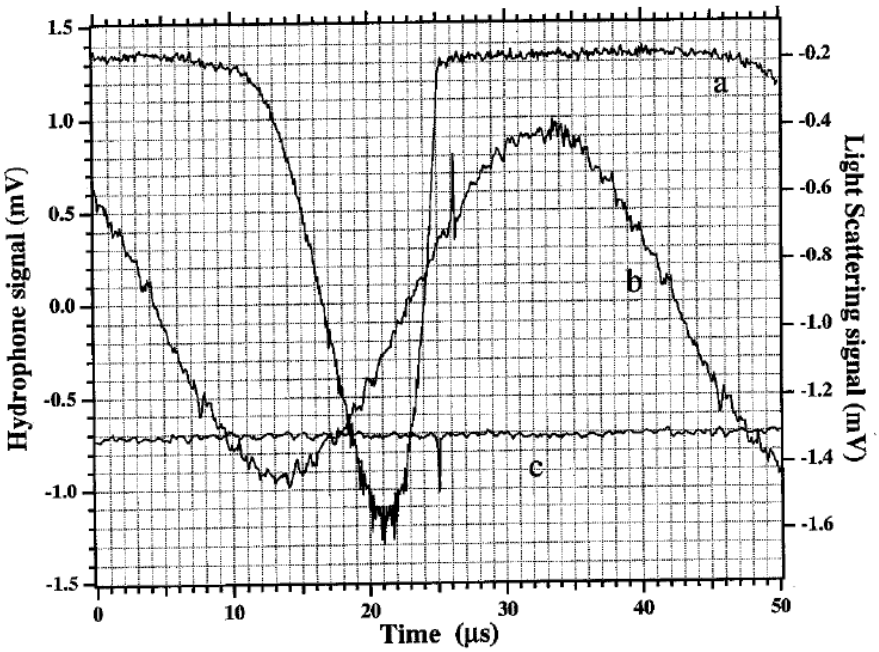

Figure 19: Relative timing of sonoluminescence (c) from the stressed interior of a collapsing air bubble whose radius squared is proportional to the magnitude of the intensity of scattered laser light (a). The high pressures reached during the collapse launch an outgoing spike recorded by a microphone that measures the driving sound field (b) inside the acoustic resonator from ref. **(49)**.

In general, during each acoustic cycle, the bubble expands from its ambient (undriven) radius of $R_0 \sim 5\ \mu$m to its maximum radius of $R_{max} \sim 50\ \mu$m during the rarefaction half cycle, then collapse very rapidly to a minimum radius of $R_{min} \sim 0.5\ \mu$m, changing its volume by a factor of 10^6. (49) (50) This collapse happens so fast that the bubble wall is accelerated to supersonic velocity and compresses the bubble's interior, (51) (52) (53) resulting in temperature in excess of 10^5 K and pressures in excess of 10^7 bar, (48) and concentrating the energy by 12 orders of magnitude.

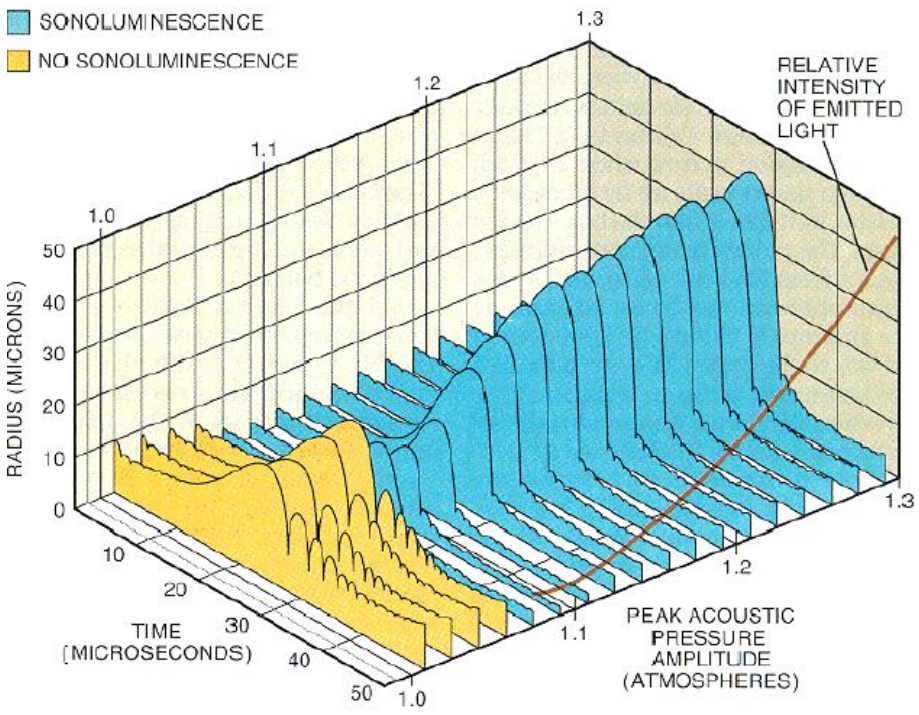

Figure 20: Transition to sonoluminescence happens when the sound level reaches a critical state. The average radius of a bubble generally increases with a rise in acoustic amplitude. At the level at which sonoluminescence begins, however, the radius suddenly shrinks. The mechanism behind this transition is not understood from ref. **(54)**.

Initially, scientists thought the pulse width of the single-bubble sonoluminescence should be less than 50 ps, (49) while more recent measurements of the pulse width of single-bubble sonoluminescence showed it to be in a range of 35 -300 ps. In 1997, Gompf et al. found the pulse width of single-bubble sonoluminescence of an air bubble to be about 60 ps at low gas concentrations and low driving pressures, and more than 250 ps at high gas concentrations and high driving pressures at the upper sonoluminescence threshold. (55) The pulse shape is near Gaussian and is identical in the red and UV part of the spectrum.

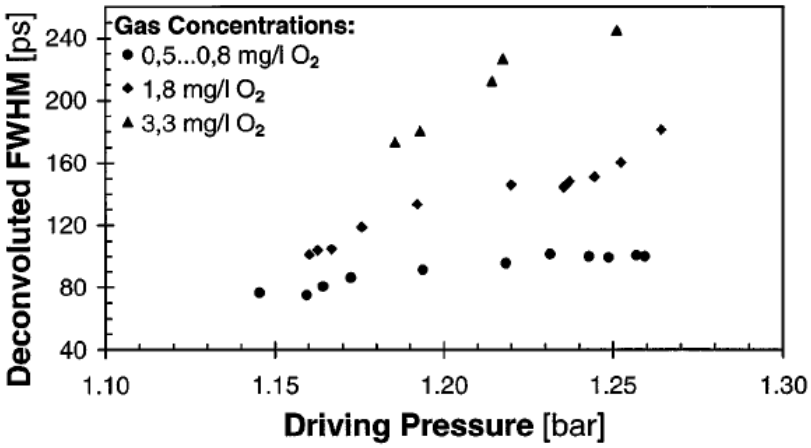

Figure 21: Dependence of the FWHM of the sonoluminescence pulse width on driving pressure and gas concentration at room temperature from ref. **(55)**.

Single-bubble sonoluminescence is sensitive to various experimental parameters. It is brighter at lower ambient temperatures. (56) But there have been mixed results for sonoluminescent brightness at lower ambient pressures. Dan et al. reported a roughly sevenfold increase in sonoluminescent intensity when the ambient pressure over a 25 wt. % degasses/glycerine mixture was decreased from 1.00 atm to 0.90 atm, (57) while Putterman et al. observed that the maximum sonoluminescent intensity decreases as the ambient pressure over a mixture of ethylene glycol and water is lowered below 1 atm. (58)

Differing contents of a gas bubble result in different sonoluminescent intensity and spectrum. Hiller et al. discovered that the sonoluminescent intensity can be greatly enhanced by adding a small amount of noble gas into the bubble, while both a gas bubble without noble gas contents and a pure noble gas bubble result in a weaker sonoluminescence. (59)

Water has been proven to be the friendly host liquid for sonoluminescence. It seems that adding certain surfactants (e.g. Triton X-100) into water facilitates the interfacial motion and results in weaker sonoluminescence, while adding some other surfactant (e.g. bovine serum albumin, glycerol, etc.) into water hinders the interfacial motion and results in brighter sonoluminescence. (60) (61) Suslick et al. discovered the generation of extremely intense single-bubble sonoluminescence in 85 wt. % H_2SO_4 aqueous solution, more than 1000 times brighter compared to the sonoluminescent intensity in water. (62)

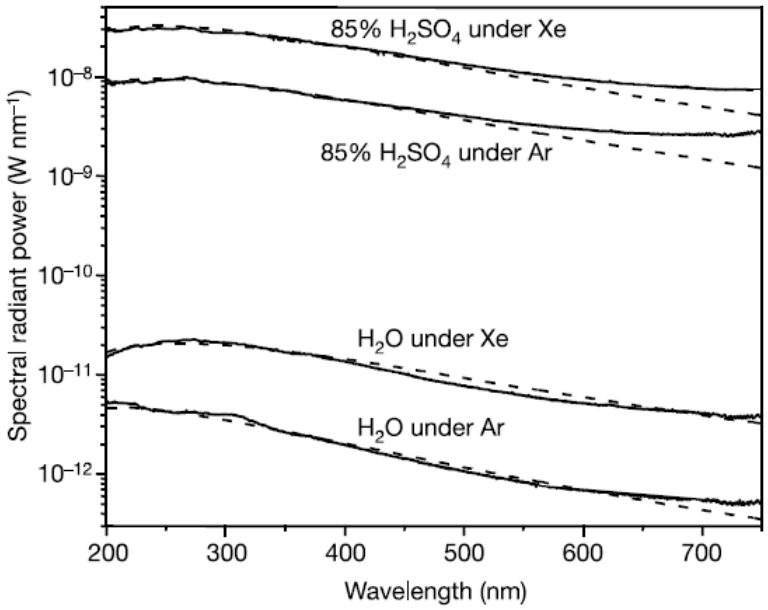

Figure 22: Single-bubble sonoluminescence spectra from 85% H_2SO_4(aq.) and pure water regassed with Xe and Ar (solid lines); apparent fits to blackbody spectra are given as dashed lines from ref. **(62)**.

2. 2 Application of Sonoluminescence and Nuclear Fusion

Sonoluminescence can be applied to sonochemistry, (63) sonophotoluminescence, (64) biology (65) and even medicine. (66) Above all, the most exciting application for sonoluminescence could possibly be nuclear fusion. Taleyarkhan et al. reported that they have found the experimental evidence of nuclear fusion inside a sonoluminescencing air bubble in deuterated acetone. (67) However, this result prompted a strong debate within the scientific community, and an attempt to repeat the experiment by various groups found no evidence of nuclear fusion. (68) Finally, he was judged guilty of research misconduct for "falsification of the research record" by a Purdue University review board in 2008. (69) (70)

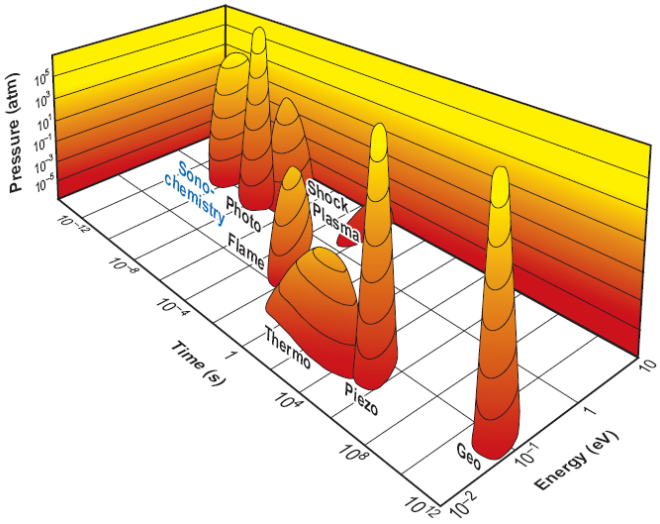

Figure 23: Chemistry is, fundamentally, the interaction of energy and matter. The parameters that control that interaction are the amount of energy per molecule, the time of the interaction, and the pressure under which that interaction occurs. This schematic represents the distinct domains of chemistry. Acoustic cavitation and its consequent sonochemistry provide an unusual method to access a unique parameter space for exploring new and interesting chemistry and physics from ref. **(71)**.

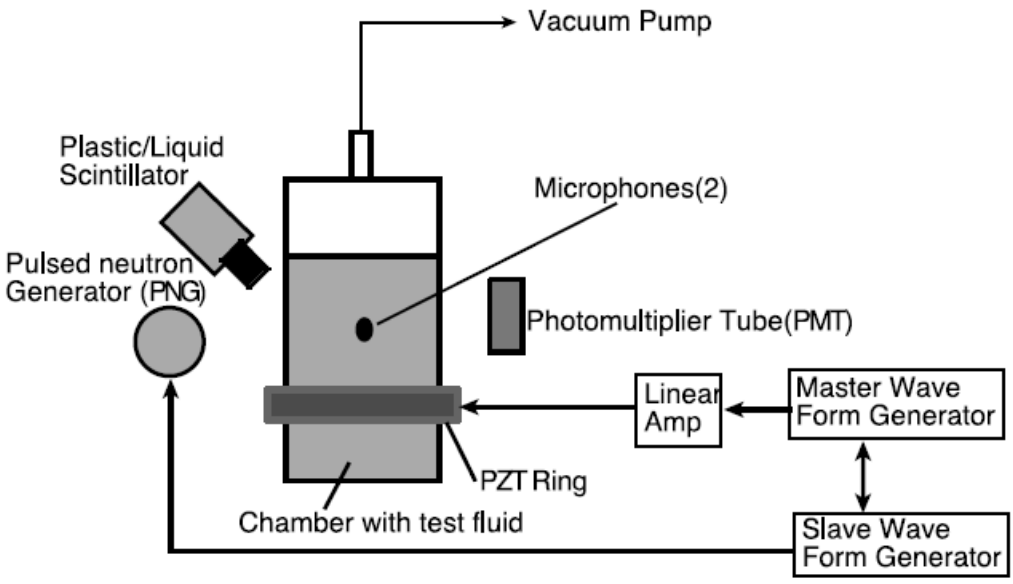

Figure 24: Schematic of Taleyarkhan's experimental setup from ref. **(67)**.

2. 3 Theories of Sonoluminescence

There have been dozens of theories of sonoluminescence, but most of the theories are now discounted, as they cannot explain all the modified properties of sonoluminescence. Only a couple of theories remain interesting: one is the hot spot (black body) theory; (72) the other is the shock wave theory. (51) (73) In the hot spot model, the energy for the light emission is supplied by thermal energy resulting from an adiabatic bubble collapse. In 1950, Rayleigh-Plesset bubble dynamics was used to deduce bubble internal temperatures as high as 10,000 K at the moment of the collapse of a spherically symmetric bubble. (74) Within the hot spot models, the question of which process of light emission will dominate depends on the actual maximum temperatures reached, e.g., recombination of dissociated molecules at lower temperatures, or characteristic molecular radiation due to electronic excitation, in particular of the OH radical. The latter was referred to as chemiluminescence by Suslick and must not be confused with secondary chemiluminescence, which may occur in the liquid as a result of chemical reactions of the radical molecules generated in the bubble collapse.

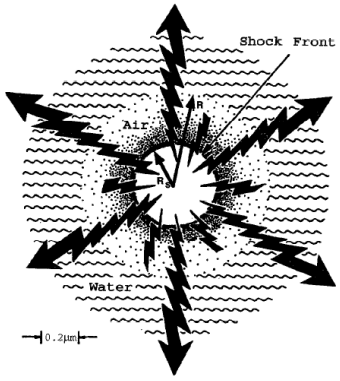

Figure 25: Sketch of an imploding shock wave model of sonloluminescence. The shock is launched by the supersonic motion of the bubble wall. The radius of the gas water interface is R and the radius of the shock is R_s. The shock first implodes to a focus and then explodes. This figure depicts the state reached about 100 ps after focusing from ref. **(49)**.

2. 4 Temperature of Sonoluminescence

The temperature predicted inside the sonoluminescing bubble varies from a few thousand K to hundreds of millions K. (75)

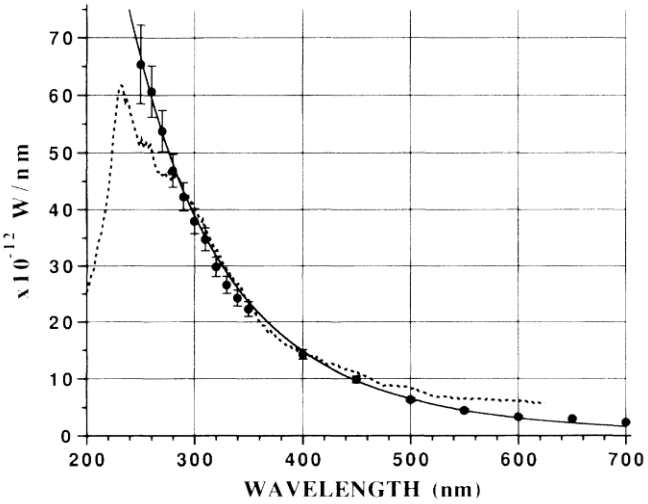

Figure 26: Calibrated spectral power density of the synchronous picosecond flashes of sonoluminescence. The solid line is a 25,000 K blackbody spectrum from ref. **(75)**.

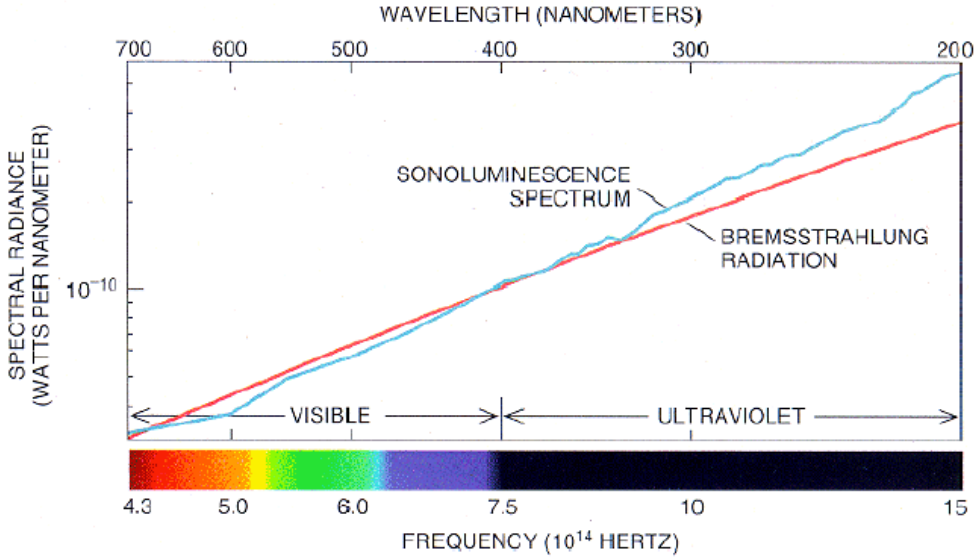

Figure 27: Spectrum of sonoluminescence shows that most the emitted light is ultraviolet. The signal compares closely with bremsstrahlung radiation- that is, light emitted by plasma at 100,000 K from ref. **(54)**.

2. 5 Generation of Cavitation

There are several ways to generate cavitation for sonoluminescence. The term "sonoluminescence" was introduced, because cavitation was generated by the acoustic sound field. Cavitation generated with transducer is the most common method of generating cavitation. Pulsed laser with a focusing lens can vaporize liquid and make bubbles. Also, chemically generated bubbles can make sonoluminescence. (76)

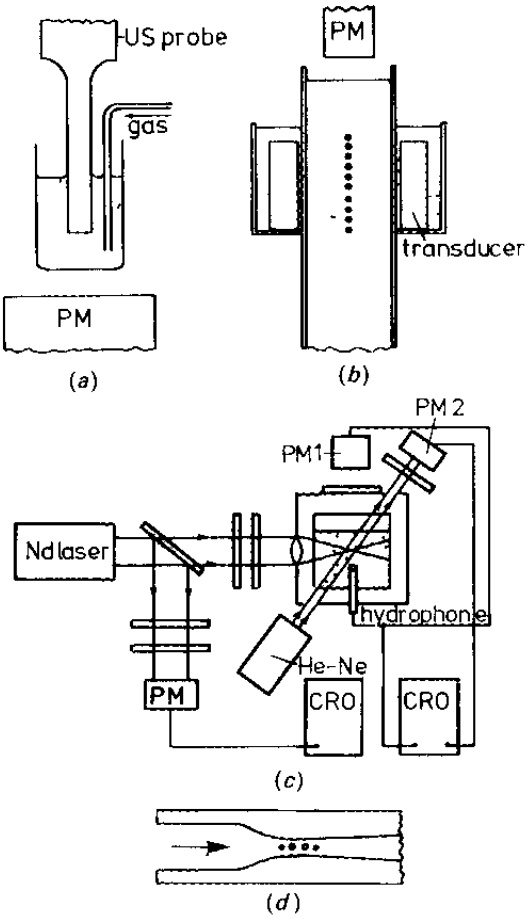

Figure 28: Generation of cavitation. (a)(b) Acoustic cavitation, (c) Optic cavitation, and (d) Hydrodynamic cavitation from ref. **(77)**.

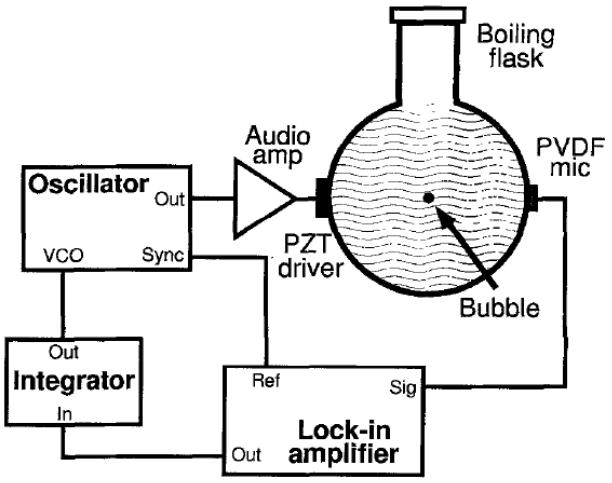

Figure 29: Basic apparatus for generating and modelocking sonoluminescence from ref. **(49)**.

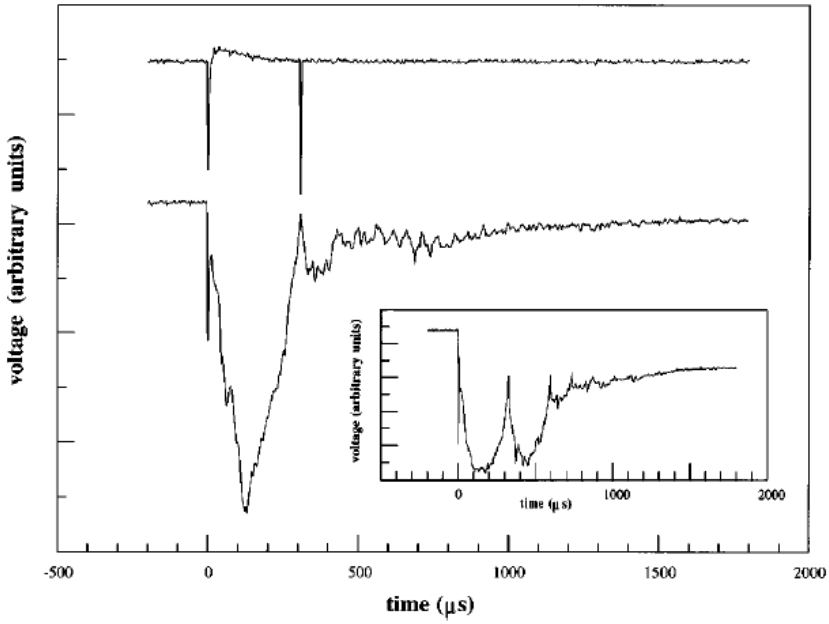

Figure 30: Chemical generation of sonoluminescence from ref. **(76)**.

Laser-induced chemical reactions produce gas bubbles and their collapse makes sonoluminescence. With the Carbon-Steam Reaction, carbon suspension produces hydrogen and carbon monoxide. These bubbles collapse after about 300 microseconds and emit the light as shown in Figure 30.

2. 6 Mie Scattering

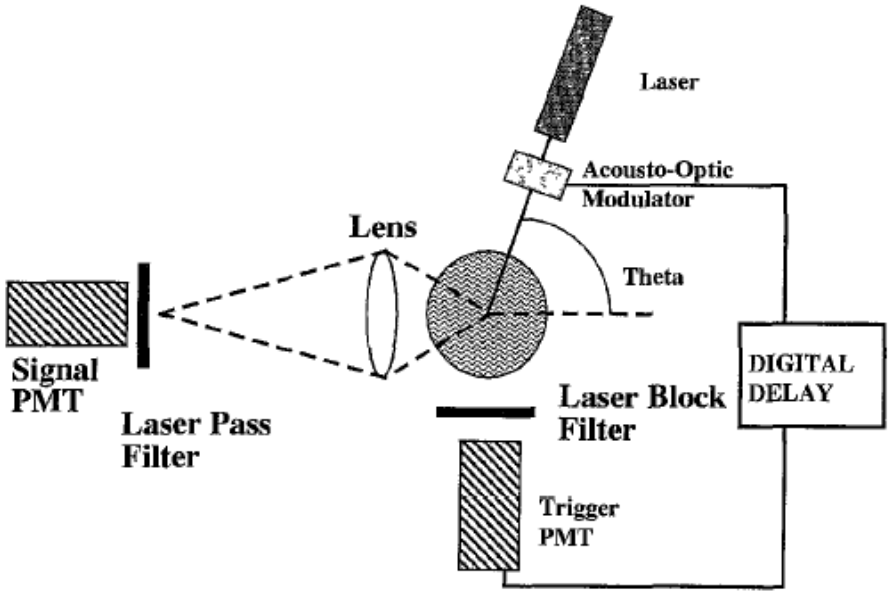

Figure 31: Apparatus for Mie scattering measurements of a sonoluminescing bubble. Detected intensity is proportional to the square of the radius of the bubble from ref. **(49)**.

Knowledge of bubble radius as a function of time constitutes an essential parameter in characterizing sonoluminescence. Mie scattering has proven to be a valuable technique for measuring radii. In this approach, laser light with a beam width larger than the bubble's radius is trained on the bubble. The light scattered within a given large angle is simply proportional to radius squared.

2. 7 Rayleigh-Plesset Equation

The Rayleigh-Plesset equation (RPE) explains the radial motion of an acoustically driven bubble. Rayleigh-Plesset equations can vary in complexity and have been elaborated using contributions from many researchers. An example of an Rayleigh-Plesset equation is in Equation 1:

$$R\ddot{R} + \frac{3}{2}\dot{R}^2 = \frac{1}{\rho}\left[\left(P_0 + \frac{2\sigma}{R_0}\right)\left(\frac{R_0}{R}\right)^{3\gamma} - \frac{2\sigma}{R} - \frac{4\mu\dot{R}}{R} + P_\infty\right] \quad (1)$$

where R is the bubble radius [the overdots signify first (velocity) and second (acceleration) derivatives of the interface with respect to time], R_0 is the bubble radius at ambient conditions, ρ is the bulk liquid density, P_0 is the ambient liquid pressure, σ is the surface tension, μ is the shear viscosity, and P_∞ is the far-field acoustic pressure. The left-hand side of Equation 1 describes the inertial characteristics of the bubble interface, and equating this to $\frac{P_L - P_\infty}{\rho}$, where P_L is the pressure in the liquid at the bubble wall, gives the fundamental equation of bubble dynamics. The term $\left(P_0 + \frac{2\sigma}{R_0}\right)\left(\frac{R_0}{R}\right)^{3\gamma}$ represents the intracavity gas pressure as the bubble radius varies from R_0 to R. Rayleigh-Plesset equations work well over most of the range of bubble motion; any Rayleigh-Plesset equation assumes, however, that the density of the liquid is very large compared with the density of the gas within the bubble. This assumption fails in the case of a strongly driven bubble as it rapidly approaches its minimum radius.

2. 8 Minnaert Frequency

A bubble oscillator can be thought to be simple harmonic if one assumes a small amplitude oscillation and no dissipative loss (through viscosity, thermal condition, etc.). The restoring force is the "elasticity" of the gas; the "effective mass" is associated with the moving liquid surrounding the bubble. Without external driving forces, the bubble oscillates at its natural frequency, which is called the Minnaert Frequency.

Analogously to a simple harmonic motion, where energy is changed between kinetic energy and potential energy and the maximum kinetic energy equals the maximum potential energy, a simple harmonic bubble oscillator changes energy between the internal energy of the gas in the bubble and the kinetic energy of the liquid surrounding the bubble, and the maximum kinetic energy of the surrounding liquid equals the maximum internal energy of the gas. Since we assume the bubble oscillation to be simple harmonic, the bubble radius can be written as

$$R(t) = R_0 + R_\epsilon(t) \tag{2}$$

$$R_\epsilon(t) = -R_{\epsilon_0}\, e^{i\omega_o t} \tag{3}$$

where R_0 is the equilibrium radius, ω_0 is the nature resonance frequency and $R_{\epsilon 0}$ is the amplitude of bubble oscillation. The negative sign is used to show an increase in pressure, causing a decrease in bubble radius. The kinetic energy of the surrounding liquid is found by integrating over the shells of liquid from the bubble wall to infinity. A given shell at radius r with thickness dr moves with speed of $\dot{r}$ and has mass of $4\pi r^2 \rho dr$

where ρ is the density of the liquid. Therefore the kinetic energy E_k of the surrounding liquid is

$$E_k = \frac{1}{2} \int_R^\infty 4\pi^2 \rho \, \dot{r}^2 \, dr \tag{4}$$

If the liquid is assumed to be incompressible, at any instant the rate of mass of liquid flowing through any spherical surface (radius r) equicentric with the cavity must be a constant. The mass flow rate across a surface at some general radius r outside the cavity (given by $4\pi r^2 \rho \dot{r}$) must equal the flow rate at the cavity wall (given by $4\pi R^2 \rho \dot{R}$):

$$4\pi r^2 \rho \dot{r} = 4\pi R^2 \rho \dot{R} \;\Rightarrow\; \frac{\dot{r}}{\dot{R}} = \frac{R^2}{r^2} \tag{5}$$

This is also called the *liquid incompressibility condition*. The substitution of the relation $r^2 \dot{r} = R^2 \dot{R}$ into Equation 4 gives

$$E_k = \int_R^\infty 2\pi \rho R^4 \, \dot{R}^2 \frac{dr}{r^2} = 2\pi R^3 \rho \dot{R}^2 \tag{6}$$

Similar to a simple harmonic spring-bob system, E_k is maximum at the equilibrium position where $R=R_0$ and $\dot{R} = i\omega_0 R_{\epsilon 0} e^{i\omega_0 t}$. Thus

$$E_{k,max} = 2\pi R_0^3 \rho (\omega_0 R_{\epsilon 0})^2 \tag{7}$$

The internal energy of the gas in the bubble is converted from the work done by compressing the bubble from equilibrium volume V_0 (radius R_0) to the maximum volume $V_{\min}$ (radius R_0 - $R_{\epsilon 0}$), that is

$$E_{p,max} = -\int_{V_0}^{V_{min}} (p_g - p_0)\, dV \tag{8}$$

where p_g is the pressure of the gas in the bubble at radius R, p_0 is the pressure of the gas in the bubble at radius R_0. If we assume the gas behaves polytropically so that pV^k=constant, we have

$$p_g (R_0 + R_\epsilon)^{3k} = p_0\, R_0^{3k} \tag{9}$$

or

$$\frac{p_g}{p_0} = \left(1 + \frac{R_\epsilon}{R_0}\right)^{-3k} \tag{10}$$

Since a small-amplitude oscillation is assumed, $R_\epsilon/R_0 << 1$. Approximating the right hand side of Equation 10 to its first order gives

$$\frac{p_g}{p_0} = 1 - 3k\frac{R_\epsilon}{R_0} \tag{11}$$

or

$$p_g - p_0 = -\frac{3kR_\epsilon p_0}{R_0} \tag{12}$$

Substitution of this into Equation 8 gives

$$E_{p,max} = \int_{V_0}^{V_{min}} \frac{3kR_\epsilon p_0}{R_0}\, dV = \int_{R_0}^{R_0 - R_{\epsilon_0}} \frac{3kR_\epsilon p_0}{R_0} 4\pi R^2 dR \tag{13}$$

Substitution of $R = R_0 + R_\epsilon$ and applying the condition $R_0 + R_\epsilon \approx R_0$ ($R_\epsilon << R_0$) gives

$$E_{p,max} = \int_{R_0}^{R_0 - R_{\epsilon_0}} \frac{3kR_\epsilon p_0}{R_0} 4\pi(R_0 + R_\epsilon)^2 d(R_0 + R_\epsilon)$$

$$\approx \int_0^{R_{\epsilon_0}} \frac{3kR_\epsilon p_0}{R_0} 4\pi R_0^2 dR_\epsilon = 6\pi k p_0 R_0 R_{\epsilon_0}^2 \quad (14)$$

Equating $E_{p,max}$ from Equation 14 to $E_{k,max}$ from Equation 7 gives the natural frequency (termed Minnaert frequency) of the bubble oscillator

$$\omega_0 \approx \frac{1}{R_0}\sqrt{\frac{3kp_0}{\rho}} \quad (15)$$

Chapter 3 Effects of exothermic chemical reaction on photoacoustic effect from particulate matter

3. 1 Introduction

Suspension of small carbon particles in fluids can have sufficiently large optical absorption cross sections that upon irradiation of the suspension with a high power pulsed laser, (78) (79) the surfaces of the particles can be driven to sufficiently high temperatures so as to initiate chemical reactions at the particle-fluid interface. (80) When a suspension of carbon particles in water is irradiated with the output of a high power pulsed laser, many surprising effects take place. Some of the phenomena associated with this interaction include: the chemical synthesis of gas (38) (81) and liquid phase products, the production of diffuse white light, and the generation of a large audible sound. (38) Other effects include the generation of sonoluminescence, (76) and the rapid formation of vapor bubbles around carbon particles. (82) (83) Optical limiting effects (84) and the

generation of shock waves have also been reported (85) to take place in irradiated suspensions of carbon particles.

This chapter describes the exothermic chemical reactions that take place when particulate suspensions of carbon particles in water, hydrogen peroxide, and nitromethane are irradiated with the output of a Q-switched Nd:YAG laser. The effect of reaction exothermicity and laser energy is reported.

Irradiation of carbon suspensions in water with a few hundred mJ of 1064 nm radiation raise the temperature of the particles to sufficiently high temperatures to initiate chemical reaction at the particle-water interface. This leads to the formation of permanent gas above the suspension that is made up of CO, H_2 and numerous hydrocarbons. The production of carbon monoxide and hydrogen from carbon and water is known as the Carbon-Steam Reaction: (86)

$$C\ (s) + H_2O\ (l) \rightarrow CO\ (g) + H_2\ (g) \qquad (16),$$

which reaction is highly endothermic (175 kJ/mol). In industry, carbon in the form of coal or coke, is usually heated to temperatures above 850 °C. CO and H_2 are the desired products from this reaction, but depending on the operation conditions used, CO_2 and CH_4 can also be found in the product stream. The formation of CO_2 can be attributed to the Gas-Shift Reaction: (86)

$$CO\ (g) + H_2O\ (l) \rightarrow CO_2\ (g) + H_2\ (g) \qquad (17)$$

At elevated pressures, and at temperatures less than 1150 °C, H_2 reacts with carbon to form CH_4. (87) Carbon hydrogenation reactions are believed to proceed by successive hydrogen additions at the edges of carbon crystallites. Mixtures of CO and H_2 in high concentrations are termed synthesis gas (generally shortened to syngas), a name that reflects the unique versatility of these two gases as chemical building blocks. The Carbon-Steam Reaction, also referred to as the Water-Gas Reaction, was used predominantly before World War II for producing hydrogen to be used in the manufacture of ammonia by the Haber process. (88) Synthesis gas produced from the Carbon-Steam Reaction was also used during the same time period to make liquid hydrocarbons via the Fischer-Tropsch method (86) but most of the plants used were phased out as low cost petroleum and natural gas became available in the late 1940's and early 1950's.

Strickland-Constable proposed that the reaction of carbon with water in the form of steam involves the following reactions: (89)

$$C_{act} + H_2O \rightarrow C(O) + H_2 \quad (18)$$

$$C(O) \rightarrow CO + C_{act} \text{ (or } C_{inact}) \quad (19)$$

C_{act} is an active site on the carbon substrate and C(O) represents an oxygen atom chemisorbed at an active site on the carbon surface. The proposed mechanism involves the chemisorptions of oxygen at an active site on the carbon surface (Equation 18),

followed by the desorption of CO and the generation of a new active or inactive ($C_{inactive}$) site as shown in Equation 19.

Although bubble formation (82) and permanent gas generation (85) have been previously observed when aqueous suspensions of carbon particles were irradiated, no exothermic chemical reaction to increase photoacoustic effects has been reported. What follows is a systematic and thorough investigation into the physical and chemical effects that take place when a suspension of carbon particles in water, hydrogen peroxide, and nitromethane are irradiated with the output of a high-power pulsed laser.

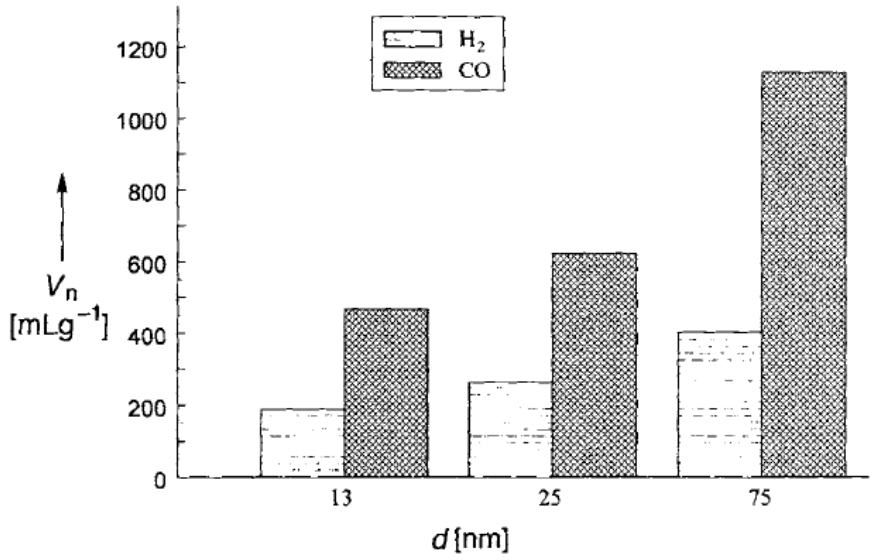

Figure 32: Laser-initiated Carbon-Steam Reaction. H_2 and CO content of the evolved gas in milliliters of gas per gram of carbon in the suspension versus particle diameter from ref. (81).

3. 2 Data of Photoacoustic Effect

Experimental Setup

Experimental apparatus here was based on the traditional photoacoustic cell design discussed in Figure 14 (c) of Chapter 1. Experiments were carried out to determine the influence of exothermic chemical reactions on the production of the photoacoustic effect. The apparatus consisted of a glass cuvette filled with a carbon suspension made in mixtures of H_2O with H_2O_2 into which a Q-switched Nd:YAG laser with a 10 ns pulse width was directed. The laser fundamental at 1064 or its frequency doubled output at 532 nm was used to irradiate the suspensions. The laser beam was 1 cm in diameter. In Experimental Setup 1 as shown in Figure 34, a polyvinylidene film transducer was placed in contact with the cuvette at perpendicular incidence to the direction of the propagation of the laser beam to record the acoustic wave. In Setup 2 as shown in Figure 35, a piezoelectric transducer was placed in contact with flat glass and optical filter. The transducer was attached to a 1 MΩ input impedance amplifier with a gain of 20 dB whose output was fed to a fast oscilloscope. H_2O_2 was prepared by bubbling dry N_2 into commercially obtained (Sigma-Aldrich) 50% by weight H_2O_2 in water to yield higher concentrations of the peroxide. (90) Lower concentrations of H_2O_2 were made by dilution of the stock solution with distilled water. The weight percentages of H_2O_2 were determined from density measurements. Carbon suspensions were made from particulate carbon black (Cabot, Black Pearls 1300) that were nominally 13 nm in diameter.

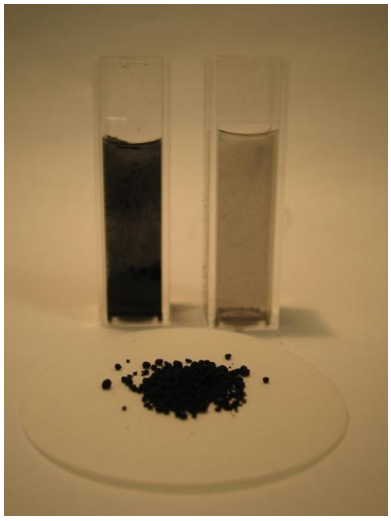

Figure 33: Particulate carbon black.

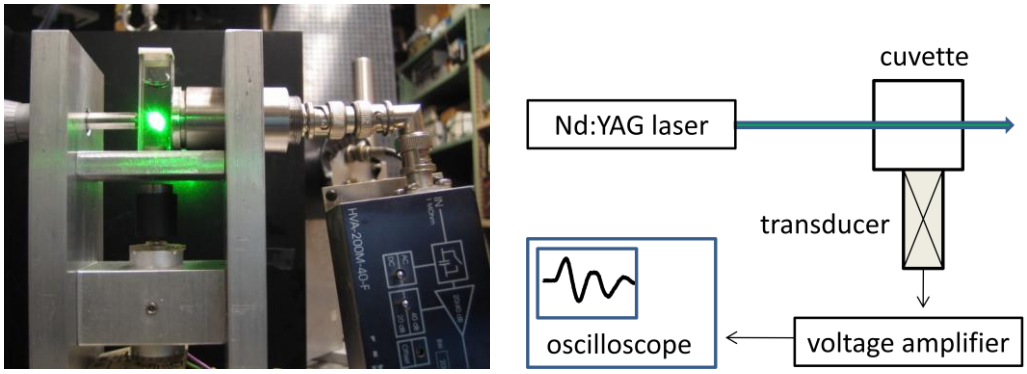

Figure 34: Experimental apparatus 1.

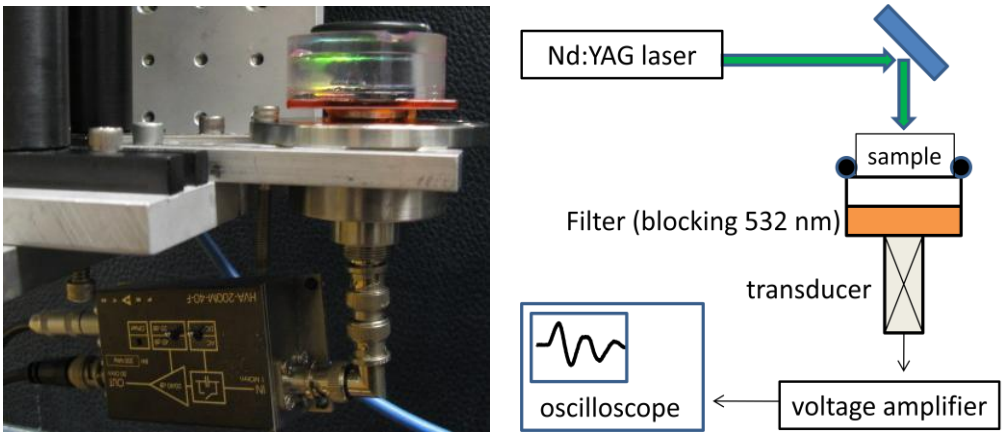

Figure 35: Experimental apparatus 2.

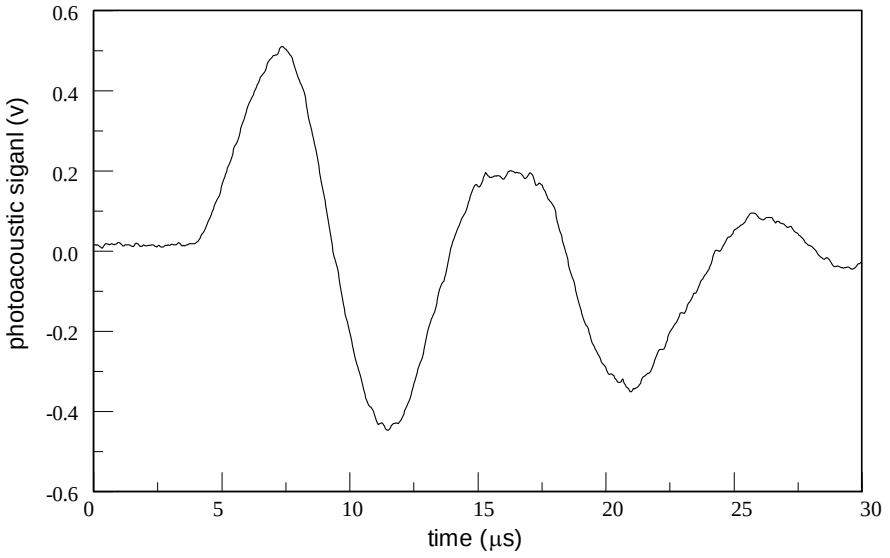

1

Figure 36: Photoacoustic signal from carbon suspension in 75% H_2O_2 with 532 nm and 0.5 J laser irradiation. The peak height of the first pulse is what is referred to here as the photoacoustic signal amplitude.

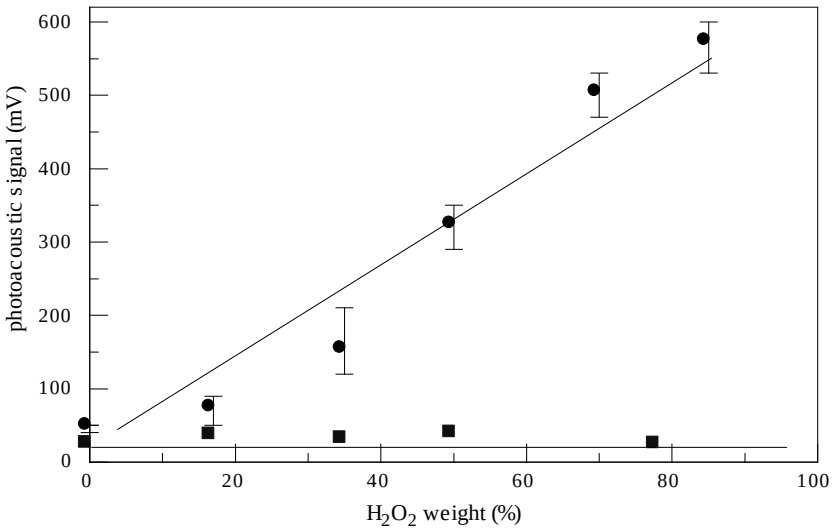

Figure 37: Upper curve: photoacoustic signal versus weight percentage of H_2O_2 in mixtures of colloidal C with H_2O_2 and H_2O. The error bars correspond to the root mean square deviations from the averages of several experiments. Lower curve: photoacoustic signal from a SiC suspension. The suspensions were adjusted to have an absorption coefficient of 0.25 cm^{-1} at the laser wavelength, 532 nm. The laser beam energy was 0.5 J per pulse.

The Effect of H_2O_2 on the Photoacoustic Signal Amplitude

Figure 37 shows the effect of changing the concentration of H_2O_2 on the photoacoustic signal amplitude for suspensions of C in mixtures of H_2O_2 in H_2O. As H_2O_2 can decompose exothermically to yield O_2, for comparison, suspensions with the same optical absorbance were made from SiC powder with an average particle diameter of 50 μm, as determined using an optical microscope.

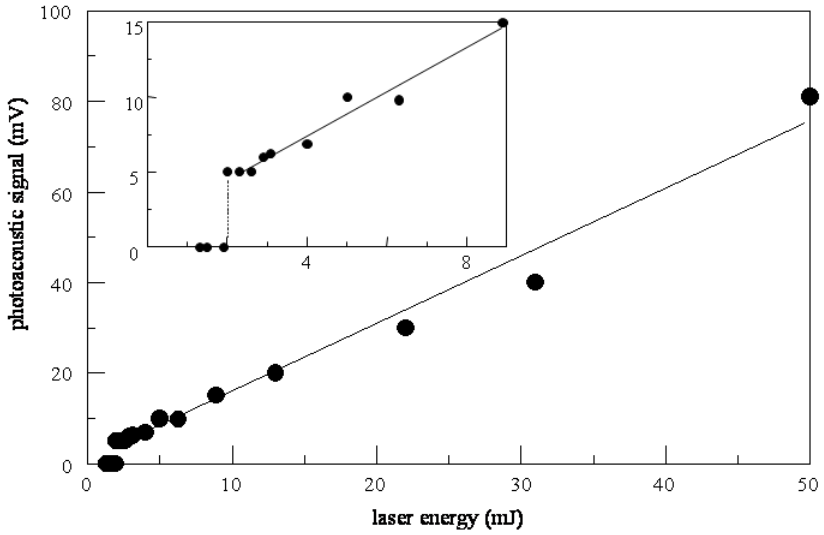

Figure 38: Photoacoustic signal amplitude versus laser energy for a 35% weight fraction of H_2O_2 in H_2O with a C concentration adjusted to give an absorbance of 0.25. The inset shows a portion of the same data on an expanded vertical scale. The wavelength of laser is 532 nm.

The Effect of Laser Energies on the Photoacoustic Signal Amplitude

Experiments were also done over a range of laser energies at 532 nm keeping the concentration of C and H_2O_2 in the mixture constant. At low laser fluencies, there is always a photoacoustic effect in aqueous suspensions of C in water, with the possible exception (91) of experiments (92) (93) done at 4 $^{\circ}$C, as there must be thermal expansion of the fluid as heat diffuses from optically heated particles. Figure 38 shows the photoacoustic signal amplitude versus laser energy. It can be seen that there is a distinct jump in signal amplitude, which can be ascribed to the elevation of the particles to a temperature sufficiently high to initiate a chemical reaction. The inset in Figure 38 shows the same data on an expanded scale. It is of note that experiments with C in H_2O show a similar jump in amplitude with increasing laser fluence indicating a threshold fluence for heating the particles to a temperature high enough for the reaction to proceed. Equation 20 shows a linear relationship between acoustic pressure and laser energy.

$$\frac{p_0}{E_0} = const\,\frac{\beta v_a}{C_p}\alpha \qquad (20)$$

where p_0 is the acoustic pressure amplitude developed, E_0 is the laser energy in a pulse or in a cycle, β is the thermal expansion coefficient, C_p is the specific heat at constant pressure, v_a is the acoustic velocity, and α is the optical absorption coefficient of the medium.

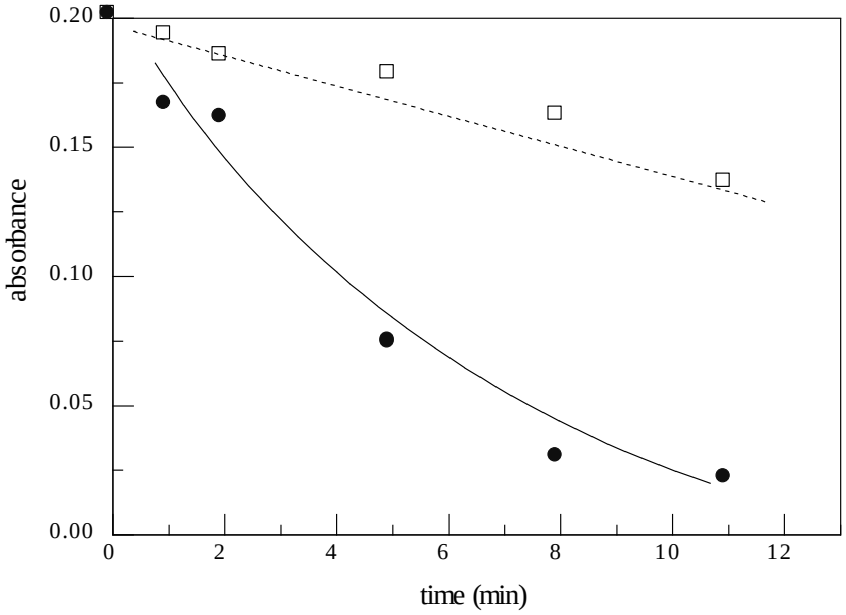

Figure 39: Optical absorbance versus time for (upper curve) a C in H_2O suspension, and (lower curve) C in a 50% by weight mixture of H_2O_2 in H_2O. The laser, which operated at 10 Hz, had a beam diameter of 1 cm and operated at 532 nm with pulse energy of 60 mJ. The cuvette in which the solutions were placed was continuously stirred. Absorbances were recorded at 700 nm with a conventional spectrophotometer.

Figure 40: Absorbance changing by laser irradiation (from left to right).

Diminution of the Absorbance

In addition to increasing the amplitude of the photoacoustic effect, the addition of H_2O_2 to aqueous C suspensions causes a more rapid diminution of the absorbance of the suspension on continued irradiation by the laser. Figure 39 shows the absorbance of two suspensions as a function of time as the laser was fired. The more rapid approach of the suspension containing H_2O_2 to optical transparency is another indicator of an enhanced reaction as a result of the addition of a strong oxidizer.

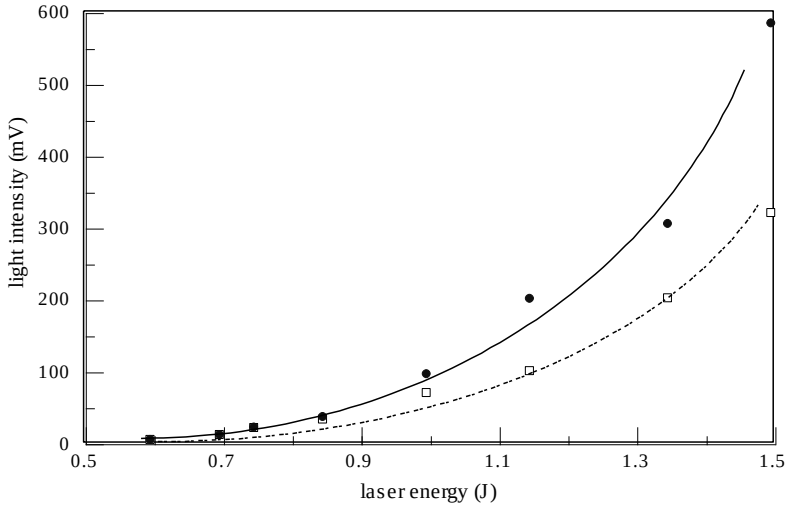

Figure 41: Photomultiplier signal versus laser energy in (upper curve) a mixture of 35% weight fraction of H_2O_2 in H_2O; and (lower curve) H_2O alone with the C concentration in both suspensions adjusted to give an absorption coefficient of 0.25 cm^{-1} at 532 nm. The laser wavelength was 1064 nm.

Light Emission

Colloidal suspensions of particulate carbon in water emit visible radiation when irradiated with high-power, pulsed laser radiation. It would be expected that the inclusion of H_2O_2 in the solution, which, depending on the reaction rate of H_2O_2 with C relative to that of H_2O with C, would lead to an increase in the temperature of the particles, enhancing the emission of radiation. Experiments to measure the optical emission of the suspensions coincident with the 1064 nm laser pulses were done using the same apparatus as described above, but with a photomultiplier (EMI, Inc., Model 9558B)

substituted for the acoustic transducer. That is, the photomultiplier, which was used without optical filters, viewed the cuvette at right angles to the direction of propagation of the laser beam. As only the intensity of the light flash on laser irradiation was of interest, the cable connecting the photomultiplier output to the oscilloscope was terminated with 1 MΩ, and signal amplitudes alone were recorded. The plot in Figure 41 shows the results of experiments with a suspension of C in an H_2O_2−H_2O mixture and a suspension of C in H_2O.

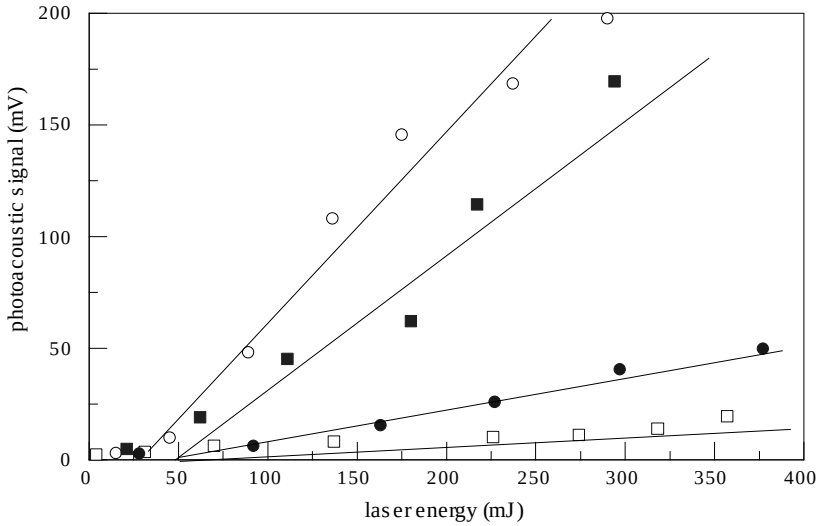

Figure 42: Photoacoustic signal amplitude versus laser energy for suspensions of $Hg(CNO)_2$ in water (○), C in CH_3NO_2 (■), C in 35 weight % H_2O_2 in H_2O (●) and C in H_2O (□). The laser beam diameter was 1 cm in diameter. The laser was operated at 532 nm.

Oxidizers and Explosives

Experiments were done with C suspensions in nitromethane and particulate suspensions of mercury fulminate in water. Carbon can undergo an exothermic reaction with CH_3NO_2, whereas $Hg(CNO)_2$ is expected to undergo explosive decomposition on irradiation with a high power laser irrespective of the presence of H_2O. $Hg(CNO)_2$ was prepared by dissolving Hg in HNO_3 and adding C_2H_5OH to the solution. Particles of $Hg(CNO)_2$ were maintained in suspension through use of a stirring bar placed at the bottom of the cuvette; as C forms stable suspensions in CH_3NO_2, continuous stirring was not necessary. The $Hg(CNO)_2$ particles were determined by optical microscopy to have

diameters on average of 100 μm. The results of the experiments with CH_3NO_2 and $Hg(CNO)_2$ are shown in Figure 42 along with data for suspensions of particulate C in H_2O_2 and in H_2O for reference.

3. 3 Discussion of Photoacoustic Effect

Chemically Generated Photoacoustic Model

A model to describe the photoacoustic effect that includes chemical reaction must include the consumption or liberation of thermal energy and volume changes produced on the conversion of reactants to products. In the case of the Carbon-Steam Reaction, the volume change is substantial because of the great disparity between the molar volume of gases such as H_2 and CO and liquid water. Consideration of the effects of energy consumption and volume change in the linearized hydrodynamic equations for a fluid (29) gives the acoustic density δ and temperature τ as solutions to the coupled equations

$$\left(\nabla^2 - \frac{\gamma}{c^2}\frac{\partial^2}{\partial t^2}\right)\delta = -\rho\beta\,\nabla^2\tau - \rho\beta_c\,\nabla^2 n \tag{21}$$

and

$$\lambda\,\nabla^2\tau - \rho C_v\frac{\partial\tau}{\partial t} = -H + \rho\mu^{\dagger}\frac{\partial n}{\partial t} - \frac{C_v(\gamma-1)}{\beta}\frac{\partial\delta}{\partial t} \tag{22}$$

where γ is the heat capacity ratio, c is the speed of sound, t is time, ρ is the ambient density, β is the thermal expansion coefficient, β_c is a "chemical" expansion coefficient, n is the differential concentration of new chemical species formed, λ is the thermal conductivity, C_v is the heat capacity at constant volume, H is the "heating function" (the energy per volume and time delivered to the fluid by the light beam), and $\mu^{\dagger}$ is a chemical potential. The chemical expansion coefficient is a measure of the change in fluid density

at constant pressure *P* and temperature *T* on the conversion of reactants into products, defined by

$$\beta_c = -\frac{1}{\rho}\left(\frac{\partial \rho}{\partial N}\right)_{P,T} \tag{23}$$

where *N* is the concentration of chemical species reacted. The chemical potential is the amount of internal energy per mass stored per concentration of chemical species reacted at constant density and temperature and is defined as

$$\mu^{\dagger} = \left(\frac{\partial \epsilon}{\partial N}\right)_{\rho,T} \tag{24}$$

where ε is the internal energy per mass of the fluid.

Equation 21 is essentially a wave equation for the acoustic density, and Equation 22 is a heat equation for the temperature change coupled through a compressive work term, the $\frac{\partial \delta}{\partial t}$ term in Equation 22. The two source terms on the right side of Equation 21 show that changes in either the temperature or the chemical composition act identically to launch acoustic waves. The term in Equation 22 containing the chemical potential acts as an energy source, or sink, that augments or diminishes *H*.

Exothermic Reaction

When the photoacoustic effect is generated by the simple absorption of radiation and the heating of a fluid, sound generation arises through volume expansion, which is essentially a mechanical motion, the effect of which is to launch a sound wave. When phase change

is the ultimate result of the absorption of laser energy the mechanism of sound production is different but still relies on volume change. Consider the relative volume changes for the two processes. If, for instance, 1 J of laser energy is absorbed in a 1 cm^3 of H_2O at room temperature, where its volume expansion coefficient is 2×10^{-4} K^{-1}, the change in temperature is 0.24 K and the relative volume change from thermal expansion, $\Delta v/v$ is 4.8 $\times10^{-5}$. The Carbon-Steam Reaction that is initiated by a laser in an aqueous colloidal C suspension and its enthalpy of reaction

$$C\ (s) + H_2O\ (l) \rightarrow CO\ (g) + H_2\ (g) \qquad \Delta H = 175\ kJ/mol \qquad (25)$$

(Note that the values of ΔH given here and below all refer to conditions at standard temperature and pressure and can be used only as a rough guide to the actual values at the temperatures of the heated particles.) If the same 1 J is used to consume C through the carbon steam reaction, then 1.14×10^{-5} moles of gas are generated, which, at room temperature and a pressure of 1atm, gives $\Delta v/v = 0.278$. Despite the consumption of laser energy in driving the Carbon-Steam Reaction, the ratio of the relative changes for the chemical reaction and thermal expansion mechanisms can be seen to differ by nearly a factor of 6000. As the mechanisms of the thermal expansion of water and the expansion of highly compressed gases involve complicated fluid dynamics, this figure cannot be taken to predict relative photoacoustic amplitudes in experiments. A remarkably large photoacoustic effect is generated by C suspensions in water.

In the case of the reaction with C and H_2O_2, two reactions are possible.

$$C\,(s) + H_2O_2\,(l) \rightarrow CO\,(g) + H_2O\,(g) \qquad \Delta H = -165\ \text{kJ/}mol \qquad (26)$$

and

$$C\,(s) + H_2O_2\,(l) \rightarrow CO_2\,(g) + H_2\,(g) \qquad \Delta H = -206\ \text{kJ/}mol \qquad (27)$$

In the first of these, the H_2O is formed initially as a gas. When H_2O (g) is condensed to H_2O (l), the heat of vaporization ΔH = 41 kJ/*mol* of water is released, adding to the generation of the photoacoustic effect through thermal expansion, but, at the same time, decreasing that from phase change, as only one mole of gas per mole of C remains. Since both reactions 26 and 27 are exothermic, it is possible, depending on the reaction rates, that the absorption of laser radiation is required only as a means of raising the temperature to initiate a reaction, and that the consumption of particles within the volume irradiated by the laser could proceed as a result of a chemical reaction alone. In contradistinction to reaction 25, there is a minimum energy required by the laser. However, there was no evidence for such a large effect from experimental observations; but, as shown in Figure 39, for a roughly 5 cm^3 of a continually stirred solution, there was a substantially more rapid consumption of the C in H_2O_2 solutions relative to that for C in H_2O suspensions.

Optical Radiation

The optical radiation emitted by a C suspension in H_2O irradiated by a 1064 nm laser radiation appears white to the naked eye. It is reasonable to assume that the emitted radiation arises from a mechanism whereby the rate of laser heating of the C particles

initially exceeds that of heat conduction, energy loss through light emission, and chemical reaction until the particles reach a temperature at which the energy deposition and loss mechanisms balance. The process is influenced, as well, by the time profile of the laser pulse. It would appear that the enhancement in the observed luminescence owing to the presence of H_2O_2 shown in Figure 41 is caused by the change in the character of the chemical reaction from one that consumes energy to one that releases energy, and results of an increase in the temperature of the C particles even though the reaction with H_2O_2 acts to consume the C faster, presumably making smaller particles or consuming them completely, relative to the reaction of C in H_2O.

Oxidizers and Explosives

Although CH_3NO_2 can explosively decompose by itself, the reaction of C(s) with CH_3NO_2 (l) most likely takes place through

$$C + 2\ CH_3NO_2 \rightarrow 3H_2\ (g) + 3\ CO\ (g) + H_2O\ (g) + N_2\ (g) \quad \Delta H = -347\ kJ/mol \qquad (28)$$

which is even more exothermic than the reactions of C with H_2O_2. According to Figure 42, the magnitude of the photoacoustic effect from particulate C is seen to be larger in CH_3NO_2 than it is in either H_2O_2 or in H_2O at any given laser fluence. This increase can be attributed to either the more negative reaction enthalpy, or the higher number of moles of gas produced in Reaction 28 per mole of C relative to that produced by the latter two oxidizers.

The photoacoustic effect recorded in suspensions of $Hg(CNO)_2$ in H_2O show the largest amplitude for any of the suspensions studied. The decomposition reaction for $Hg(CNO)_2$ can be expected to be

$$Hg(CNO)_2\ (s) \rightarrow Hg\ (g) + N_2\ (g) + 2\ CO\ (g) \qquad \Delta H = -423\ kJ/mol \qquad (29)$$

which has a reaction exothermicity greater than that of any of the other reactions studied here, and gives the largest photoacoustic effect. As $Hg(CNO)_2$ is an explosive and is known as having explosive velocity of 4250 m/s, it is expected that the mechanism of sound production involves the formation of spherical shock waves at the sites of each of the particles which then expand outwardly and coalesce into a macroscopic sound wave. A unique feature of the laser irradiation of $Hg(CNO)_2$ suspensions is that on a single firing of the laser, the absorption of the suspension is profoundly changed in the irradiated volume of the cuvette, decreasing sharply in amplitude and taking on broad absorption features.

One of the unexpected results of the experiments described here is that there appears to be no chemical reaction generated when suspensions of SiC in H_2O_2 are irradiated by the pulsed laser: no unusually large photoacoustic effect is generated, and there is no evidence of loss of absorbance by the suspension, or the evolution of gas after numerous firings of the laser. In fact, H_2O_2 decomposes rapidly in the presence of a catalyst to form O_2 through the reaction

$$H_2O_2\ (l) \rightarrow H_2O\ (g) + \frac{1}{2}O_2\ (g) \qquad \Delta H = -54\ kJ\ /\ mol \qquad (30)$$

The experiments indicate that the heated SiC particles do not undergo reaction by themselves with H_2O_2 or initiate decomposition of the peroxide.

Laser irradiation of aqueous suspensions of colloidal C is well-known to produce a large photoacoustic effect as a result of chemical reaction. The experiments reported here point out the profound effect that the addition of an oxidizer to a C suspension has on the amplitude of the photoacoustic effect. It may be possible to design particles that undergo exothermic chemical reactions on absorption of laser irradiation as contrast agents, such as colloidal Au are used as contrast agents for photoacoustic imaging.

A somewhat unexpected result of the experiments is that even though there is always consumption of C as the laser is fired, even in the case of relatively concentrated H_2O_2 or neat CH_3NO_2, a single laser shot does not result in complete reaction of the C in the irradiated portion of the cuvette. Why this is the case can depend on reaction kinetics, where the time for reaction is slow compared with the pulse length of the laser, or, perhaps, a shielding effect, where the reaction products prevent the oxidizer from contacting the interior of the particle as it undergoes reaction.

3. 4 Conclusion

Irradiation of chemically reactive particulate suspensions by high-power, pulsed Nd:YAG laser radiation initiates reactions at the sites of the particles so that besides the absorbed optical energy, chemical energy is liberated. In addition to the release of chemical energy, chemical reaction can result in gas production both of which result in enhancement in the amplitude of the photoacoustic effect. The inclusion of H_2O_2 in an aqueous C suspension changes the normally endothermic reaction of C with H_2O into the highly exothermic reaction of C with H_2O_2 leading to both an enhanced photoacoustic effect and an increase in light emission from the suspension. As well, laser-initiated exothermic reactions in suspensions of C with CH_3NO_2 and particulate $Hg(CNO)_2$ in H_2O are shown to result in greatly enhanced photoacoustic signal amplitudes.

Chapter 4 Generation of Sonoluminescence by Laser-induced Exothermic Chemical Reaction

4. 1 Chemical Generation of Sonoluminescence

Laser-induced Carbon-Steam Reaction

The chemical generation of sonoluminescence is based on laser-induced Carbon-Steam Reaction; a laser beam focused into an aqueous suspension of C generates highly compressed gases through the Carbon-Steam Reaction,

$$C\,(s) + H_2O\,(l) \rightarrow CO\,(g) + H_2\,(g) \qquad \Delta H = 175\ \text{kJ/}mol \qquad (31)$$

where ΔH is the reaction enthalpy at standard temperature and pressure. The multiple bubbles formed at the sites of the nanometer sized C particles coalesce into a single bubble, which expands beyond its equilibrium diameter, and then collapses to give a flash of light. Although the Carbon-Steam Reaction is endothermic so that it consumes laser

energy, the characteristics of chemically generated sonoluminescence are the high intensity of the sonoluminescence and the large size of the gas bubble.

Exothermic chemical reactions

Park *et al.* (39) reported that the magnitude of the photoacoustic effect in an aqueous C suspension can be greatly enhanced by adding H_2O_2 to the suspension so that sound is produced through the initiation of exothermic chemical reactions. The exothermic reaction of C with H_2O_2 proceeds through either of two reactions to generate sonoluminescence:

$$C(s) + H_2O_2\ (l) \rightarrow CO\ (g) + H_2O\ (g) \qquad \Delta H = -165\ kJ/mol \qquad (32)$$

$$C(s) + H_2O_2\ (l) \rightarrow CO_2\ (g) + H_2\ (g) \qquad \Delta H = -206\ kJ/mol. \qquad (33)$$

Both the intensity of the sonoluminescence resulting from exothermic chemical reaction and its time of appearance following irradiation by the laser are studied. In addition, the influence of pressure in the reaction chamber on sonoluminescence from laser irradiated aqueous suspensions of C is investigated.

4. 2 Experiments

Experimental Setup

To generate sonoluminescence, the 1064 nm output a Q-switched Nd:YAG laser with a pulse width of 10 ns and a repetition rate of 2 Hz was focused with a 10 cm focal length lens into a rectangular reaction chamber equipped with three 10 mm thick quartz windows with diameters of 50 mm. Experiments were done with 25 nm diameter C particles (Cabot, Inc., Black Pearls 470) in distilled H_2O or in mixtures of H_2O_2 with H_2O. Stock solutions of 50% H_2O_2 in H_2O (Aldrich Co., reagent grade) were used. The concentration of C in all of the solutions was 20 mg/l.

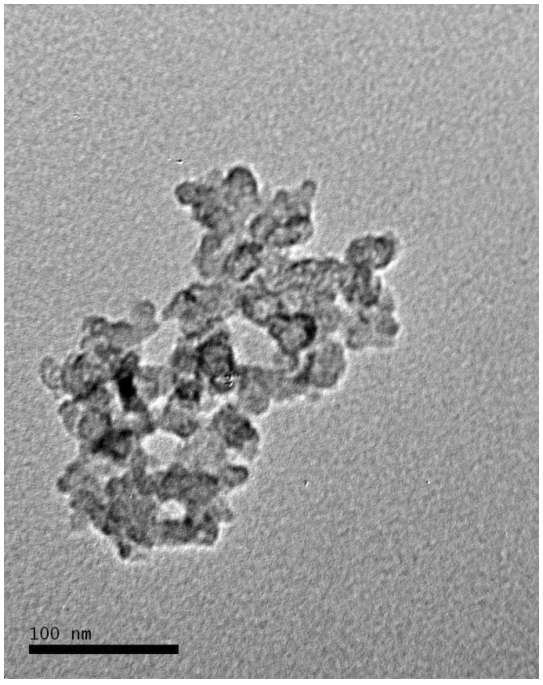

Figure 43: TEM image of 25 nm carbon suspension.

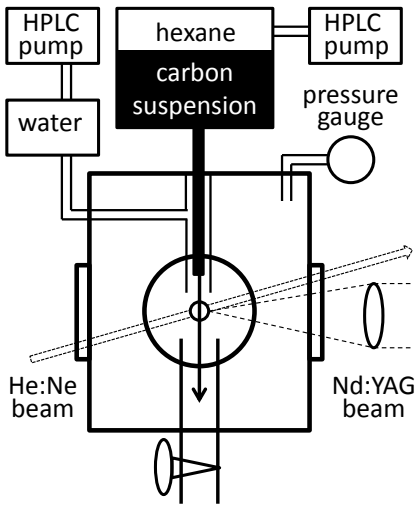

Figure 44: Schematic diagram of the experimental apparatus. The reaction vessel was equipped with three windows: the one on the right for the high power Nd:YAG laser beam, the one on the left for a He-Ne laser beam which passed through the left window and out the right window at an angle, and a third one for a bare photomultiplier to view sonoluminescence.

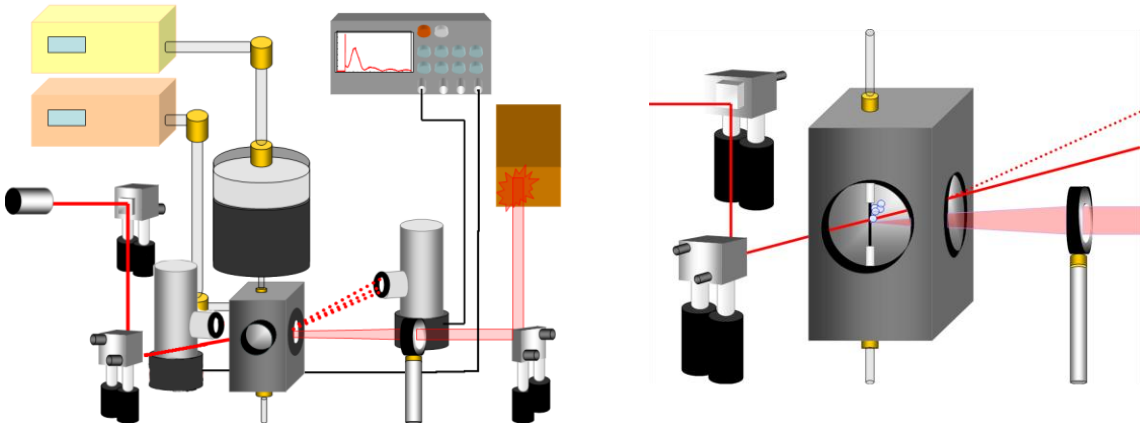

Figure 45: Schematic diagram of the experimental apparatus.

(a) (b)

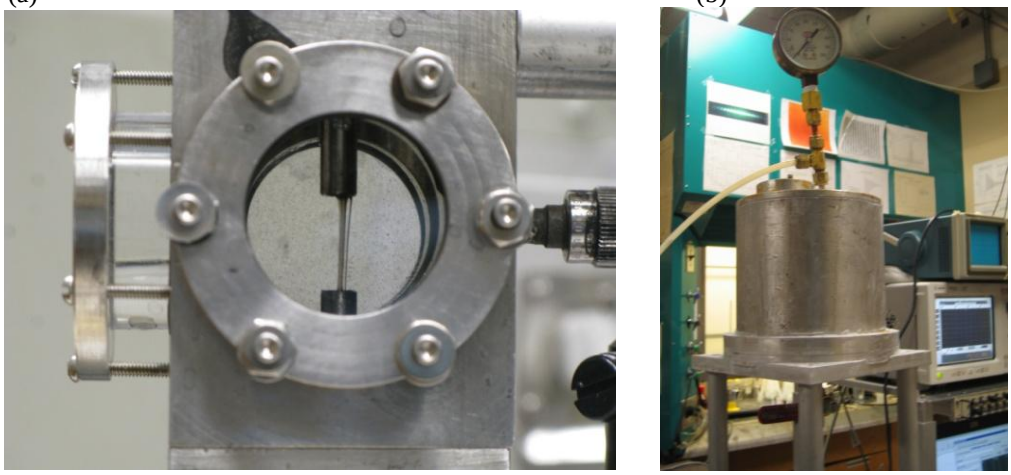

Figure 46: Experimental apparatus. (a) reaction chamber and (b) tank holding C suspension and hexane.

As shown in Figure 44, the chamber was fitted to hold chromatography tubing with an inside diameter of 0.5 mm which was placed inside a larger, second piece of tubing with a 10 mm inside diameter. In order to avoid sending the C suspension through a pump, an HPLC (high performance liquid chromatography) pump was used to deliver hexane, which has very low solubility in water (13 mg/L at 20 ºC) and floats on water, into a

sealed holding tank containing approximately 1 L of the C suspension as shown in Figure 46 (b). By connection tubing from the bottom of the holding tank to the chromatography tubing that led into the reaction chamber, the C suspension could be forced into the reaction chamber at high pressure to form a fine stream. At the same time, water was pumped by a second HPLC pump into the inside of the larger diameter tubing so that a sheath of water flowed around the colloidal C stream. The flow rates of the HPLC pumps were adjustable and could be varied continuously up to 10 mL/min. As the pumps operate up to limiting pressures of 75 atm, the pressure in the chamber could be varied by restricting the flow at the exit of the reaction vessel by adjusting the opening of a valve. This experimental arrangement provided for generating a fine stream of the C suspension that remained encased in a water sheath which extended throughout the length of the reaction chamber; as well, it permitted the flowing water to flush out continuously any suspension that ended up in the region traversed by the laser beam as a result of turbulence induced by the intense interaction of the focused laser beam with the C suspension.

The diameter of bubble as a function of time is an essential parameter in characterizing sonoluminescence. Light scattering was used to monitor the oscillations in the diameter of the bubble by directing a He-Ne laser beam into the reaction chamber at the point where the Nd:YAG laser beam was focused. A photomultiplier equipped with an interference filter to pass 632.8 nm radiations viewed the laser interaction region. An additional photomultiplier was placed at perpendicular incidence to the direction of propagation of the Nd:YAG laser beam to view sonoluminescence from the bubble. The photomultiplier for recording sonoluminescence was a 50 mm diameter head-on tube

with sensitivity in the spectral region from 300 to 900 nm. Appendix B includes key specification of photomultipliers. Signals were recorded on a digital oscilloscope (Agilent Inc., Infinium 54845A) that had a bandwidth of 1.5 GHz and a sampling rate of 8 GSa/s. Signals from the photomultiplier were terminated in 1 MΩ to broaden the pulse to permit more facile recording; those from the photomultiplier viewing 632.8 nm were terminated in the impedance of the cable, 50 Ω.

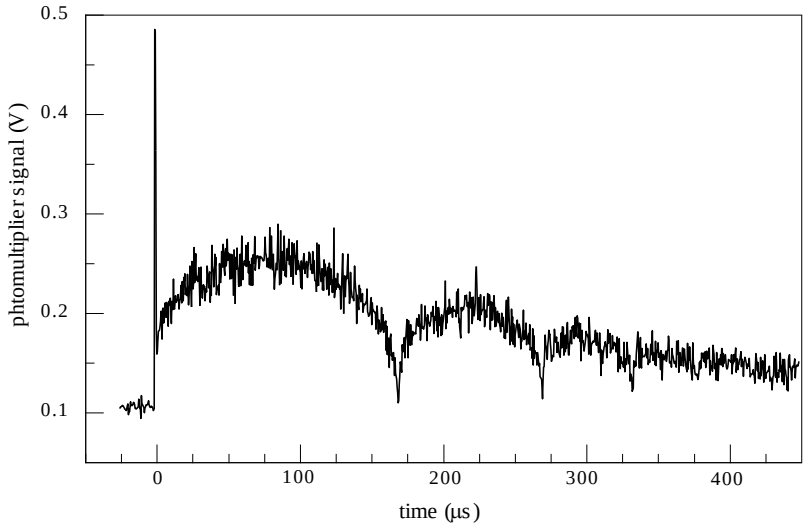

Figure 47: Signal amplitude versus time for a photomultiplier viewing 632.8 nm radiation from a C suspension that was 50 % by weight H_2O_2 and H_2O irradiated by a Nd:YAG laser pulse with an energy of 500 mJ. The initial spike of light in the oscilloscope is broadband radiation that extends throughout the visible spectral region arising from the interaction of the laser with C in the suspension.

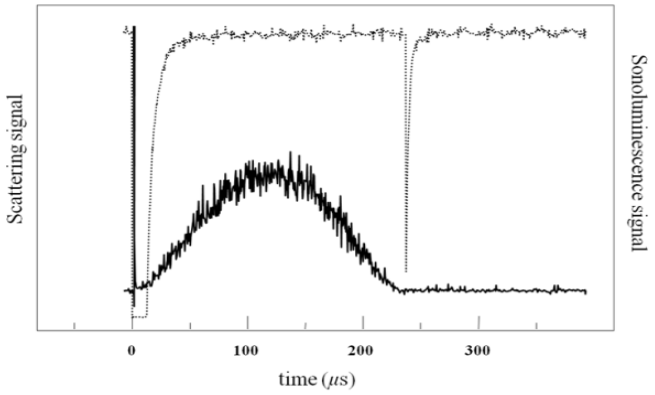

Figure 48: Photomultiplier output voltage in arbitrary units vs. time for: top trace, a photomultiplier viewing the irradiated suspension, and bottom trace a photomultiplier with 632 nm filter recording the intensity of He-Ne laser light scattered from a bubble generated in a 20 mg/l aqueous carbon suspension by a laser with a power of 500 mJ.

Light scattering

The results of a light scattering experiment are shown in Figure 47. Laser heating of the C in the suspension causes generation of an intense flash of light, some of which is within the pass band of the interference filter, giving the initial spike seen in the photomultiplier signal. The remaining part of the waveform following the spike arises from scattering by the bubble. The scattering signal shows bubble oscillations with periods markedly larger than those found with bubbles in acoustic traps used to produce sonoluminescence which is less than 50 μs. Comparison of the baseline before the firing of the laser with that after the oscillations have decayed shows that a bubble of permanent gas is formed by the laser-initiated chemical reactions. At higher laser fluences typically a single oscillation of the bubble is seen with a sonoluminescent flash occurring at the point of collapse of the

bubble, which is shown in Figure 48. The threshold laser fluencies acquired to initiate sonoluminescence has not been studied.

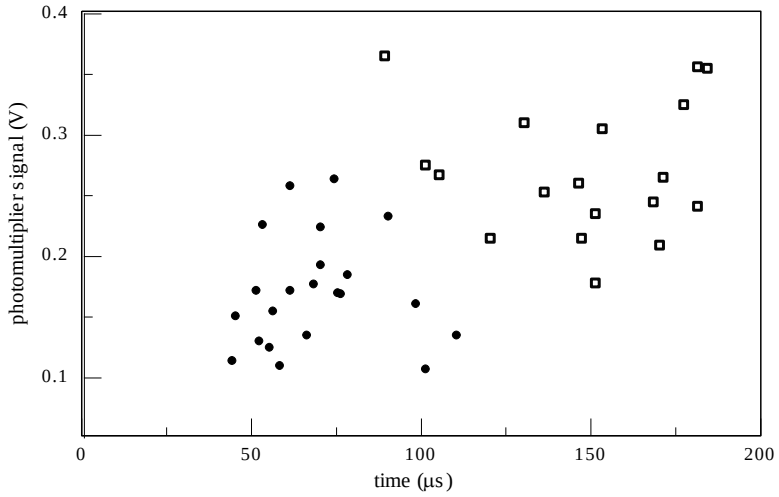

Figure 49: Sonoluminescent intensity recorded by the photomultiplier versus time of appearance of sonoluminescence for (●) C suspensions in H_2O and (□) C suspensions in a 50% by weight mixture of H_2O_2 with H_2O irradiated by a Nd:YAG laser pulse with an energy of 500 mJ.

Sonoluminescent Intensity and the Appearance Time of Sonoluminescence

Experiments were also carried out to determine the intensity of sonoluminescence as a function of its the time of appearance after firing of the laser for aqueous C suspensions and C suspensions made in mixtures of H_2O_2 with H_2O with the laser energy maintained constant at 500 mJ per pulse. Figure 49 shows, for either suspension, an increase in sonoluminescent intensity with an increase in the time of appearance of sonoluminescence after firing of the laser. The effects of chemical reaction of C with H_2O_2 are seen to be both an increase in sonoluminescent intensity and an increase in the appearance time of sonoluminescence after the firing of the laser relative to what is found for sonoluminescence from aqueous C suspensions.

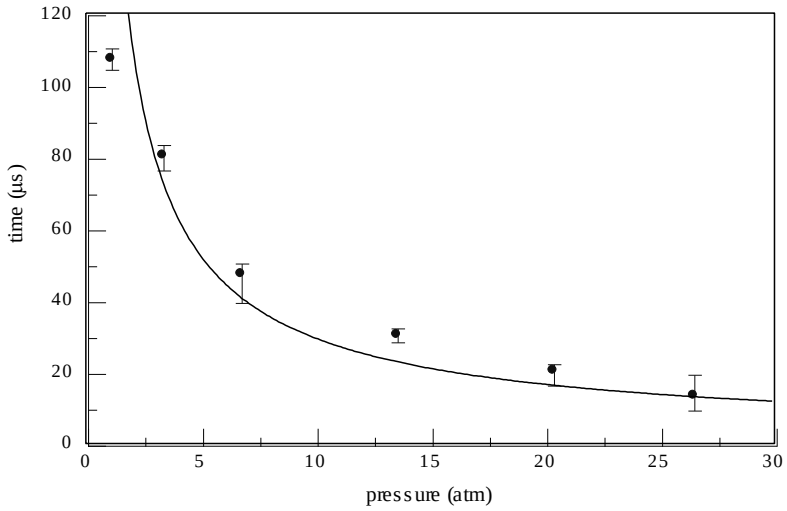

Figure 50: Time of observation of sonoluminescence after the firing of the laser versus pressure in the reaction vessel for an aqueous C suspension. Each point is the average of 8 recordings; the error bars represent the standard deviations in the measurements. The curve is a one parameter fit to the expression for t_s given by Equation 36.

Time and Intensity of Sonoluminescence versus Pressure

The effects of pressure on sonoluminescence in laser irradiated colloidal C suspensions can be easily studied by simply restricting the flow of fluid at the bottom of the reaction vessel to create high pressures. Figure 50 shows the time following firing of the laser at which sonoluminescence takes place as a function of the ambient pressure in the reaction vessel. The change in the appearance time for sonoluminescence as the pressure is increased from 1 to 27 atm is seen to decrease by approximately a factor of 10. The intensity of sonoluminescence over the same pressure range, as shown in Figure 51, increases by a factor of 5. The pressure-changing range was limited by the sealing of the reaction chamber and the strength of optical windows.

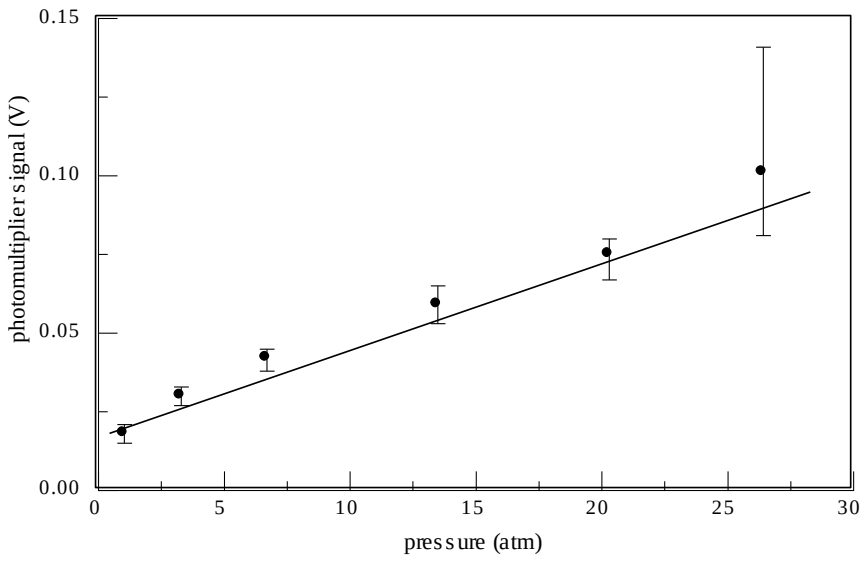

Figure 51: Sonoluminescence intensity recorded by the photomultiplier versus pressure for a carbon suspension in water. Each point is the average of 8 recordings; the error bars represent the standard deviations in the measurements. The line is a least square fit to the data with the assumption of a linear dependence.

Thermal Radiation and Heat Conduction

An additional experiment was done using a photomultiplier whose output was fed to the oscilloscope with the cable terminated in 50 Ω to view the initial flash of radiation coincident with firing of the laser. The suspension was an aqueous C suspension as described above. Although the photomultiplier had a time resolution of 10 ns, there was no evidence for generation of visible radiation that extended far beyond the pulse length of the incident laser beam. This result points to the strong effects of thermal radiation and heat conduction in reducing the temperature of the particles to a point where they do not emit in the visible spectral region following cessation of laser heating.

4. 3 Discussion

Sonoluminescence generated by laser-induced chemical reaction has 3 steps: absorption, expansion, and collapse. At first, the absorption of laser radiation initiates chemical reaction resulting in bubble formation. Secondly, individual bubbles at the sites of C nanoparticles agglomerate to become a single, highly compressed, expanding bubble of gas. At last, the bubble collapses to produce a sonoluminescent flash. At this point, much of its internal energy is lost to producing a flash of light and a burst of ultrasound. In the first step, when the laser is heating the particles, the absorbed laser energy is apportioned between chemical reaction, vapor production, emission of radiation, and the launching of acoustic burst. Following agglomeration of the individual bubbles a single bubble appears that must have some internal energy, *E*. A primitive approximation from ref. (77) can be made that for a fixed concentration of C in solution and a given laser energy, *E* should be a constant independent of the ambient pressure. The energy of a bubble undergoing oscillations is related to its potential energy *E*.

$$\mathrm{E} = \frac{4}{3}\pi\, R_{\mathrm{m}}{}^{3} P_0 \tag{34}$$

where R_{m} is the maximum radius of the bubble, and P_0 is the ambient pressure. If the time for collapse of a bubble t_{s} is taken as the inverse of the Minnaert frequency then

$$t_{\mathrm{s}} = 2\,\pi\, R_{\mathrm{m}} \left(\frac{\rho}{3\gamma P_0}\right)^{\frac{1}{2}} \tag{35}$$

where γ is the heat capacity ratio, and ρ is the fluid density. Combination of Equation 34 with Equation 35 gives the time of sonoluminescence following firing of the laser as

$$t_s = 2\ \pi^{\frac{4}{3}}\ \left(\frac{3E}{4}\right)^{\frac{1}{3}} \left(\frac{\rho}{3\gamma}\right)^{\frac{1}{2}} {P_0}^{-\frac{5}{6}} \tag{36}$$

The curve shown in Figure 50 is a fit to the ${P_0}^{-\frac{5}{6}}$ dependence given in Equation 36 showing at least qualitative agreement with the time of appearance data. The increase in sonoluminescent intensity of the collapsing bubble with ambient pressure shown in Figure 51 for a carbon suspension can arise from several factors such as lower viscous losses associated with smaller bubble diameter excursions at high pressure, a different admixture of vapor in the bubble, or a different radius when the sonoluminescence takes place. Further investigation of the pressure dependence of sonoluminescence is perhaps warranted.

4. 4 Conclusion

The finding that the optical radiation emitted by aqueous carbon suspensions is coincident with the laser pulse is expected for the endothermic Carbon-Steam Reaction—the reaction proceeds only when the laser supplies energy to the particles. In the case where exothermic reaction takes place, it is possible however that the laser can act to initiate the reaction, and that the reaction could proceed as a result of liberation of chemical energy, the reaction going to completion as individual nanoparticles within the laser beam are consumed. For the reaction of C with H_2O_2 at the concentrations employed here, this does not appear to be the case, as on the firing of a single laser pulse into a cuvette with such a mixture, significant optical absorption remains in the irradiated volume. Nevertheless, as shown here for the case of C suspensions, the substitution of an exothermic reaction for an endothermic reaction leads to a significant increase in both the brightness of sonoluminescence and the bubble diameter for a fixed amount of absorbed laser energy. It is likely that other laser initiated chemical reactions where the exothermicity of the reaction exceeds that of the reaction of C with H_2O_2 should produce sonoluminescence with even higher brightness.

Chapter 5 Comparison of Ultrasonic Distillation to Sparging of Liquid Mixtures

5. 1 Introduction

Distillation is a physical method of separating mixtures based on differences in their volatilities: its application in industrial processes are numerous and include the separation of crude oil into more fractions, the manufacture and purification of numerous liquid chemicals such as solvents, and for the production of a number of alcoholic beverages. Since separation of ethanol from water is an essential and energy consuming step in the conversion of fermented biomass to purified alcohol, efficient separation methods are of key importance in determining the economic feasibility of substitution of alcohol for petrofuels.

In 2001, “ultrasonic distillation” has been reported as a new method for separation of ethanol from water. In this method, vapor and mist are formed from liquid mixtures

irradiated by high intensity ultrasound which is removed by an air stream. (94) (95) When intense acoustic radiation produced by a transducer at the bottom of a fluid filled vessel is directed upward toward the surface of the liquid, the radiation force produces an upward displacement of the fluid surface at the center of the acoustic beam whose properties are described by nonlinear acoustics. (96) As the radiation intensity is increased, a jet of fluid is formed, and at somewhat higher intensities, mist is produced in the region of the displaced fluid. A fluid jet produced in this way is referred to an "ultrasonic fountain" in the acoustics literature.

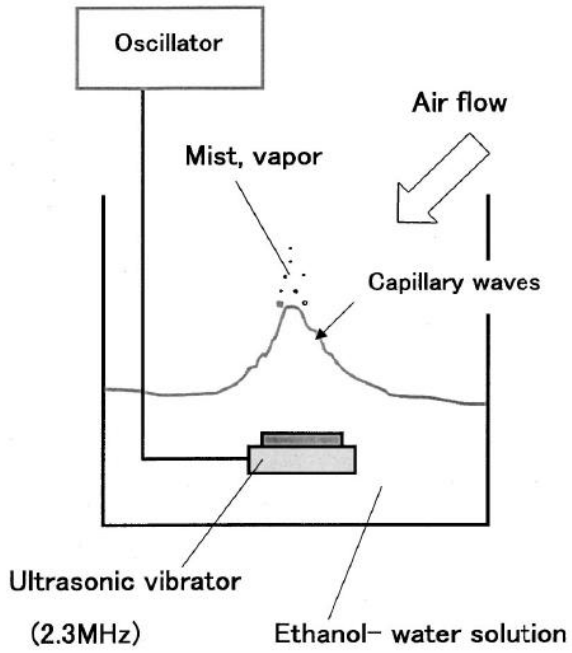

Figure 52: Experimental setup of ultrasonic separation of ethanol from ethanol-water solutions. The ultrasonic vibrator is comprised of 20 mm diameter piezoceramics, and has a resonant frequency of 2.3 MHz from ref. **(94)**.

As the experiments reported in ref. (94) indicate virtually complete separation of ethanol and water at 10 °C from liquid mixtures with ethanol-water mixtures at mole fractions as low as 15% and an energy efficiency where the input energy to the piezoelectric

transducer is smaller than the latent heat of vaporization of the liquid mixture, it is of some interest to explore ultrasonic distillation in general. Flame ionization gas chromatography, nuclear magnetic resonance spectroscopy, refractive index measurements, and spectrophotometry are used here to determine the efficacy of ultrasonic distillation relative to sparging with dry nitrogen. Experiments with an ethanol-water mixture, a mixture of two nonpolar solvents, a salt solution, and two colloidal suspensions are reported.

5. 2 Experiment

As shown in Figure 53, the apparatus used for studying ultrasonic distillation consisted of a 41 mm diameter glass tube connected to a short section of copper tubing approximately 2 cm high with a glass-to-metal Housekeeper seal. A few turns of copper tubing were soldered to the copper section of the tube through which a cooling solution from a feedback-controlled temperature controller (Thermo Tek, Inc., model T25IP) flowed. The glass part of the tube, which had an overall height of 25 cm, was fabricated to have a port for sampling the liquid near the bottom of the tube, an inlet port for the nitrogen, and a third port at the top of the apparatus for exhausting the mist, vapor, and nitrogen into a fume hood. The flow rate of N_2 through the vessel was 2000 cm^3/min. The mist formed by transducer on as shown in Figure 55 (c) was exhausted with flowing N2 as shown in Figure 55 (b). Commercial 25 mm diameter ceramic piezoelectric transducer assemblies (APC International, model 50-1011), used as components of a household ultrasonic humidifier, were attached to the bottom of the copper section of the vessel by an O-ring to provide either 1.64 or 2.40 MHz ultrasound. The maximum power consumption of the oscillator circuit producing the ultrasound was 29 W. The intensity of the ultrasound was adjusted by a variable voltage supplier to a level sufficient only to cause upward displacement of the fluid in the center of vessel on the order of 5 cm.

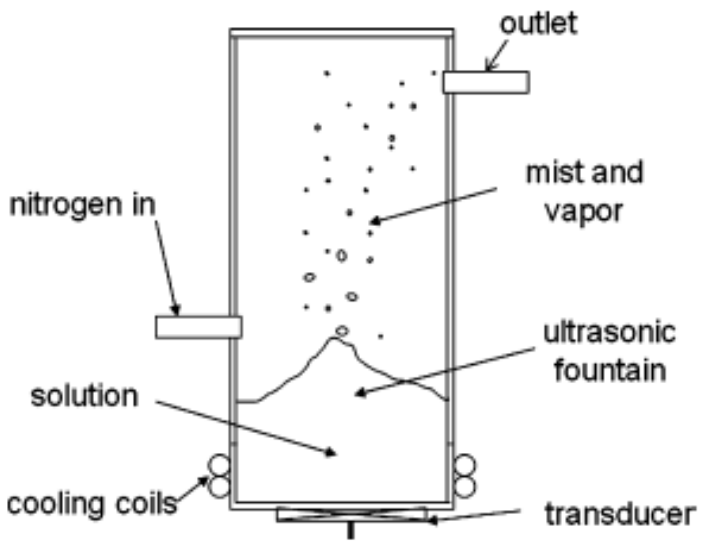

Figure 53: Schematic of the apparatus used for ultrasonic distillation. Dry nitrogen purge gas flows into the region above the ultrasonic fountain, carrying out both the mist and vapor. Experiments used on the order of 50 mL of the solvent mixtures.

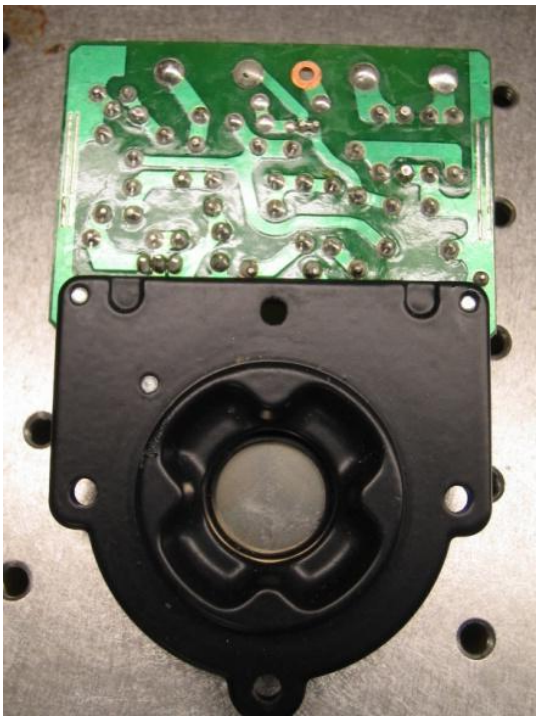

Figure 54: Commercial 25 mm diameter ceramic piezoelectric transducer assemblies (APC International, model 50-1011).

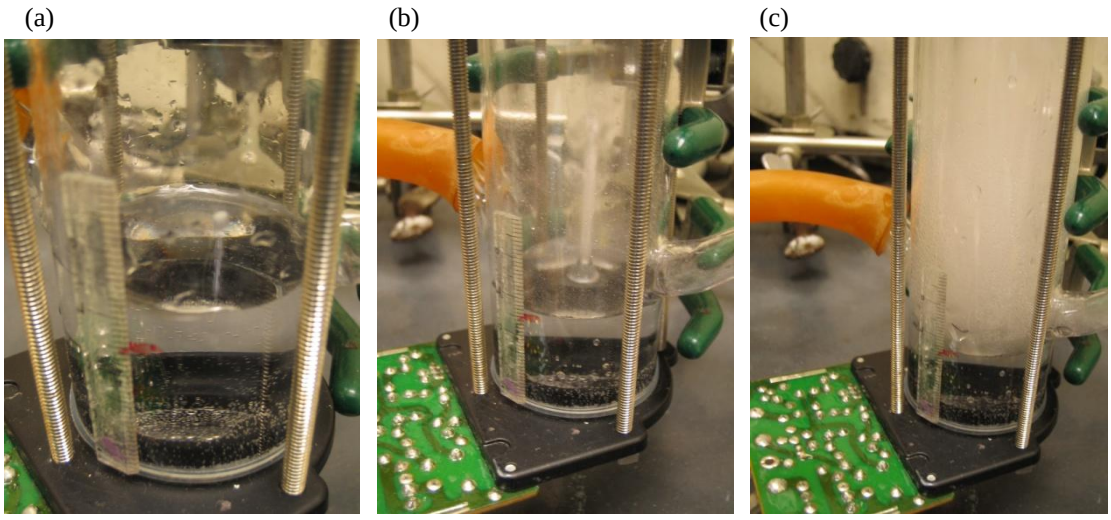

Figure 55: Ultrasonic fountain formation. (a) transducer off, (b) transducer on with flowing N_2, and (c) transducer on without flowing N_2.

Sparging experiments were carried out by flowing a stream of high-purity nitrogen through a piece of tubing that extended to the bottom of a glass graduated cylinder or the ultrasonic distillation vessel with the same flow rate as above but without the application of ultrasound. The flow rate of the nitrogen was kept sufficiently low to prevent violent bubbling and loss of liquid.

Figure 56: Experimental setup for Sparging. A flowmeter is shown as well.

Refractive index measurements were carried out by taking liquid samples of a few microliters from the distillation vessel or the graduated cylinder using a pipet and transferring them to an Abbe refractometer (Fischer Scientific, model 13-964). The refractometer was calibrated to determine the refractive index versus ethanol volume fraction in 10 ethanol-water mixtures over the range from 0.05 to 0.95. The accuracy of the measurements was determined to have a standard deviation of ±0.0001 in the index of refraction. Nuclear Magnetic Resonance determinations (NMR) of mole fractions were made by filling NMR sample tubes with 25 μL of the solvent mixture after sparging and ultrasonic distillation, together with 600 μL of 99.9 atom percent D6-acetone (Sigma Aldrich, 444863) using a 300 MHz NMR spectrometer (Bruker, Inc., model DPX Advance). In the experiments with organic solvents, determination of the mass fractions was done using a capillary gas chromatograph (Varian, model CP3900 with a FactorFour VX-1 ms column) with flame ionization detection. A conventional spectrophotometer (Varian Cary, model 50) was used for experiments with ionic and colloidal solutions.

Figure 57: Gas chromatograph (Varian, model CP3900)

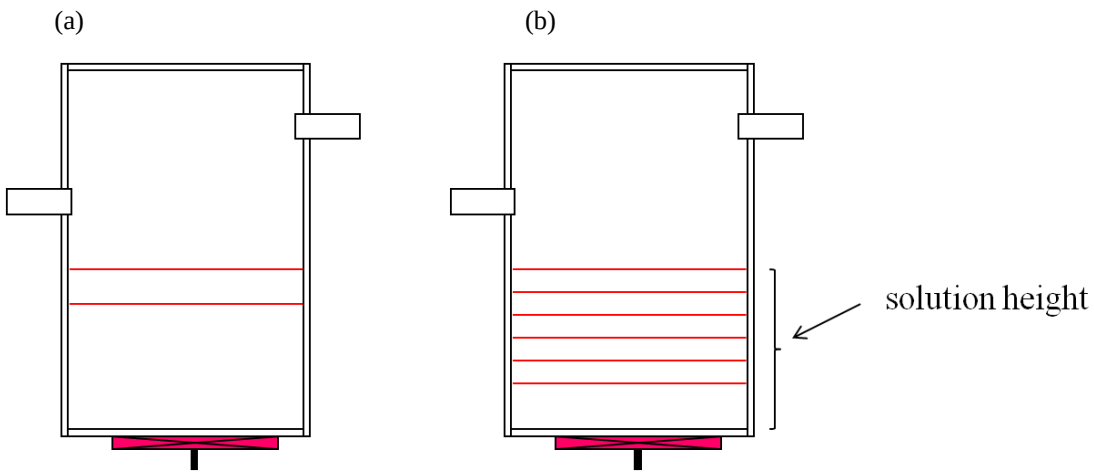

Figure 58: Schematic of the experimental methods. (a) method #1: multiple solutions with single measurement and (b) method #2: single solution with multiple recordings.

Experiments with ethanol-water mixtures were made by mixing 99.8% ethanol (Sigma Aldrich, spectrophotometric grade) with distilled water. Two different methods were used here, as shown in Figure 58. In the first method, sparging and ultrasonic distillation were carried out on identical volumes of solvent mixtures until a given percentage of the volume was lost through either process, at which point, measurements of the relative concentrations of the components remaining in the vessel were made. In total, 10 different solvent mixtures were made with ethanol volume fractions ranging from 0.05 to 0.95. Equal amounts of a single mixture were then placed in the ultrasonic distillation apparatus and a 41 mm diameter graduated cylinder for sparging with nitrogen. Sparging and ultrasonic distillation of the mixture were carried out at 20 °C until a 25% decrease in volume was recorded, at which point sparging or distillation were stopped and 10 μL samples of the remaining solvent mixtures were taken to determine the relative volume fractions in the remaining sample with the refractometer. The refractometer was calibrated using samples from the original 10 mixtures. Each of the 10 mixtures was

tested using this procedure producing the data shown in Figure 59 for ultrasonic distillation and sparging of the 10 mixtures, together with a calibration curve for the refractometer. A vertical line at any of the data points in Figure 59 gives the volume fraction for the original solvent mixture on the abscissa and on the ordinate the index of refraction of the mixture following ultrasonic distillation or sparging. The volume fraction after distillation is found by reading the index of refraction of the final solution and using the calibration curve to determine the volume fraction of ethanol in the remaining mixture. It can be seen that the volume fraction of ethanol in the sparged samples in the liquid was consistently less than that of the ultrasonically distilled samples. On the basis of this observation, it is concluded that sparging produced a higher volume fraction of ethanol (the more volatile of the two solvents) above the fluid than did ultrasonic distillation.

Additional experiments were performed using a second experimental procedure where mixtures with known volume fractions were separately placed in the distillation vessels, and, as the separation proceeded, samples were taken for analysis at different heights of the fluid in the vessel until the height of the solution decreased to 1/2 of its original value. Two experiments at 10 °C with ethanol volume fractions of 0.5 and 0.95 (near the azeotrope for ethanol-water) were done with the view of replicating some of the same conditions reported in ref. (94). A series of approximately seven samples was taken for analysis as the distillation proceeded, using the refractometer as a diagnostic. The data shown in the inset of Figure 59 indicate no separation of components of ethanol-water near the azeotrope to within the error of measurement of the method. Note that although the measurements with the refractometer are not as accurate near the azeotropic

composition as they are for lower ethanol concentrations, the data at the left of the plot in the inset represent the results of integration of any separation as the mixture decreases to one-half of its initial volume. If there were substantial separation of components by either sparging or ultrasonic distillation, a downward trend in the data as the solution height approaches 18 mm would have been found. The other data showed in the inset for the 0.5 volume fraction ethanol in water at 11 °C shows nearly identical separations for sparging and ultrasonic distillation.

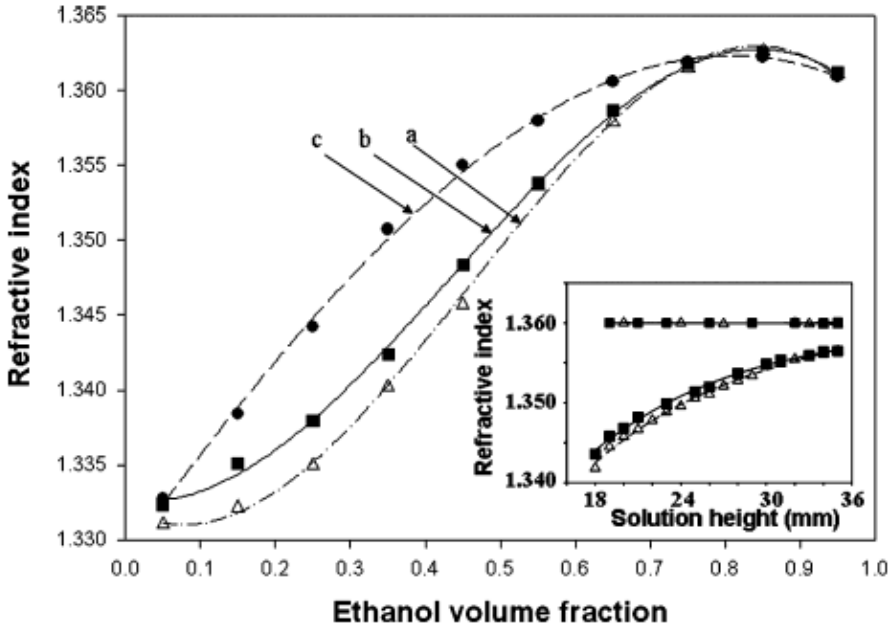

Figure 59: Index of refraction versus ethanol volume fraction for ethanol-water mixtures after (a) sparging; and (b) ultrasonic distillation at 2.4 MHz for 10 different mixtures. Curve c is the calibration curve for the refractometer. All data were taken at a temperature of 22 °C. Inset: index of refraction for two water-ethanol mixtures at 11 °C versus column height in the distillation vessel. The top curves are the results of ultrasonic distillation (■) and sparging (Δ) of an ethanol-water mixture at the azeotrope. The bottom curves are the results of ultrasonic distillation (■) and sparging (Δ) of a 0.5 volume fraction composition of ethanol in a water-ethanol mixture.

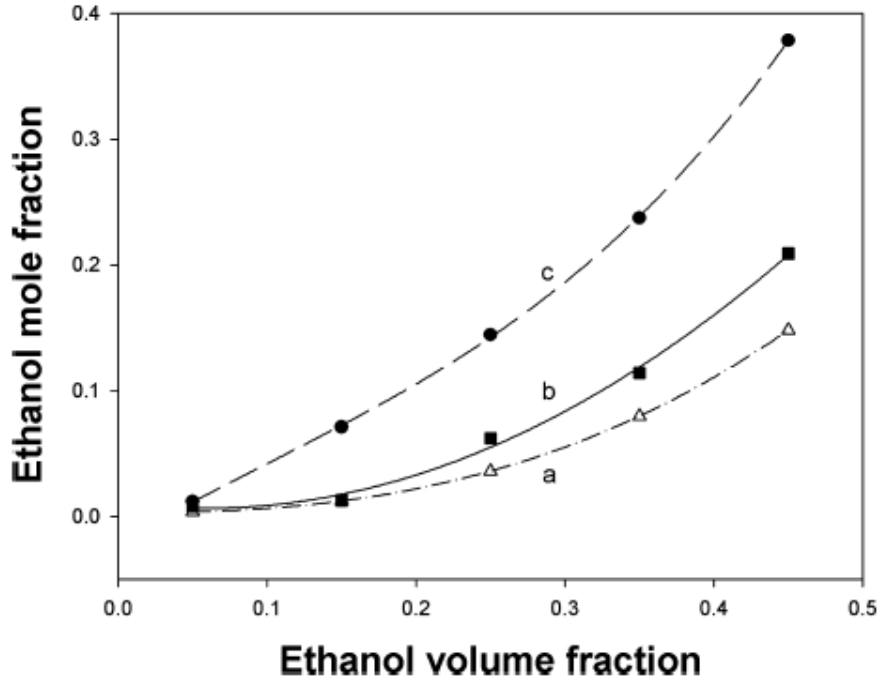

Figure 60: Ethanol mole fraction determined from NMR measurements for ethanol-water mixtures for (a) sparging and (b) ultrasonic distillation at 1.65 MHz and 22 °C. Curve c is a calibration curve.

NMR measurements were used for analyzing 5 different solvent as the diagnostic for determining mole fractions of ethanol in water by comparing the integrated areas of the H resonance peaks from water at 3.09 ppm to those for ethanol at 1.11 ppm. The first experimental method for distillation as described above was used. As shown in Figure 60, sparging again produced a lower mole fraction of ethanol in the remaining solution relative to ultrasonic distillation. At larger ethanol volume fractions than those plotted in Figure 60, the differences between the final ethanol volume fractions for sparging and ultrasonic distillation narrowed. However, sparging showed a more complete separation of the two components of the mixture than ultrasonic distillation.

Experiments with ethyl acetate-ethanol mixtures were carried out at 22 °C using the second procedure with three ethanol-ethyl acetate solutions, one with an ethyl acetate volume fraction above the azeotrope and two below the azeotrope. (97) Data for the mass fractions of ethyl acetate in the remaining mixture as a function of liquid in the distillation vessels are presented in Figure 61. The top two curves shown in Figure 61 show that for the ethyl acetate mixture above the azeotrope, the vapor is more enriched with ethanol in the vapor for sparging as compared with ultrasonic distillation. The bottom curves show that for ethyl acetate concentrations below the azeotrope, sparging yields vapor more highly enriched in ethyl acetate than ultrasonic distillation. The effects of sparging and ultrasonic distillation are thus qualitatively similar insofar as which component is enriched in the vapor.

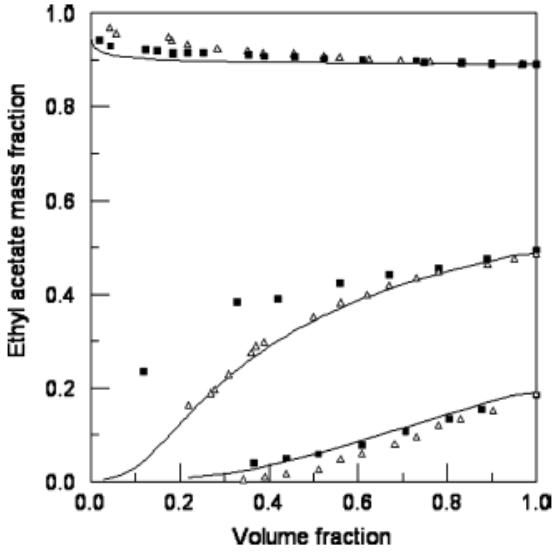

Figure 61: Mass fraction after sparging (Δ) and ultrasonic distillation (■) for three different ethyl acetate-ethanol mixtures at 22 °C. The top two curves are at ethyl acetate concentrations above the azeotrope; the remaining four curves are for ethyl acetate concentrations below the azeotrope. Time proceeds from right to left as the height of the mixture in the vessel decreases. The solid curves are calculated from the Rayleigh equation. The closeness of the ultrasonic distillation curve to the Rayleigh curve suggests a strong component of conventional distillation.

Experiments were done with aqueous solutions of $CoCl_2$ using the first method. Five 40 mL solutions were made using deionized water over a concentration range from 0.030 to 0.42 M. The absorbances of the solutions before and after sparging and ultrasonic distillation at 1.65 MHz were recorded using a spectrophotometer at a wavelength of 510 nm. Absorbance data were taken only for the initial solutions and for the solutions when their volumes had been reduced to 30 mL. The results of a few of the experiments, as given in Table 2, show that a substantial increase in the analyte concentration in the remaining solution could be found for sparging, whereas a smaller effect was found for ultrasonic distillation.

Table 2: Results of Absorption Measurements for Ultrasonic Distillation and Sparging of Five Aqueous Cobalt Chloride Solutions.

Concentration (M)	Original solution (cm^{-1})	Ultrasound (cm^{-1})	Sparging (cm^{-1})
0.0301	0.227	0.234	0.257
0.0904	0.427	0.437	0.522
0.181	0.734	0.760	0.937
0.301	1.133	1.161	1.467
0.422	1.534	1.637	2.027

Experiments with suspensions of 40-50 nm diameter colloidal silica in water (Nissan Chemical Co., Snowtex- 20 L) were carried out using the first method with the 2.4 MHz transducer where an initial solution volume of approximately 40 mL was ultrasonically distilled or sparged to 1/2 of its volume. Concentrations of the silica particles in solution were determined using the spectrophotometer at a wavelength of 520 nm, at which wavelength attenuation of the light beam in the spectrophotometer was predominantly from scattering. The results for two solutions with mass fractions of 0.42 and 0.83 silica are shown in Table 3. Identical experiments were performed with two solutions of 70-120 nm diameter colloidal gold in water (Purest Colloid, Inc.), the first with 20 mg/L and the second with 10 mg/L, where the intensity of absorption of the plasmon resonance at 520 nm was measured. As can be seen in Table 3, for both the colloidal gold and silica suspensions, sparging provides a more complete separation of the water from the suspension than ultrasonic distillation does.

Table 3: Results of Absorption Measurements for Ultrasonic Distillation and Sparging of Colloidal Gold and Silica Solutions.

solution	original (cm^{-1})	ultrasound (cm^{-1})	sparging (cm^{-1})
gold	0.162	0.254	0.303
gold	0.317	0.383	0.531
silica	0.186	0.233	0.330
silica	0.276	0.339	0.559

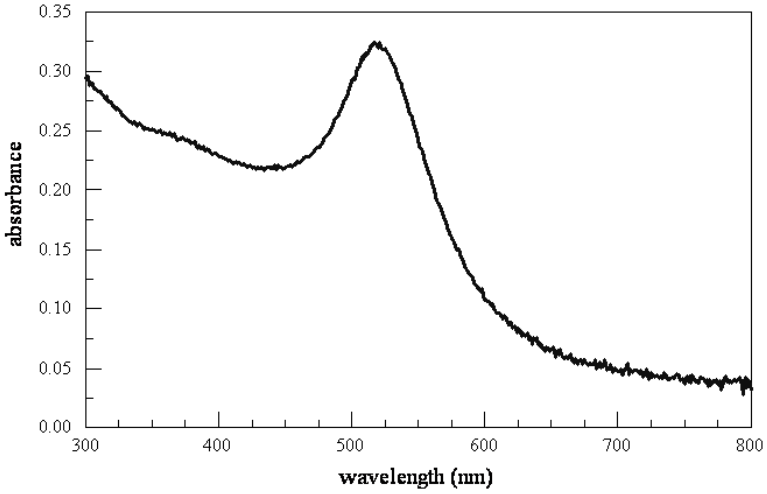

Figure 62: Absorbance spectra of colloidal gold showing a plasmon resonance at 520 nm.

5. 3 Discussion

Two widely accepted mechanisms for fog generation by intense ultrasound explain the ultrasonic fountain. As shown in Figure 63, the first posits that capillary waves (98) are produced by the high-intensity ultrasound at the surface of the liquid and that small droplets are ejected at the peaks in the capillary waves, resulting in the formation of a mist. (94) (99) The second mechanism, based on the formation of cavitation bubbles (100) within the liquid, posits that as vapor bubbles from cavitation reach the surface of the liquid, small droplets are ejected as a consequence of the force of hydraulic shocks that follow collapse of the bubbles. (101) (102) Experimental evidence can be found to support both theories. (103)

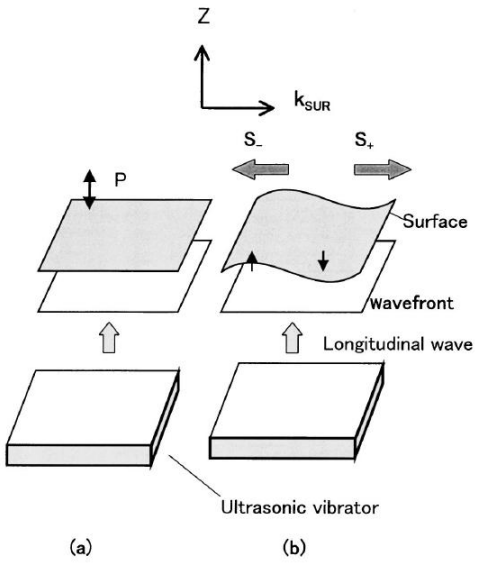

Figure 63: Mechanism of capillary waves formation. (a) Shows surface motion in phase that is driven by longitudinal waves. Here one assumes the waves are on the liquid surface, so the longitudinal waves traveling along the *z*-direction have the wave number k_{SUR} . Then, the surface motion in phase P is represented as the frequency ω_0 and wave number k_{SUR}=0. Since it is difficult to excite unison motion of a large liquid surface area in phase, surface acoustic waves appear on the liquid surface as shown in (b) from ref. **(94)**.

Enrichment of one component of the mixture in the mist above an ultrasonic fountain has been reported in ref (104) where concentrations were determined using spectrophotometry. By collecting the mist droplets in the distillate with a cyclone separator, author found that the droplets above a solution of Trition X-100 in water were enriched in the surfactant by as much as a factor of 10, depending on the original surfactant concentration. A quantitative theory of enrichment was given based on the droplet diameter and the surface tension of the surfactant: the smaller the droplet, the larger its surface to volume ratio, which leads to a dependence of the enrichment on the inverse of the droplet radius. The experiments reported in ref (104) showed qualitative agreement with the predictions of the theory. Further experiments by two different groups (95) (105) with different surfactants show significant enrichment of the mist in the surfactant as well. According to the model of ultrasonic distillation given in ref (104), the property of surfactants to concentrate at the solution-vapor interface presents ideal conditions for separation using ultrasound.

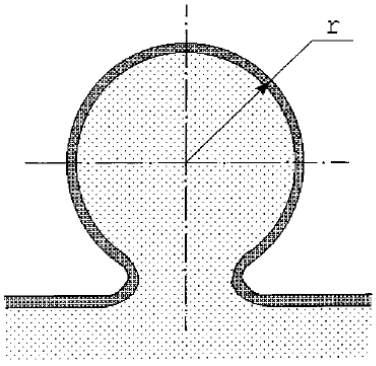

Figure 64: Droplet breaking off the surface of the solution containing a surface-active solute from ref. **(104)**.

For ethanol-water mixtures, the concentration of ethanol at the liquid-vapor interface was investigated in ref (106) for six different alcohols using surface tension measurements. By calculating the logarithmic derivative of the surface tension with respect to activity in the Gibbs adsorption equation, the author was able to determine the surface excess of alcohol for each of the water-alcohol mixtures. Gibbs adsorption equation is;

$$\Gamma_{al}^{\mathrm{wa}} = -\frac{1}{RT}\left(\frac{\partial\gamma}{\partial \ln a_{\mathrm{al}}}\right)_T \tag{37}$$

where γ is the surface tension and a_{al} is the activity of alcohol.

The author found that the adsorption isotherms of the six alcohol-water mixtures studied show similar behavior and that the data for each mixture indicate the presence of an alcohol monolayer, the underlying cause of the monolayer formation being attributed to the formation of a strong hydrogen bond network in the water. Additional studies corroborating the finding of concentration of ethanol in a surface layer of an ethanol-water mixture can be found in ref (107) where grazing incidence X-ray reflection experiments with ethanol-water mixtures showed surface excesses of ethanol. The same X-ray reflection experiments were able to determine the thicknesses of the ethanol layers. Investigations (108) (109) (110) using small-angle X-ray scattering permitted determination of the particle size distribution of water and ethanol mists produced by insonation of liquids with high-intensity ultrasound. This work concludes that for atomization of neat solutions, water droplets are produced with sizes in the range of micrometers, whereas ethanol droplets are formed with nanometer sizes. This result can be qualitatively corroborated visually by observation (110) (111) of the mist from either

solvent subjected to intense ultrasound; water produces a fog that is clearly visible through its scattering of visible radiation, while neat alcohol under the same conditions produces essentially no visible fog.

Aside from the report of strong ethanol concentration in the mist of ethanol-water mixtures in refs (94) and (110), the experiments reported in ref (103) show selective concentration of alcohols to 40 mol % in the mist from a 20 mol % solution of ethanol in water at 25 °C. On the basis of their experiments, one concludes that cavitating bubbles enriched in ethanol are produced near the liquid-vapor surface which ejects mist enhanced in the concentration of ethanol. (103) Further reports of alcohol concentration in the mist above an ultrasonic fountain are given in refs (112) (113).

The research reported here shows that there is enrichment of the mist above the liquid solution in agreement with the results given in refs (94), (103), and (110); however, complete separation of ethanol at 11 °C in the mixture to yield a mist of pure ethanol is not found, as reported in refs (94) and (110). As well, sparging yields a higher concentration of the more volatile component of the mixture in the distillate than ultrasonic distillation in every experiment reported here. For the case of ethanol-ethyl acetate above the azeotrope, the vapor phase is enriched in the azeotropic composition and the residual liquid phase is enriched in ethyl acetate, again with the more complete separation being that given by sparging.

Rayleigh distillation curves (114) in Figure 61 were calculated using activity coefficients obtained from refs (115) (116) (117). Since the resultant composition of the vapor in the sparging gas bubbles is determined by the integrated mass transfer history as the bubbles rise from the injection point to the liquid surface, exact agreement with the

calculated curves was not expected. However, as shown, the agreement between the Rayleigh calculations and the sparging data versus liquid volume fraction remaining is quite good, suggesting that there was sufficient bubble residence time in the liquid to get quite close to true equilibrium compositions. These results lend credence to the validity of the measurement techniques employed here.

In general, it is expected that sparging should produce a different distillate composition than a process that selectively removes the very top fraction of the liquid, if the composition of the liquid at the interface differs from that of the bulk. The experiments with surfactants in water reported in refs (104) and (105) confirm a high separation capability for ultrasonic distillation, showing the mist collected above an ultrasonic fountain to be highly enriched in the surfactant. Surfactants however provide an extreme case of concentration of one component at the liquid-vapor interface with far lower concentrations in the bulk. Despite the findings reported here regarding the relative merits of sparging versus ultrasonic distillation, which bring doubt to the thesis of using ultrasonic distillation for substantial economic gain in the separation of ethanol from fermented biomass, there exists convincing evidence for an ultrasonic distillation effect (104) (105) that has a unique separation capability for species concentrated at the liquid surface that warrants its further elucidation.

5. 4 Conclusion

The application of intense ultrasound to a liquid-gas interface results in the formation of an ultrasonic fountain and generates both mist and vapor from the liquid. The composition of the vapor and aerosol above an ultrasonic fountain is determined as a function of irradiation time and compared with the results of sparging for five different solutions. The experimental apparatus for determining the efficiency of separation consists of a glass vessel containing a piezoelectric transducer driven at either 1.65 or 2.40 MHz. Dry nitrogen is passed over the ultrasonic fountain to remove the vapor and aerosol. The compositions of the liquid solutions are recorded as a function of irradiation time using gas chromatography, refractive index measurement, nuclear magnetic resonance, or spectrophotometry. Data are presented for ethanol-water and ethyl acetate-ethanol solutions, cobalt chloride in water, colloidal silica, and colloidal gold. The experiments show that ultrasonic distillation produces separations that are somewhat less complete than what is obtained using sparging.

APPENDIX A. Laser System

A.1 Nd:YAG Laser

A LASER (Light Amplification by Stimulated Emission of Radiation) is a device that emits light through a process of optical amplification based on the stimulated emissions of photons. The laser used in the experiments described here is Nd:YAG, where the active element is neodymium in a host crystal of yttrium aluminum garnet. The output power of the Nd:YAG laser is optimally 10 W at 1064 nm. The fundamental wavelength of the laser is usually frequency doubled or tripled with the aid of nonlinear optics, resulting in intense lines at 532 nm and 355 nm. The Nd:YAG laser used in the research of this thesis is a 10 ns YG580 series Q-switched laser for Quantel Inc. (118) The Nd:YAG laser is a four level system in which the active element is Nd^{+3} ion in the YAG lattice as shown in Figure 65.

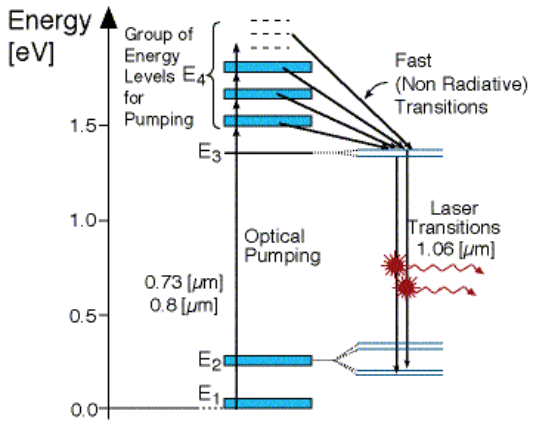

Figure 65: Energy level diagram of a Nd:YAG Laser.

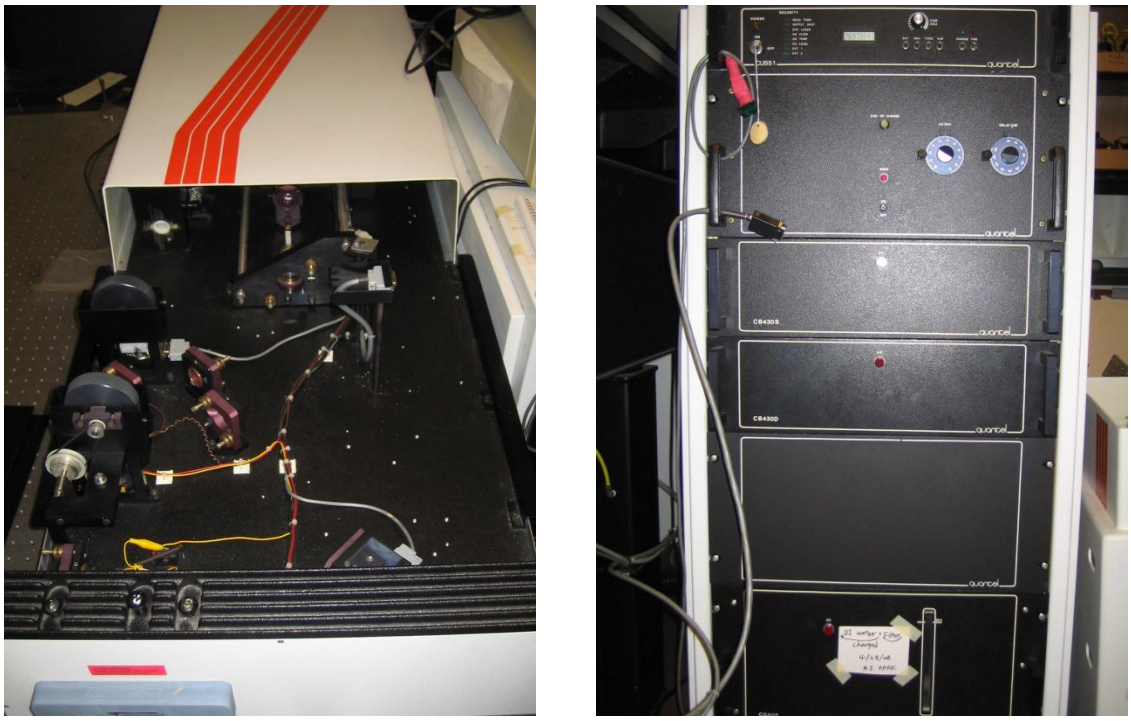

Figure 66: Actively Q-switched Nd:YAG laser (YG 580 series, Quantel International).

Q-switching

To operate a laser in a pulsed mode, the method of "Q-switching" is used. Q-switching blocks the optical path of the resonator cavity of the laser until the population inversion is high, at which point it is switched to open the optical path resulting in a high-energy output pulse. (119) Typically after Q-switching, the output is a pulse that is 10 to 20 ns long, full width at half maximum (FWHM). There are active and passive methods of Q-switching. Active Q-switching involves an externally controlled electro-optic that acts as a fast shutter. An example of an electro-optic is a Pockell's cell. A Pockell's cell is essentially voltage-controlled wave plates, which is designed to block the feedback of the intracavity light by rotating its polarization. (120) When the medium is saturated, the Pockell's cell is switched and the intracavity light is allowed to exit. Both the nanosecond and picosecond lasers use a Pockell's cell for active Q-switching. To get an even shorter pulse, a method of passive Q-switching is used. Passive Q-switching uses a saturable absorber that has a fast relaxation time. Similarly to an externally driven electro-optic, the saturable absorber is typically a bleachable dye that is opaque at low light intensities. (119) The laser cavity is blocked by the opacity of the dye until fluorescence is raised sufficiently. After absorbing sufficient fluorescence from the lasing medium, the dye is bleached, resulting in the transmission of a short, high energy pulse. The attractive features of a saturable absorber are its wavelength range, dynamic response time, and its saturation intensity.

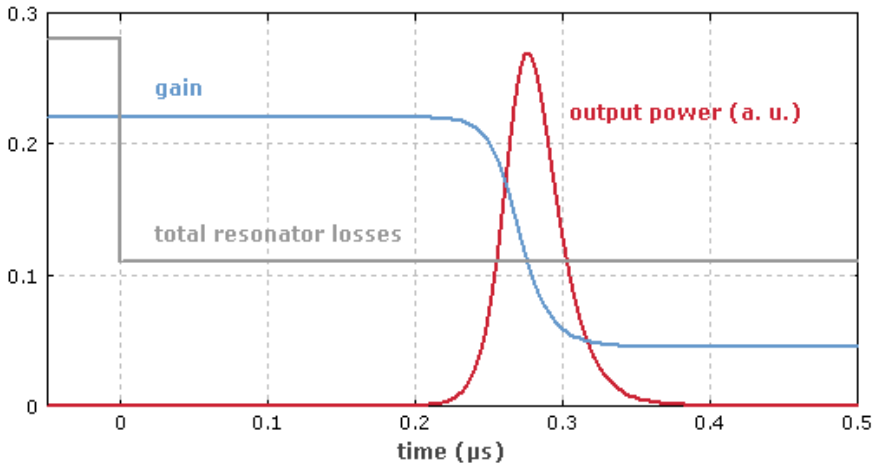

Figure 67: Temporal evolution of gain and losses in an actively Q-switched laser. The Q switch is activated at t=0. The power starts to rise exponentially at this point, but becomes high only after ~0.2 µs.

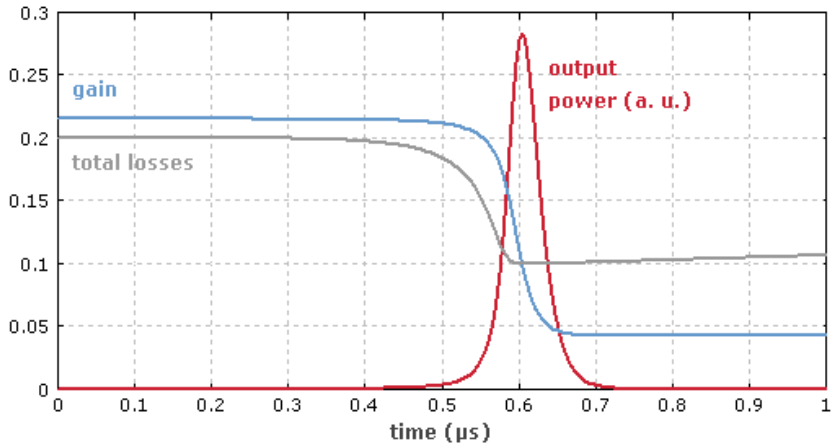

Figure 68: Temporal evolution of gain and losses in a passively Q-switched laser. Shortly after the laser gain exceeds the resonator losses, a short pulse is emitted. Once the absorber starts to be saturated, the power rises rapidly.

Harmonic Generation

Crystal materials lacking inversion symmetry can exhibit a so-called nonlinearity. This can give rise to the phenomenon of frequency doubling, where an input (pump) wave generates another wave with twice the optical frequency (i.e., half the wavelength) in the medium. This process is also called second-harmonic generation.

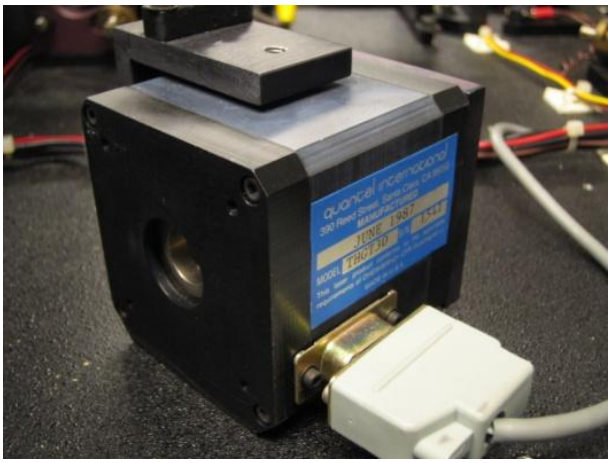

Figure 69: Second harmonic generator (Quantel International)

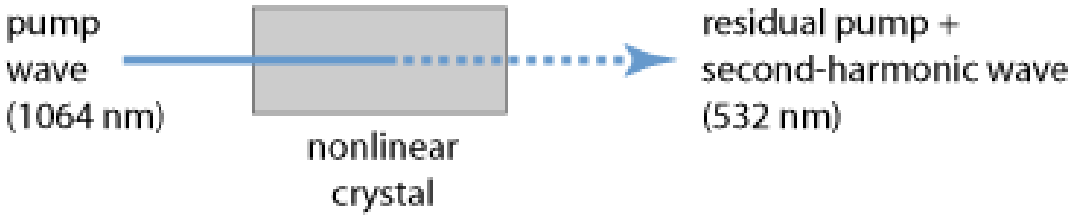

Figure 70: A typical configuration for frequency doubling: an infrared input beam at 1064 nm generates a green 532-nm wave during its path through a nonlinear crystal.

A. 2 Optical Attenuator

An optical attenuator is a device used to reduce the power level of an optical signal. It was used in this research to control the output of the Nd:YAG laser. An illustration of the main components of the attenuator is given in Figure 71. Because the laser beam is polarized coming out of laser, a ½ wave plate is used to rotate one of the polarizations of the light by 180°. (119) The laser beam then passes through a Glan-Taylor Polarizer or Glan-Taylor Prism that transmits only p-polarized light and reflects s-polarized light at 90°, the result of which is the attenuation of the beam. The Glan-Taylor polarizer is made of two right-angled calcite prisms that are separated by an air gap. The ½ wave quartz plate is a polarization rotator.

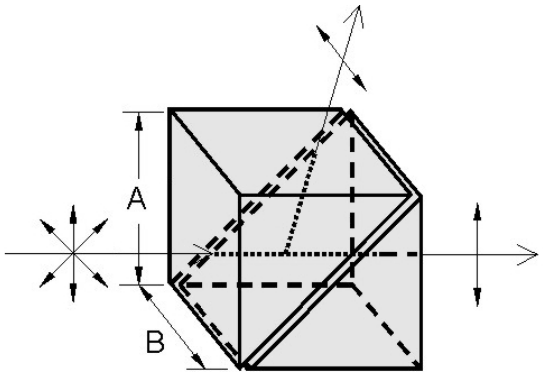

Figure 71: Glan-Taylor Polarizer.

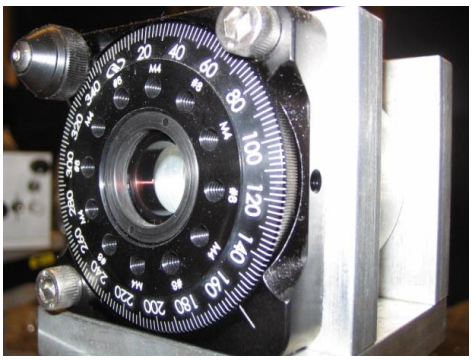

Figure 72: Rotation stage RSP-1T (Newport Co.)

APPENDIX B. Photomultipliers

The photomultipliers used in this work operate based on the photoelectric effect. Electrons are emitted from a material due to absorption of a photon. For a metal surface, an electron is emitted when the energy of an absorbed photon, hv, exceeds a minimum value of φ, called the work function, which is characteristic of the material. (121) The photodetectors that were used in this research are photomultipliers. Photomultiplier tubes (PMT) are constructed in a glass or quartz vacuum tube which houses a photocathode, several dynodes, and an anode. For a single photon incident on a photocathode, positioned at the entryway of the device, electrons are produced that are directed with a focusing electrode to the electron multiplier. (119) (122) (123) A photocathode is a negatively charged electrode that is coated with photosensitive material. The electron multiplier produces secondary electrons off of a series of electrodes that are referred to as dynodes. Each dynode is held at a more positive voltage then the previous one; thus, as the electrons from the cathode move towards the first dynode, they are accelerated by the electric field and arrive at the next sequential dynode with more energy. The configuration of the dynodes produces a cascade of an ever-increasing number of electrons. In practice, a PMT is capable of multiplying a light signal by approximately 10^9. This high gain sets a limitation on detection because at high radiant intensities, irreparable damage can be done to the photoelectric surface. (119) (121)

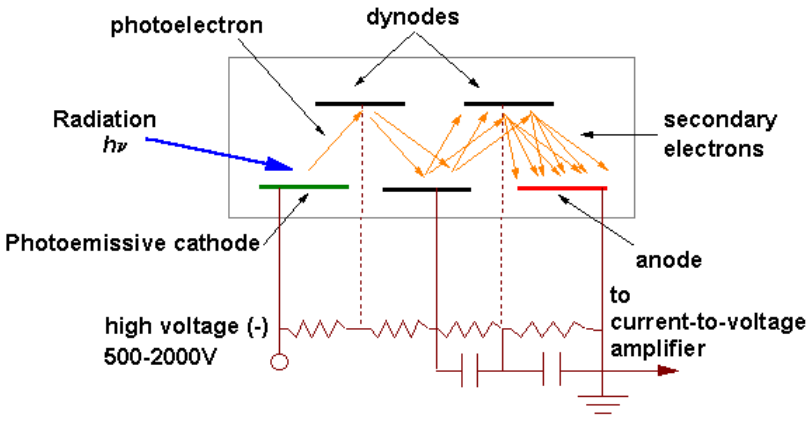

Figure 73: Photomultiplier tube construction and operation.

B. 1 Hamamatsu - 931A

Side-On types with UV to Visible Sensitivity

Table 4: Key Specifications of Hamamatsu – 931A

Size - 28mm	Cathode Luminous Sensitivity – 40 µA/lm
Active Dia/L - 8mm	Cathode Blue Sensitivity Index - 5
Active Height - 24mm	Anode Luminous Sensitivity – 400 A/lm
Min λ - 300µm	Gain - 1.0E+07
Max λ - 650µm	Dark Current after 30 min. – 5 nA
Peak Sens. - 400µm	Rise Time - 2.2 ns
Cathode Radiant Sensitivity – 48 mA/W	Transit Time – 22 ns
Window - Borosilicate	Number of Dynodes - 9
Cathode Type - Sb-Cs	Applied Voltage - 1000V

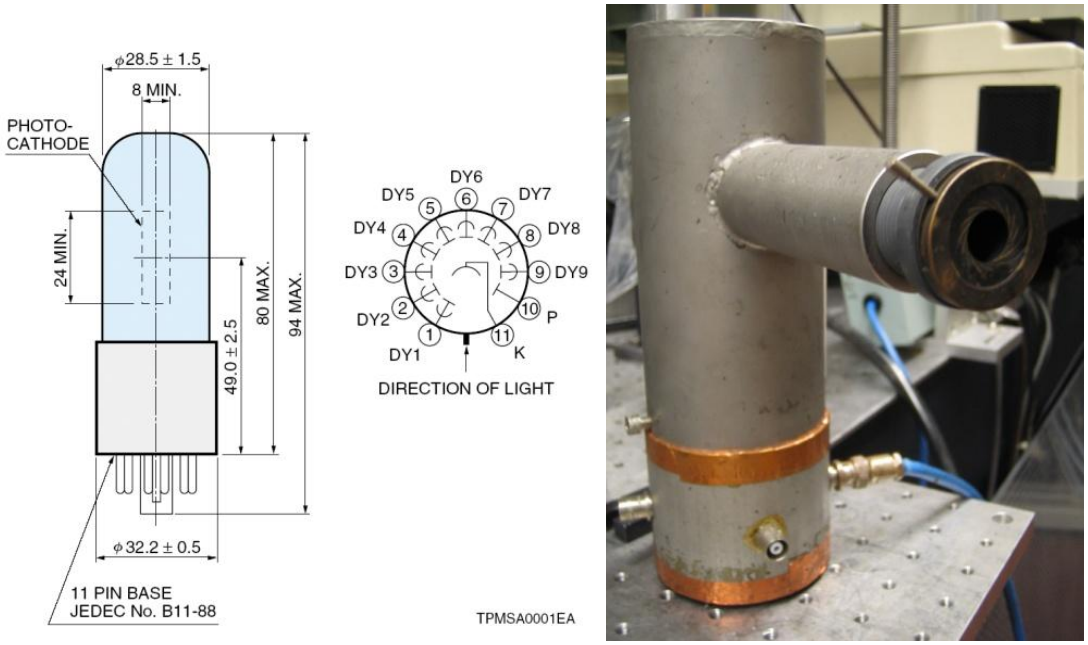

Figure 74: External dimensions (mm) of photomultiplier (Hamamatsu - 931A)

B. 2 Electron Tubes Inc. - 9558B

The 9558B is a 51mm (2”) diameter end window photomultiplier, with S20 infra-red sensitive photocathode, and 11 high gain, high stability, SbCs dynodes of the long established venetian blind design providing a low afterpulse rate.

Table 5: Window Characteristic of Photomultiplier (Electron Tubes Inc. - 9558B)

	9558B borosilicate
spectral range**(nm)	290 - 870
refractive index (n_d)	1.49
K (ppm)	300
Th (ppb)	250
U (ppb)	100

Table 6: Characteristics of Photomultiplier (Electron Tubes Inc. - 9558B)

	unit	min	typ	max
photocathode: S20				
active diameter	mm		46	
quantum efficiency at peak	%		21	
luminous sensitivity	µA/lm		200	
with CB filter		6	9	
with CR filter			90	
with IR filter		7	13	
dynodes: 11VBSbCs				
anode sensitivity in divider A:				
nominal anode sensitivity	A/lm		200	
max. rated anode sensitivity	A/lm		2000	
overall V for nominal A/lm	V		1050	1500
overall V for max. rated A/lm	V		1400	
gain at nominal A/lm	x 10^6		1	
dark current at 20 °C:				
dc at nominal A/lm	nA		2	20
dc at max. rated A/lm	nA		20	
dark count rate	s^{-1}		15000	
pulsed linearity (-5% deviation):				
divider A	mA		2	
rate effect (I_a for $\Delta g/g$=1%):	µA		20	
magnetic field sensitivity:				
the field for which the output decreases by 50 %				
most sensitive direction	T x 10^{-4}		1.7	
temperature coefficient:	% $°C^{-1}$		± 0.5	
timing:				
single electron rise time	ns		10	
single electron fwhm	ns		22	
transit time	ns		65	
weight:	g		180	
maximum ratings:				
anode current	µA			100
cathode current	nA			1000
gain	x 10^6			10
sensitivity	A/lm			2000
temperature	°C	-80		60
V (k-a)(1)	V			2300
V (k-d1)	V			450
V (d-d)(2)	V			300
ambient pressure (absolute)	kPa			202

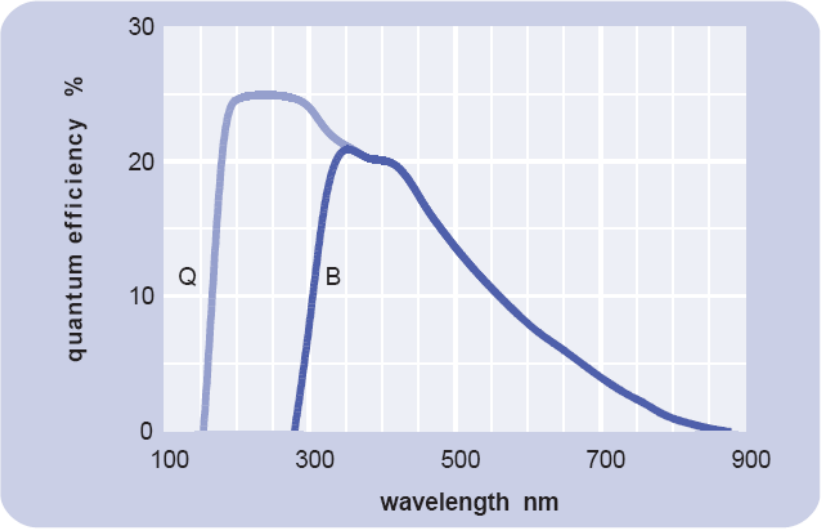

Figure 75: Typical spectral response curves of photomultiplier (Electron Tubes Inc. - 9558B)

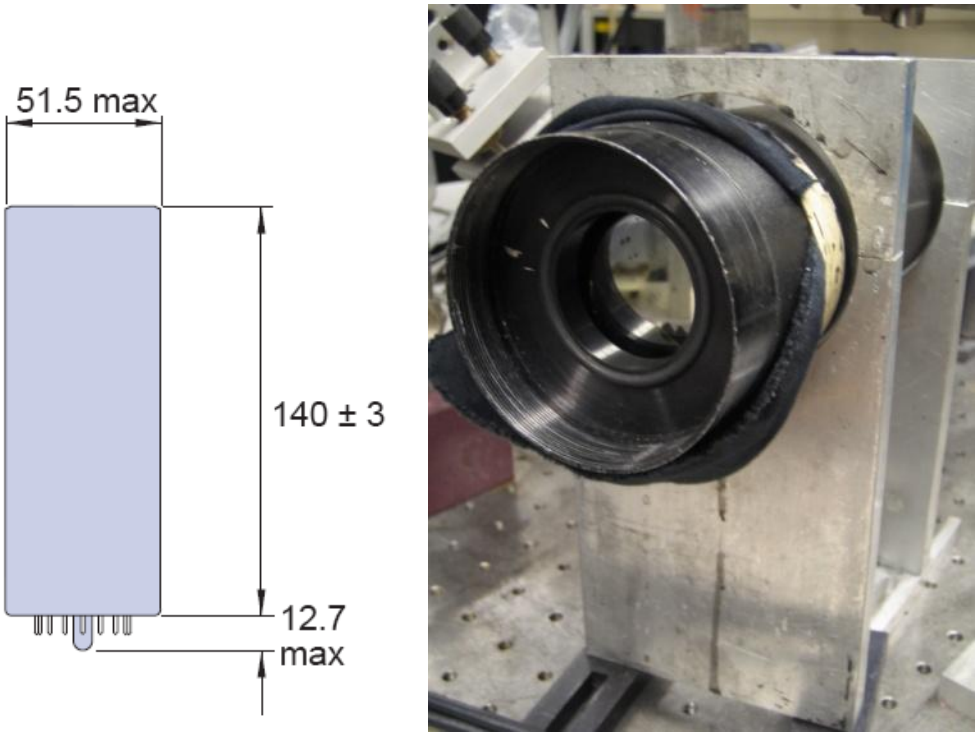

Figure 76: External dimensions (mm) of photomultiplier (Electron Tubes Inc. - 9558B) and a photo of cathode

APPENDIX C. Oscilloscopes

An oscilloscope is a device that monitors and records the time evolution of the voltage signal from the PMT. The anode of the high voltage photomultiplier is connected to the oscilloscope via a coaxial cable with a BNC connector. An oscilloscope monitors signal voltage versus time by a graphical display on a screen. A digital oscilloscope samples the waveform and uses an analog-to-digital converter (ADC) to convert the analog signal into a series of numbers stored in the memory of the oscilloscope. (119) The ADC in the acquisition system samples the signal at discrete points. The horizontal system's sample clock determines how often the ADC takes a sample. The rate at which the clock takes the sample is called the sampling rate and is measured in samples per second. These sample points are stored in the memory as waveform points. The waveform points then make up a waveform record. The oscilloscope used here is an Agilent Technologies Infinium 54845 A that had a sample rate of 8 GS/s, which is currently considered a fast oscilloscope. (124) With this high sampling rate, fast signals could be monitored. The sampling rate is one of several limitations to the type of signals that could be monitored. Another limitation is bandwidth, which specifies the frequency range over which the oscilloscope can accurately record. By convention, the bandwidth indicated the frequency at which the amplification is reduced to 70.7%. (119) (125) The bandwidth of the oscilloscope was 1.5 GHz.

A trigger was used that determined the start and stop points to be record. The trigger used for the experiments was a silicon photodiode that detected scattering light from the pump laser. Vertical sensitivity is an important factor that indicates the extent to which

the vertical amplifier can amplify a weak signal: for this oscilloscope, the smallest voltage that could be detected was on the order of 2 mV. The computer was interfaced with a LabVIEW program to communicate with the oscilloscope.

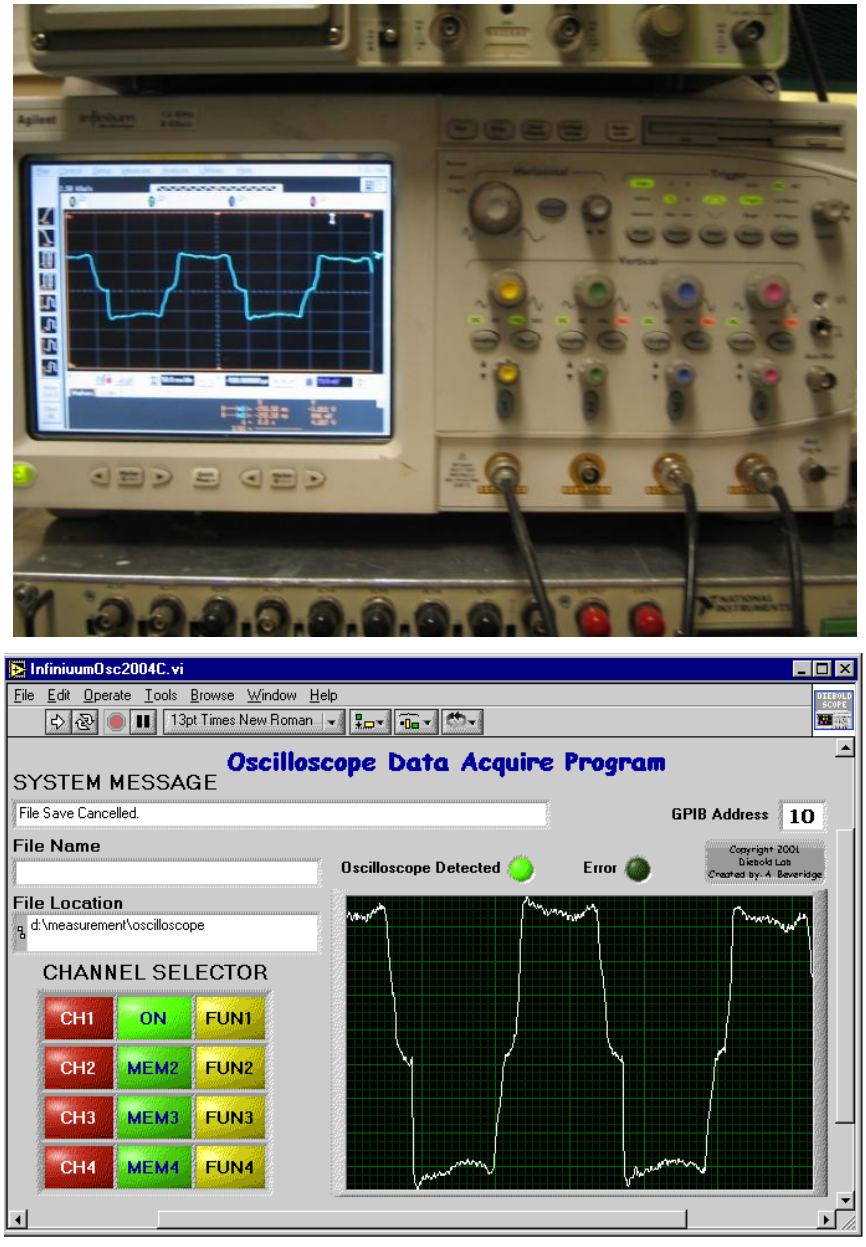

Figure 77: Digital Oscilloscope (Infinium 54845 A, Agilent Technologies) and oscilloscope data acquisition program.

APPENDIX D. Spectrophotometers

A spectrometer is a device for determining the absorption coefficient of samples. The spectrophotometer (UV/Vis Cary 50 spectrometer) uses the intense radiation from a Xenon lamp via the passage of current through an atmosphere of xenon. The wavelength range of the spectrophotometer is 190-1100 nm. The light from the xenon source passes through a beam expander that is reflected off of a mirror and directed to an automated, computer-controlled grating that has a maximum scan speed of 24,000 nm/min. The light reflected off of the grating is directed towards another reflective mirror and passes through an exit slit. The light then passes through a beamsplitter allowing simultaneous reference beam correction. The beam passes through the sample and the light intensity is monitored with a lead selenide (PbSe) detector. The beam intensities are related according to Beer's law, Equation 38, where I and I_0 are the attenuated and initial light intensities recorded before and after the cell. The absorbance, A, of the species is defined as the logarithm of the ratio of the attenuated intensity to that of the initial intensity. Conversely, transmittance, T, can be found from the expression given in Equation 39. The right-hand side of Equation 40 expresses the absorbance as being dependent on the parameters ε, b, and c are the molar absorptivity, pathlength, and concentration, respectively.

$$\log_{10}\frac{I}{I_0} = A = \varepsilon bc \tag{38}$$

$$A = -\log_{10} T \tag{39}$$

$$T = e^{-\varepsilon bc} \tag{40}$$

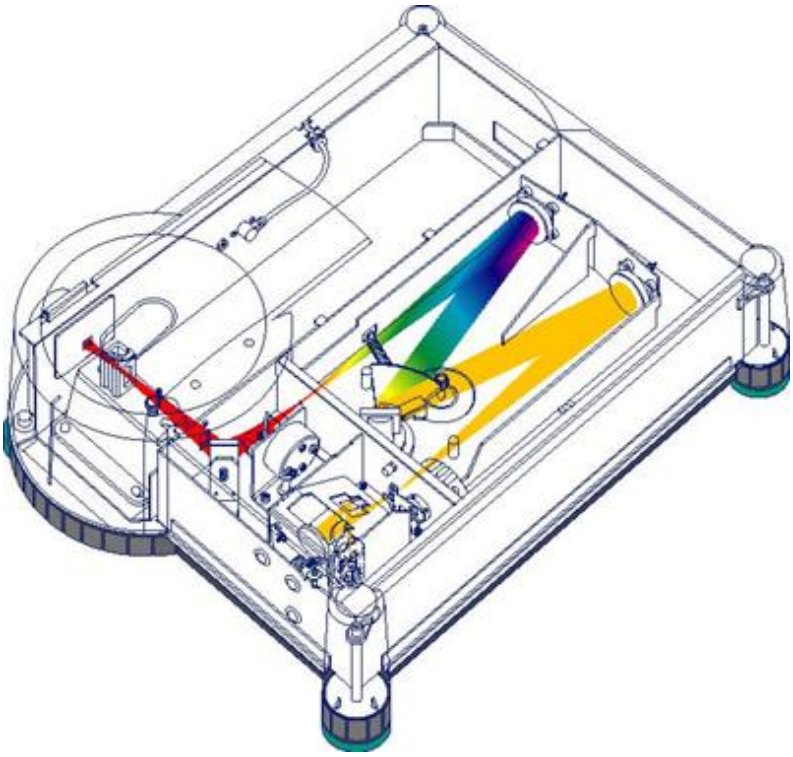

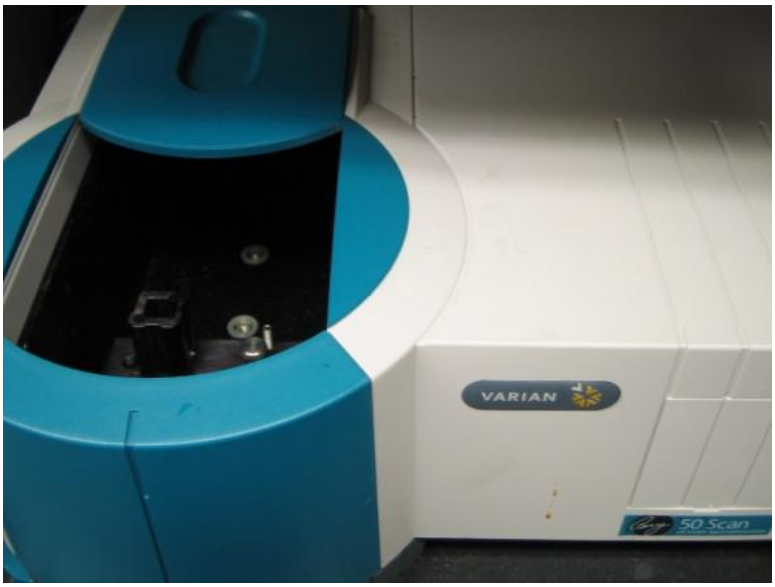

Figure 78: UV/Vis spectrometer (Cary 50, Varian Inc.)

APPENDIX E. Ultrasonic Transducers

A transducer is a device that converts one type of energy or physical attribute to another for various purposes including measurement or information transfer. The transducers used in the experiments are piezoelectric transducers. In a piezoelectric transducer, the active element is basically a piece of polarized material with electrodes attached to two of its opposite faces. When an electric field is applied across the material, the polarized molecules align themselves with the electric field, resulting in induced dipoles within the molecular or crystal structure of the material. This alignment of molecules causes the material to change dimensions. In addition, a permanently-polarized material will produce an electric field when the material changes dimensions as a result of an imposed mechanical force. This phenomenon is known as the piezoelectric effect.

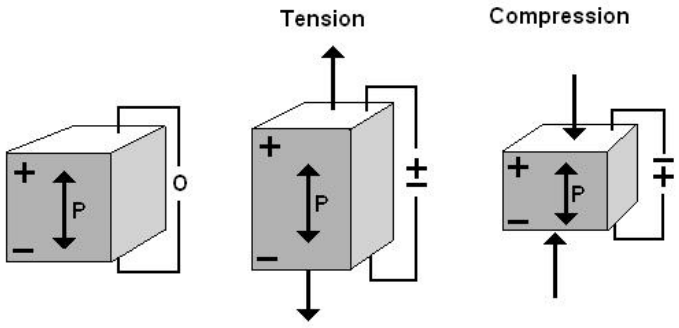

Figure 79: Piezoelectric effect.

Figure 80: Polyvinylidene fluoride (PVDF) film transducer.

APPENDIX F. Voltage Amplifier

Voltage amplifier is an electronic amplifier that varies its gain depending on a control voltage. The application includes oscilloscopes, transient recorder preamplifiers, photomultipliers, microchannel-plate amplifiers, time-resolved pulse and transient measurements, and amplification of digital signals (no baseline shift at any digital code).

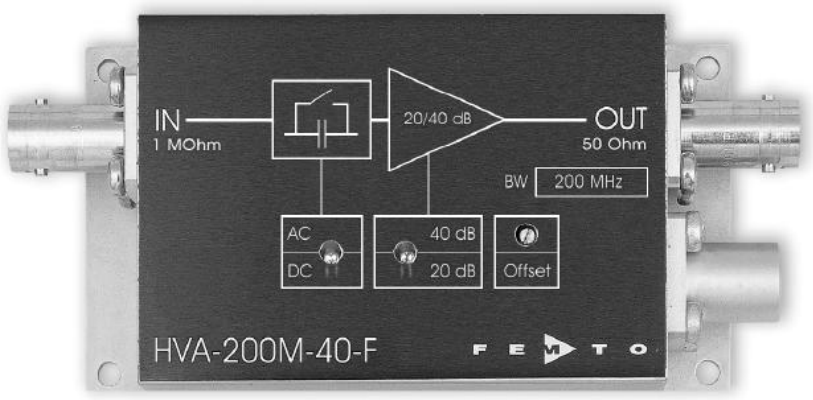

Figure 81: 200 MHz high input impedance voltage amplifier (FEMTO).

Table 7: Key Specifications of HVA-200M-40-F

Lower Cut-off frequency	DC/ 1 Hz
Upper Cut-off frequency	200 MHz
Input Impedance	1 MΩ, BNC
Gain	20/40 dB
Input Noise Voltage	4.5 nV/√Hz
Input Voltage Drift	5 μV/ºC
Output Voltage	±1V@ 50Ω

APPENDIX G. Carbon Black

Carbon blacks are produced by subjecting heavy residual oil feedstock to extremely high temperatures in a carefully controlled combustion process. They are used as a pigmenting, UV stabilizing and conductive agent in a variety of common and specialty products.

Table 8: Properties of Carbon Black

Cabot Black Pearls 1300	Cabot Black Pearls 470
Surface area – 560 M^2/gm	Surface area – 85 M^2/gm
Particle size – 13 nm	Particle size – 25 nm
Density – 16 Lbs./Cu.Ft.	Density – 23 Lbs./Cu.Ft.

Figure 82: Carbon black

Bibliography

1. **Bell, A. G.** s.l. : Am. J. Sci., 1880, Vol. 120. 305.

2. **Bell, A. G.; Tainter, S.** s.l. : Philos. Mag., 1881, Vol. 11. 510.

3. **Tyndall, J.** s.l. : Proc. R. Soc. Lond., 1881, Vol. 32. 307.

4. **Roentgen, W.** s.l. : Philos. Mag., 1881, Vol. 11. 308.

5. **Mercadier, M. E.; Hebd, C. R.** s.l. : Serv. Acad. Sci, 1881, Vol. 92. 409.

6. **Preece.** s.l. : Proc. R. Soc. Lond., 1881, Vol. 31. 506.

7. **Viengerov, M. L.** s.l. : Dokl. Akad. Nank. SSSR, 1938, Vol. 19. 687.

8. **Kreuzer, L. B.** s.l. : J. Appl. Phys., 1971, Vol. 42. 2934.

9. **Rosencwaig.** s.l. : Optics Commu., 1973, Vol. 7. 305.

10. **Roscencwaig.** *Photoacoustics and Photoacoustic spectroscopy.* New York : Wiley, 1980.

11. **Bialkowski, S. E.** *Photothermal Spectroscopy Methods for Chemical Analysis.* New York : John Wiley & Sons Inc., 1996.

12. **Rosencwaig, A.** s.l. : Anal. Chem, 1975, Vol. 47. 592.

13. **Ball, D.** s.l. : Spectroscopy, 2006, Vol. 21. 14.

14. **Mandelis, A.** *Non-destructive Evaluation (NDE).* New Jersey : Prentice Hall, 1994.

15. **Kundu, T.** *Nondestructive Evaluation: Engineering and Biological Material Characterization.* Boca Ranton, FL : CRC Press, 2004.

16. **Diebold, G. J.; Sun, T.** s.l. : Acustica, 1994, Vol. 80. 339.

17. **Diebold, G. J.; Sun, T.; Khan, M. I.** s.l. : Phys. Rev. Lett., 1991, Vol. 67. 3384.

18. **Khan, M. I.; Sun, T.; Diebold, G. J.** s.l. : J. Acoust. Soc. Am., 1993, Vol. 93. 1417.

19. **Anderson, V. E.; Chen, H.Z.; Diebold, G. J.; Mahmood, A.; Sweigart, D. A.** s.l. : J. Am. Chem. Soc., 1987, Vol. 109. 6191.

20. **Diebold, G. J.; Hayden, J. S.** s.l. : Chem. Phys., 1980, Vol. 49. 429.

21. **O'Connor, M. T.; Diebold, G. J.** s.l. : Nature, 1983, Vol. 301. 321.

22. **Heihoff, K.; Braslavsky, S. E.** s.l. : Chem. Phys. Lett., 1986, Vol. 301. 321.

23. **Sun, T.; Diebold, G. J.** s.l. : Nature, 1992, Nature, Vol. 355, p. 806. 806.

24. **Frez, C.; Tran, C. D.; Yu, S.; Diebold, G. J.** s.l. : J. Chem. Eng. Data., 2006, Vol. 51. 1250.

25. **Yan, Y.-X.; Chen, L-T.; Nelson, K. A.** s.l. : J. Chem. Phys., 1988, Vol. 88. 6477.

26. **Duggal, A. R.; Nelson, K. A.** s.l. : J. Chem. Phys., 1991, Vol. 94. 7677.

27. **Chen, H. X.; Diebold, G. J.** s.l. : J. Chem. Phys., 1996, Vol. 104. 6730.

28. **Sun, T., et al.** s.l. : J. Chem. Phys., 1992, Vol. 97. 9324.

29. **Morse, P. M.; Ingard, K. U.** Princeton, NJ : Princeton University Press, 1968.

30. **Temkin, S.** *Elements of Acoustics.* USA : American Institute of Physics, 2001.

31. **Kundu, P. K.** *Fluid Mechanics.* New York : Academic Press, 1990.

32. **Brennen, C. E.** *Cavitation and Bubble Dynamics.* New York : Oxford University Press, 1995.

33. **Young, F. R.** *Cavitation.* London : McGraw-Hill Book Co., 1989.

34. **Nowacki, W.** *Dynamic Problems of Thermoelasticity.* Leyden : Noorhoof Int., 1976.

35. **Nowacki, W.** *Thermoelasticity.* New York : Pergamon Press: Oxford, 1986.

36. **Zharov, V. P.; Letfullin, R. R.; Galitovskaya, E. N.** s.l. : J. Phys. D: Appl. Phys., 2005, Vol. 38. 2571.

37. **Lin, C. P.; Kelly, M. W.** s.l. : App. Phys. Lett., 2003, Vol. 72. 2800.

38. **Chen, H. X.; Diebold, G. J.** s.l. : Science, 1995, Vol. 270. 963.

39. **Park, H. J.; Wu, B.; Diebold, G. J.** s.l. : J. Chem. Phys., 2011, Vol. 134. 124513.

40. **Park, H. J.; Diebold, G. J.** 2011. manuscript in preparation.

41. **Heritier, J-M.** s.l. : Opt. Comm, 1983, Vol. 44. 267.

42. **Tam, A. C.** s.l. : Rev. Mod. Phys., 1986, Vol. 58. 381.

43. Institute of Hydrochemistry, Technische Universität München.

44. **Frenzel, H.; Schultes, H.** s.l. : j. Phys. Chem., 1934, Vol. B 27. 421.

45. **Suslick, K.** Sonochemistry. *Comprehensive Coordination Chemistry 2.* New York : Elsevier Science, 2003.

46. **Matula, T.; Roy, R.; Mourad, P.; McNamara III, W.; Suslick, K.** s.l. : Phys. Rev. Lett., 1995, Vol. 75. 2602.

47. **Gaitan, F.** *an Experimental Investigation of Acoustic Cavitation in Gaseous Liquids.* s.l. : University of Mississippi, Ph. D. thesis, 1990.

48. **Crum, L.; Roy, R.** s.l. : Science, 1994, Vol. 266. 233.

49. **Barber, B.; Hiller, R.; Lofstedt, R.; Putterman, S.; Weninger, K.** s.l. : Physics Reports, 1997, Vol. 281. 65.

50. **Brenner, M.; Hilgenfeldt, S.; Lohse, D.** s.l. : Rev. Mod. Phys., 2002, Vol. 74. 425.

51. **Moss, W.; Clarke, D.; White, J.; Young, D.** s.l. : Physics Letters A, 1996, Vol. 211. 69.

52. **Moss, W.; Clarke, D.; Young, D.** *Star in a jar. In Sonochemistry and Sonoluminescence.* Dordrecht, Netherlands : Kluwer Academic Publishers, 1999. Vol. 524.

53. **Crum, L.; Mason, T.; Reisse, J.; Suslick, K.** Sonochemistry and Sonoluminescence. Dordrecht, Netherlands : Kluwer Acadimic Publishers, 1999.

54. **Putterman, S.** s.l. : Scientific American, 1995, Vol. 272. 46.

55. **Gompf, B.; Gunther, R.; Nick, G.; Pecha, R.; Eisenmenger, W.** s.l. : Phys. Rev. Lett., 1997, Vol. 79. 1405.

56. **Hilgenfeldt, S.; Lohse, D.; Moss, W. C.** s.l. : Phys. Rev. Lett, 1998, Vol. 80. 1332.

57. **Dan, M.; Cheeke, J. D. N.; Kondic, L.** s.l. : Phys. Rev. Lett., 1999, Vol. 83. 1870.

58. **Vazquez, G. E.; Putterman, S. J.** s.l. : Phys. Rev. Lett., 2000, Vol. 85. 3037.

59. **Hiller, R.; Weninger, K.; Putterman, S.; Barber, B.** s.l. : Science, 1994, Vol. 266. 248.

60. **Stottlemyer, T. R.; Apfel, R. E.** s.l. : J. Acousti. Soc. Am, 1997, Vol. 102. 1418.

61. **Harba, N.; Hayashi, S.** s.l. : J. Appl. Phys., 2003, Vol. 42. 716.

62. **Flanigan, D. J.; Suslick, K. S.** s.l. : Nature, 2005, Vol. 434. 52.

63. **Didenko, Y.; Suslick, K.** s.l. : Nature, 2002, Vol. 418. 394.

64. **Grieser, F.; Ashokkumar, M.** s.l. : Adv. Colloid Interface Sci., 2001, Vol. 89. 423.

65. **Lohse, D.; Schmitz, B.; Versluis, M.** s.l. : Nature, 2001, Vol. 413. 477.

66. **Tachibana, K., Uchida, T. Yamashita,N. and Tamura, K.** s.l. : Lancet, 1999, Vol. 353. 1409.

67. **R. P. Taleyarkhan, R. P.; West, C. D.; Cho, J. S.; Lahey Jr., R. T.** s.l. : Science, 2002, Vol. 295. 1868.

68. **Shapira, D.; Saltmarsh, M.** s.l. : Phys. Rev. Lett., 2002, Vol. 89. 104302.

69. **Reich, E. S.** s.l. : Nature, 2007, Vol. 445. 690.

70. **II, Thomas H. Maugh.** *Purdue physicist found guilty of misconduct.* s.l. : Los Angeles Times, July 19, 2008.

71. **Suslick, K.; Flannigan, D.** s.l. : Annu. Rev. Phys. Chem., 2008, Vol. 59. 659.

72. **Vazquez, G.; Camara, C.; Putterman, S.; Weninger, H.** s.l. : Opt. Lett., 2001, Vol. 26. 575.

73. **Moss, W. C.; Clarke, D. B.; Young, D. A.** s.l. : Science, 1999, Vol. 276. 1398.

74. **Neppiras,E; Noltingk, B.** s.l. : Proc. Phys. Soc. B, 1951, Vol. 64. 1032.

75. **Hiller, R.; Putterman, S.; Barber, B.** s.l. : Phys. Rev. Lett., 1992, Vol. 69. 1182.

76. **McGrath, T.; Beveridge, A.; Diebold, G.** s.l. : Appl. Phys. Lett., 1998, Vol. 73. 1029.

77. **Walton, A. ; Reynolds, G.** s.l. : Advances in physics, 1984, Vol. 33. 595.

78. **van de Hulst, H. C.** *Light Scattering by Small Particles.* New York : Wiley, 1957.

79. **Kerker, M.** *The Scattering of Light and Other Electromagnetic Radiation.* New York : Academic Press, 1969.

80. **Mohr, S.; Muller-Bbuschbaum. H.** s.l. : Angew. Chem. Int. Ed. Engl., 1995, Vol. 34. 634.

81. **Chen, H.; McGrath, T.; Diebold, G.** s.l. : Angew. Chem. Int. Ed. Engl., 1997, Vol. 36. 163.

82. **McEwan, K.; Madden, P.** s.l. : J. Chem. Phys., 1992, Vol. 97. 8748.

83. **Lin, C.; Kelly, M.** s.l. : Appl. Phys. Lett., 1998, Vol. 72. 2800.

84. **Mansour, K.; Soileau, M.; van Stryland, E.** s.l. : J. Opt. Soc. Am. B., 1992, Vol. 9. 1100.

85. **Lowen, H.; Madden, P.** s.l. : J. Chem. Phys., 1992, Vol. 97. 8760.

86. **Berkowitz, N.** *An Introduction to Coal Technology.* New York : Academic Press, 1994.

87. **von Fredersdorff, C.; Eliot, M.** *Chemistry of Coal Utilization.* New York : Wiley, 1963.

88. **Atkins, P.; Jones, L.** *Chemistry: Molecule, Matter, and Change.* New York : W. H. Freeman and Company, 1997.

89. **Strickland-Contable, R.** s.l. : J. Chem. Phys., 1950, Vol. 47. 356.

90. **Titova, K. V.; Nikol'skaya, V. P.; Buyanov, V. V.; Suprun, I. P.** s.l. : Russ. J. Appl. Chem., 2002, Vol. 75. 1903.

91. **Patel, C. K. N.; Tam, A. C.** s.l. : Rev. Modern Phys., 1981, Vol. 53. 517.

92. **Dunina, T. A.; Egerev, S. V.; Naugol'nykh, K. A.** s.l. : Sov. Phys. Usp., 1983, Vol. 9. 176.

93. **Egerev, S. V.; Lyamshev, L. M.; Puchenkov, O. V.** s.l. : Sov. Phys. Usp., 1990, Vol. 33. 739.

94. **Sato, M.; Matsuura, K.; Fujii, T. .** s.l. : J. Chem. Phys. , 2001, Vol. 114. 2382.

95. **Nii, S.; Matsuura, K.; Fukazu, T.; Toki, M.; Kawaizumi, F.** s.l. : Trans. IChemE, Part A: Chem. Eng. Res. Des., 2006, Vol. 84. 412.

96. **Beyer, R. T.** *Nonlinear Acoustics.* Washington, DC : U.S. Department of Defense, Department of the Navy, Naval Sea Systems Command, U.S. Government Printing Office, 1974.

97. **Murti, P. S.; Winkle, M. V.** s.l. : Ind. Eng. Chem. , 1958, Vol. 3. 72.

98. **Lighthill, J.** *Waves in Fluids.* Cambridge, U.K. : Cambridge University Press, 1987.

99. **Tsai, S. C.; Luu, P.; Childsand, P.; Teshome, A.; Tsai, C.** s.l. : Phys. Fluids, 1997, Vol. 9. 2909.

100. **Leighton, T. G.** *The Acoustic Bubble.* New York : Academic Press, 1994.

101. **Sollner, K.** s.l. : Trans. Faraday Soc., 1936, Vol. 32. 1532.

102. **Avvaru, V.; Patil, M. N.; Gogate, P. R.; Pandit, A. B. .** s.l. : Ultrasonics, 2006, Vol. 44. 146.

103. **Kirpalani, D. M.; Toll, F.** s.l. : J. Chem. Phys., 2002, Vol. 117. 3874.

104. **Rassokhin, D.** s.l. : J. Phys. Chem. B , 1998, Vol. 102. 4337.

105. **Takaya, H.; Nii, S.; Kawaizumi, F.; Takahasi, K.** s.l. : Ultrason. Sonochem., 2005, Vol. 12. 483.

106. **Yano, Y. F.** s.l. : J. Colloid Interface Sci. , 2005, Vol. 284. 255.

107. **Li, Z. X.; Lu, J. R.; Styrkas, D. A.; Thomas, R. K.; Rennie, A. R.; Penfold, J.** s.l. : Mol. Phys., 1993, Vol. 80. 925.

108. **Yano, Y. J.; Matsuura, K.; Fukazu, T.; Abe, F.; Wakisaka, A.; Kobara, H.; Kaneko, K.; Kumagai, A.; Katsuya, Y.; Tanaka, M.** s.l. : J. Chem. Phys., 2007, Vol. 127. 031101.

109. **Yano, Y.; Douguchi, J.; Kumagai, A.; Limima, T.; Tomida, Y.; Miyamoto,T.; Matsuura, K.** s.l. : J. Chem. Phys., 2006, Vol. 125. 174705.

110. **Yano, Y. F.; Matsuura, K.; Fukazu, T.; Abe, F.; Wakisaka, A.; Kobara, H.; Kaneko, K.; Kumagai, A.; Katsuya, Y.; Okui, M.; Tanaka, M.** s.l. : J. Appl. Crystallogr., 2007, Vol. 40. 318.

111. **Bando, Y.; Yamaguchi, S.; Doi, K.; Nakamura, M.; Yasuda, K.; Oda, A.; Kawase, Y.** s.l. : J. Chem. Eng. Jpn., 2004, Vol. 37. 1286.

112. **Kawase, Y.;Masuya, T.; Yasuda, K.; Nakamura, M.** s.l. : J. Chem. Eng. Jpn., 2006, Vol. 39. 334.

113. **Nii, S.; Toki, M.; Watanabe, S.; Suzuki, K.; Matsuura, K.; Jukazu, T.** s.l. : J. Chem. Eng. Jpn., 2010, Vol. 43. 99.

114. **Rayleigh, L.** s.l. : Phil. Mag. , 1902, Vol. 3. 521.

115. **Walas, S.M.** *Phase Equilibrium in Chemical Engineering;.* Stoneham, MA : Activity coeffients were calculated using the Wilson Equation., 1985.

116. [Online] http://demonstrations.wolfram.com/IsobaricVaporLiquidEquilibriumComputations.

117. **AlRub, F.; Datta, R.** s.l. : Sep. Sci. Technol., 2000, Vol. 35. 2203.

118. **Continuum.** Operation and Maintenance Manual Leopard Series Laser. Santa Clara, CA : s.n., 2001.

119. **Moore, J. H.; Davis, C. C.; Coplan, M. A.** *Building Scientific Apparatus, a Practical Guide to Design and Construction.* Cambridge, MA : Perseus Books, 1991.

120. **Koechner, W.** *Solid-State Engineering.* New York : Springer, 1999.

121. **Skoog, D. A.; Holler, F. J.; Nieman, T. A.** *Principles of Instrumental Analysis.* U.S.A. : Saunders College Publishing, 1998.

122. **Engstrom, R. W.** *Photomultiplier Handbook.* Lancaster, PA : RCA Corp., 1980.

123. **Hamamatsu.** *Photomultiplier Handbook.* Bridgewater, NJ : Hamamatsu Corp., 1994.

124. **Technologies, Agilent.** *Infinium Oscilloscope.* Santa Clara, CA : Agilent Technologies, 2001.

125. **Burr-Brown.** *OPA 686 Technical Data Sheet.* Tucson, AZ : s.n.